Biochemical characterization of human Shieldin complex

Dissertation

for the award of the degree
"Doctor rerum naturalium"
of the Georg-August-Universität Göttingen

within the doctoral program
Biomolecules: Structure-Function-Dynamics
of the Göttingen Graduate Center for Molecular
Biosciences, Neurosciences and Biophysics (GGNB)

submitted by

Vivek Susvirkar

from Mumbai, India

Göttingen, 2022

Thesis Advisory Committee

Dr. Alex Faesen (Supervisor, Reviewer)
Research Group Biochemistry of Signal Dynamics
Max Planck Institute for Multidisciplinary Natural Sciences, Göttingen, Germany

Prof. Dr. Peter Rehling (Reviewer)
Department of Cellular Biochemistry
University Medical Center, Göttingen, Germany

Prof. Dr. Patrick Cramer
Department of Molecular Biology
Max Planck Institute for Multidisciplinary Natural Sciences, Göttingen, Germany

Extended Thesis Advisory Committee

Dr. Sonja Lorenz
Research Group Ubiquitin Signaling Specificity
Max Planck Institute for Multidisciplinary Natural Sciences, Göttingen, Germany

Prof. Dr. Matthias Dobbelstein
Department of Molecular Oncology
University Medical Center, Göttingen, Germany

Dr. Alexander Stein
Research Group Membrane Protein Biochemistry
Max Planck Institute for Multidisciplinary Natural Sciences, Göttingen, Germany

Date of oral examination: 30.05.2022

Abstract

Shieldin is a newly identified DNA repair effector involved in the repair of DNA double-strand breaks (DSBs) in G1 phase of the cell cycle. Shieldin is a four-component complex consisting of proteins SHLD1, SHLD2, SHLD3 and HORMA domain protein REV7. Shieldin inhibits homologous recombination (HR) through its direct ssDNA binding activity and directs the repair pathway to non-homologous end joining (NHEJ). Despite the clear understanding of Shieldin function, the basis of its recruitment and assembly at DSBs is not well understood.

In this thesis, I reconstituted the Shieldin complex using purified proteins to investigate the mechanism of Shieldin recruitment and assembly. Using this approach, I was able to elucidate the unusual stoichiometry of the Shieldin complex. In presence of SHLD3 and the SHLD2 N-terminal fragment, I observe a dimer of REV7 in Shieldin complex. HORMA REV7 exists in two topologically distinct states (open and closed) which can be isolated using trapping mutants. The assembly of Shieldin complex is surprisingly slow and depends on conversion of open REV7 (O-REV7) to closed REV7 (C-REV7) upon binding to SHLD3. I report a similar binding kinetics between REV7 and REV3 subunits of the DNA Polymerase ζ. My results demonstrate that Shieldin and Pol ζ assembly centred around REV7 is remarkably slow in vitro and thereby rate-limiting.

In order to understand the mechanism of Shieldin recruitment, I tested SHLD3 for DNA binding. My results show SHLD3 harbours a DNA-binding domain and forms DNA-protein complex independently as well as in complex with REV7 and SHLD2. SHLD3 binds both single-stranded DNA (ssDNA) and double stranded DNA (dsDNA) with similar affinities. It also shows ability to bind both telomeric and non-telomeric sequences. SHLD3 truncation studies show DNA binding activity lies in its conserved C-terminal domain (CTD). To understand its molecular basis, I used SHLD3 structure predictions from Alphafold and identified key residues involved in DNA binding. Mutagenesis of these residues attenuated DNA binding activity of SHLD3.

In conclusion, this thesis provides valuable insights into the assembly of Shieldin complex mediated by REV7 topology switch and its recruitment to DSB through the newly identified DNA-binding domain in the SHLD3 subunit. It also provides a tool to trap REV7 in either open or closed topology for future functional, kinetic, and cell-based studies.

Table of Contents

List of figures

List of Tables

Abbreviations

5,6-FAM	5,6-Carboxyfluorescein
E.coli	*Escherichia coli*
RBM	REV7 binding motif
MIM	MAD2 interacting motif
MBP	Maltose binding protein
SLS	Static-angle light scattering
RIM	REV7 interacting motif
S. frugiperda	*Spodoptera frugiperda*
SPR	Surface plasmon resonance
NHEJ	Non-homologous-end-joining
HR	Homologous recombination
DNA	Deoxyribosnucleic acid
ss	Single stranded
ds	Double stranded
kDa	kilo Dalton
BSA	Bovine serum albumin
SEC	Size exclusion chromatography
PDB	Protein data bank
K_D	Dissociation constant
K_{ON}	Rate of association
WT	Wildtype
K_{OFF}	Rate of dissociation
TRIS	Tris(hydroxymethyl)aminomethane
HEPES	4-(2-hydroxyethyl)-1-piperazineethanesulfonic acid
SDS-PAGE	Sodium dodecyl sulfate polyacrylamide gel electrophoresis

MW	Molecular weight
mL	Millilitre
R. I	Refractive index
EDC	1-ethyl-3-(3-dimethylaminopropyl)carbodiimide
NHS	N-Hydroxysuccinimide
FP	Fluorescence Polarization
HCl	Hydrochloric acid
NAD	Nicotinamide adenine dinucleotide
CV	Column volume
RT	Room temperature
PEG	Polyethylene glycol
NaOH	Sodium hydroxide
DDR	DNA damage response

1. Introduction

DNA double strand breaks (DSBs) are highly cytotoxic to cells as they cause full rupture of the chromosomes. Formation of DSBs can be caused by both exogenous and endogenous factors. The most common exogenous factor responsible for DNA DSBs is the exposure to high doses of ionization radiation. Endogenous factors responsible for DSBs can be either spontaneous or programmed. Spontaneous DSBs arise from replication stress due to replication fork collapse at ssDNA nicks or stalled replication fork at inter-strand crosslink (ICL). Programmed DSBs occur in cells for generation of variation as seen in rearrangement at immunoglobulin genes via RAG-1-RAG-2 in case of V(D)J recombination or SPO11 mediated double strand breaks in meiosis II.

Lack of repair or incorrect repair leads to genomic anomalies ranging from insertions, deletions, duplication to translocations. This is associated with embryonic death, early aging, genetic disorders, immunodeficiency, neurological disorders and cancer. Moreover, these lesions can block both replication and transcription leading to genome wide aberrations ultimately leading to cell death. Luckily, our cells are equipped with multiple repair mechanisms to carry out appropriate repair of DSBs: homologous recombination (HR), canonical nonhomologous end-joining repair (c-NHEJ), alternative end joining (a-EJ) and single strand annealing (SSA) (Figure 1.1). Of the stated pathways, c-NHEJ and HR are the most utilized pathways for repair of DSBs and thus are extensively investigated. The activation mechanism of DNA repair is not well understood but numerous studies have identified key protein complexes that function in an orderly manner to activate these pathways.

In G1 and early S1 phase, the predominantly active repair pathway is c-NHEJ or simply NHEJ. This pathway in mammalian cells is also the most frequently used pathway throughout the cell cycle. The broken ends of DNA are repaired by sequential recruitment of KU70/80 and DNA-dependent protein kinase catalytic unit (DNA-PKcs) forming the

DNA-PK complex. KU70/80 are abundant in nuclear cytoplasm and show high affinity for DNA ends. In the next step, DNA-PK complex recruits endonuclease Artemis. DNA-PKcs activate Artemis by undergoing autophosphorylation (Goodarzi et al., 2006). This makes the DNA ends compatible for ligation reaction. The ligation machinery composed of XRCC4, ligase IV and KLF is then recruited for re-ligation. This type of repair requires minimal to no resection and may potentially lead to small insertion and deletions. Due to this error-prone nature, NHEJ is required for immune receptor diversification as both V(D)J recombination and class switch recombination (CSR) are mediated by it. Along with core factors as mentioned above the pathway activation is carried out by 53BP1 and its downstream factor RIF1, REV7 and Shieldin complex (Xu et al., 2015; Boersma et al., 2015; Gupta et al., 2018; Dev H et al., 2018; Noordermeer et al., 2018).

Since the error-prone repair by NHEJ can be lethal for cells in late S and G2 phase, HR is activated once the cell has duplicated its genome. This allows for error-free template-based replication. The pathway then begins with extensive resection of DNA ends by exonucleases MRN complex, CtIP, DNA1 and EXO1. This resection termed 'long-range resection' is carried out in two steps. In the first step, a short-range resection (~100 nt) is mediated by MRN-CtIP complex producing a short 3' ssDNA overhang (Sartori et al., 2007; Shibata et al., 2014). *In vitro* studies have shown in absence of CtIP, MRN complex is unable to stimulate DNA end resection (Cannavo et al., 2014; Anand et al., 2016). In the second step, EXO1/DNA2-BLM (5'-3' exonuclease) carry out long range resection. This yields a long stretch of 3' single stranded DNA overhangs on both the side of DSBs. The exposed ssDNA allows for binding of replicative protein A (RPA). In the next step RPA is replaced by another ssDNA binding protein RAD51. This replacement is catalysed by BRCA2-PALB2 complex through a poorly understood mechanism (Yuan et al., 1999). RAD51 then initiates D-loop formation where it invades homologous sequence and accurate repair synthesis is carried out by replicative polymerases. BRCA1 is a key protein involved in many stages of the HR process. It colocalises with DSBs, is known to initiate the resection process and enhances RAD51 recombinase activity. The recombination event follows resolution by either formation of Holliday junction or synthesis dependent strand annealing (SDSA).

In addition to NHEJ and HR, cells have access to two more repair mechanisms viz. alternative end-joining (a-EJ) and single strand annealing (SSA). These mechanisms are only activated if NHEJ and HR are compromised or unavailable and are known to function mainly in S and G2 phase. Interestingly, they share mechanistic features with both NHEJ and HR. Similar to NHEJ these pathways repair DNA DSBs without using sister chromatids. And like HR, these pathways require resection of DNA ends with SSA particularly requiring large stretches of resection. The initial resection machinery is same as for HR that is MRN-CtIP catalysed short range resection. Due to this, these pathways are highly-error prone. Secondly, they show homology-mediated repair with a-EJ requiring fewer base pair homology (2-20 bp) and SSA requiring more than 20 base pair homology. Also, loss of a-EJ causes synthetic lethality in cells deficient in HR. This suggests these pathways function as a backup sort for the two major pathways.

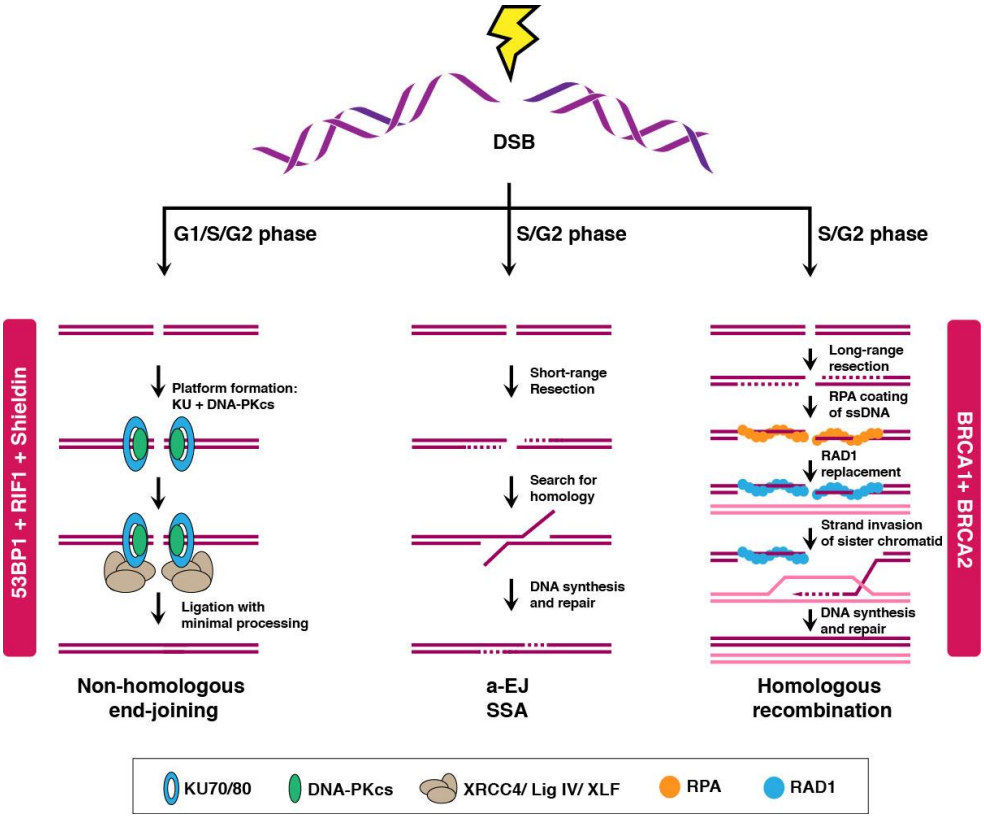

Figure 1.1: Overview of repair pathway choice in DNA repair (Adapted from Noordermeer S. and Attikum H. 2020). continued on next page

Figure 1.1: (continued): DNA DSBs are repaired by two major pathways. NHEJ is active in G1/early S phase and is mediated through the activity of 53BP1-RIF1-Shieldin. KU70/80 form a complex with DNA-PKcs and provide a platform for recruitment of DNA processing enzymes for ligation (see text for details). The broken DNA is ligated by ligation complex consisting of XRCC4-LigIV-XLF with minimal processing. This results in error-prone repair with insertion and deletions. HR is active in late S/G2 phase when duplication of chromosomes is complete and is mediated by BRCA1/BRAC2. Long-range resection is achieved by the concerted action of multiple exonucleases (see text for details) followed by recruitment of RPA on to 3' overhang ssDNA. RPA is replaced by RAD51 which catalyzes strand invasion of sister chromatid commences. Resynthesis of DNA is carried out by replication polymerases to achieve error free repair.

1.1 Control of DNA repair pathway choice

As HR and NHEJ are the two major pathways involved in DNA repair, as such the molecular mechanism behind the regulation of repair pathway choice has been studied for decades (Brandsma and Gent, 2012; Chapman et al., 2012). A key parameter in the pathway choice is the cell cycle. The basic understanding is that HR would require sister chromatids for repair and thus would have to be restricted to S and G2 phase. On the other hand, NHEJ is active throughout the interphase and is only down regulated once the genome is duplicated. The second parameter is the extend of resection on newly formed DNA ends at break sites. The understanding here is that minimally resected ends allow for NHEJ factors to bind whereas, well-resected ends provide high affinity for HR factors. The current model for DNA repair pathway choice revolves around the interplay of two major DNA repair factors (BRCA1 and 53BP1) and how they bring about end resection or end protection.

1.1.1 BRCA1 promotes DNA end resection

BRCA1 is a 190 kDa tumour suppressor nuclear protein that accumulates at DSBs through its phospho-protein binding C-terminal BRCT domain (Scully et al., 1997; Manke et al., 2003; Yu et al., 2003). Although activity of both BRCA1 and BRCA2 is necessary for efficient and complete HR; activation of HR is dependent solely on BRCA1. In mouse models, loss of BRCA1 in cells deficient of 53BP1 resulted in reactivation of NHEJ (Bunting et al., 2010; Bouwman et al., 2010). This shows BRCA1 is necessary for antagonising 53BP1-mediated NHEJ. BRCA1 recruits MRN to generate short 3'-ssDNA overhang (Lamarche et al., 2010) However, its activity is dependent on phosphorylation of CtIP on CDK target motif (Anand et al., 2016). This explains the cell cycle dependence of HR pathway (Escribano-Diaz et al., 2013). Extension of initial short-range resection is necessary for RPA binding. This task is carried out by exonucleases EXO1/DNA2 (Liu and Huang, 2016). MRN complex recruits as well as stimulates EXO1/DNA2 activity at DSBs. Together with MRN-CtIP complex, BRCA1 catalyzes end resection and commits the ensuing repair pathway to HR (Figure 1.2A).

1.1.2 53BP1 promotes DNA end protection

53BP1 (TP53BP1, tumour suppressor p53 binding protein 1) is a key regulator of DSB repair pathway choice (Zimmerman and de Lange, 2014). 53BP1 forms large foci at DNA DSBs which is mediated by ataxia telangiectasia and Rad3-related protein (ATR) and ataxia telangiectasia mutated (ATM) signaling (Bekker-Jensen and Mailand, 2010). 53BP1 is also known to form similar foci at dysfunctional telomeres which have lost Shelterin complex (telomere protection complex) components. The telomeric recruitment of 53BP1 is similarly mediated by ATR and/or ATM kinase (Celli et al., 2005; Takai et al., 2003; Denchi et al., 2007). Dimethylation of K20 of histone H4 is necessary for recruitment of 53BP1. H4K20^{Me2} then interacts with Tudor domain present in 53BP1. Another histone modification identified is the ubiquitylation of H2A (or H2AX) at K15 by RNF168. This specific histone modification is a marker for DNA lesions and itself mediated by

ATR/ATM signaling. 53BP1 recognises H2AK15^{Ub} using a conserved ubiquitin-dependent recruitment (UDR) motif.

Moreover, 53BP1 contains an oligomerization domain (Zgheib et al., 2009). This oligomerization is suggested to strengthen the association with DSBs (Lottersberger et al., 2013). The next immediate factor downstream of 53BP1 is Rap1-interacting factor 1 (RIF1). RIF1 is a genome maintenance protein with diverse roles in DNA metabolism (Buonomo SB, 2010; Yamazaki et al., 2013). Similar to 53BP1, RIF1 recruitment is dependent on ATM/ATR signaling. Recently, it has been shown RIF1 is a phosphopeptide-binding protein and directly binds phosphorylated epitopes present on 53BP1 (Setaiputra et al., 2021). Interestingly, even though RIF1 is recruited at DSBs it is not known whether RIF1 contains any DNA binding activity.

1.1.3 Repair pathway choice and synthetic lethality

Genomic stability is dependent on proper functioning of DDR elements. These responses include the aforementioned NHEJ, HR and single stranded break repair (SSBR) (Chatterjee and Walker, 2017). SSBs are less toxic when compared to DSBs as they do not significantly distort the double helical nature of DNA strands; however, they are relatively abundant and form the basis for synthetic lethality when coupled with HR deficiency in tumours (Caldecott, 2008). Poly (ADP)-Ribose Polymerase 1 (PARP1) is a signaling molecule involved in sensing SSBs. It catalyzes poly (ADP-ribosyl)ation a post translational modification necessary for recruiting DNA damage repair effector proteins at SSB site (Gibson and Kraus, 2012). Recent data has shown PARP inhibitors (PARPi) can inactivate PARP1 and trap the protein onto the damaged DNA (Murai et al., 2012). This causes the single stranded breaks to convert into DSBs during subsequent replication. Also, the trapped PARP1-inhibitor complex on DNA causes difficulty for replication machinery to move past the lesion. To repair these structures, cells require functional HR. However, HR-deficient cells are unable to carry out repair and undergo cell death whereas healthy HR-proficient cells survive. This forms the basis of synthetic lethality (Figure 1.2C). This approach was first described in 2005 and since then clinical studies have shown great

promise (Bryan et al., 2005; Framer et al., 2005; Fong et al., 2009; Mirza et al., 2018). Currently, several PARPi have been FDA- and/or EMA-approved for treatment of BRAC-mutated breast and ovarian tumours (Gourley et al., 2019). However, multiple studies in patients and observations in murine models have shown that response to PARPi treatment is met with high rates of resistance (Rottenberg et al., 2008). Moreover, these resistances coincide with loss of function of 53BP1 suggesting factors controlling repair pathway choice at DSBs also play a key role in synthetic lethality (Figure 1.2 D).

1.2 Discovery of Shieldin complex

Despite their important roles for end resection inhibition both 53BP1 and RIF1 show no enzymatic activity or direct interactions between them. Shieldin complex was discovered simultaneously by multiple research groups as a key downstream factor of 53BP1-RIF1 (Gupta et al., 2018; Dev H et al., 2018; Noordermeer et al., 2018; Ghezraoui et al., 2018). These groups used either CRISPR/Cas9-based genetic screens to identify factors whose mutations elevate PARPi sensitivity in cells deficient of BRCA1, or used apex-based proximity labelling coupled to mass spectrometry (AP-MS). Shieldin is a novel four component complex containing previously identified HORMA domain REV7 and three newly identified uncharacterized proteins C20orf196, FAM35A and CTC.534A2.2. These proteins were named SHLD1 (C20orf196/RINN3), SHLD2 (FAM35A/RINN2), SHLD3 (CTC.534A2.2/RINN1). These seminal studies identified Shieldin recruitment to DSBs to be 53BP1-RIF1 dependent. Since RIF1 binding to 53BP1 is dependent on the cell cycle, Shieldin recruitment to DSBs is therefore also cell cycle dependent. Interestingly, while the loss of SHLD3 leads to loss of REV7 at DSBs, the loss of REV7 did not affect SHLD3 localization to DSBs. SHLD2-SHLD1 co-localization similarly dependent on SHLD3 and REV7. This suggests Shieldin recruitment is hierarchical with SHLD3 recruited first followed by REV7 and SHLD2-SHLD1 (Gupta et al., 2018). Furthermore, SHLD3 recruitment was found to be dependent on ataxia-telangiectasia-mutated (ATM) kinase activity and RNF8-RNF168-dependent recruitment of 53BP1-RIF1 (Gupta et al., 2018). Quantitative mass spectrometry revealed similar abundance of SHLD3 and REV7

suggesting that the pair form 1:1 stoichiometry with strong affinity. This is supported by *in vitro* studies which show that REV7 binds SHLD3 with a strong binding affinity (K_D =15 nM). On the other hand, such a strong interaction strength was not observed for SHLD2 and SHLD1 within Shieldin complex suggesting a unique relationship between SHLD3 and REV7. Of note, the SHLD proteins are not present in prokaryotes and lower eukaryotes (Gupta et al., 2018). Although REV7 is present in all eukaryotes where it forms a part of multiple DNA centric complexes, SHLD1-3 are only found in higher eukaryotes that show capability for class-switch recombination (CSR). This is evident as nurse sharks which show earliest emergence of SHLD proteins show CSR activity. This suggests emergence of CSR recombination in eukaryotes can be attributed to evolution of Shieldin complex (Gupta et al., 2018). Two studies found Shieldin complex at telomeres, where it is involved in telomere length maintenance (Dev et al., 2018; Mirman et al., 2018). Similar to its function in NHEJ, Shieldin loss diminished telomere fusion in TRF2ts experiments (Dev et al., 2018). This experiment utilizes temperature sensitive mutants of telomere capping protein TRF. At elevated temperatures, the mutant gets inactivated and telomeres are unprotected thereby activating repair mechanism. This shows that Shieldin functions genome-wide and is a part of the repair pathways choice at DSBs, CSR and telomeres.

Studies show Shieldin complex can bind DNA. This DNA binding activity is shown to be present in the SHLD2 subunit of the complex (Dev et al., 2018; Gao et al., 2018; Noordermer et al., 2018). To further understand Shieldin architecture, a study carried out domain mapping with truncation experiments and identified that residues 28-83 of SHLD3 are involved in binding REV7 *in vitro*. Similarly, residues 6-11 in the N-terminus of SHLD2 are enough to bind REV7. C-terminal region from residue 650-835 of SHLD2 binds SHLD3 (Gupta et al., 2018; Dev et al., 2018; Gao et al., 2018). This data shows Shieldin is a single physical unit composed of four proteins. Together, these exhaustive studies show that these proteins physically interact with one another and form the effector arm of 53BP1 (Figure 1.2B).

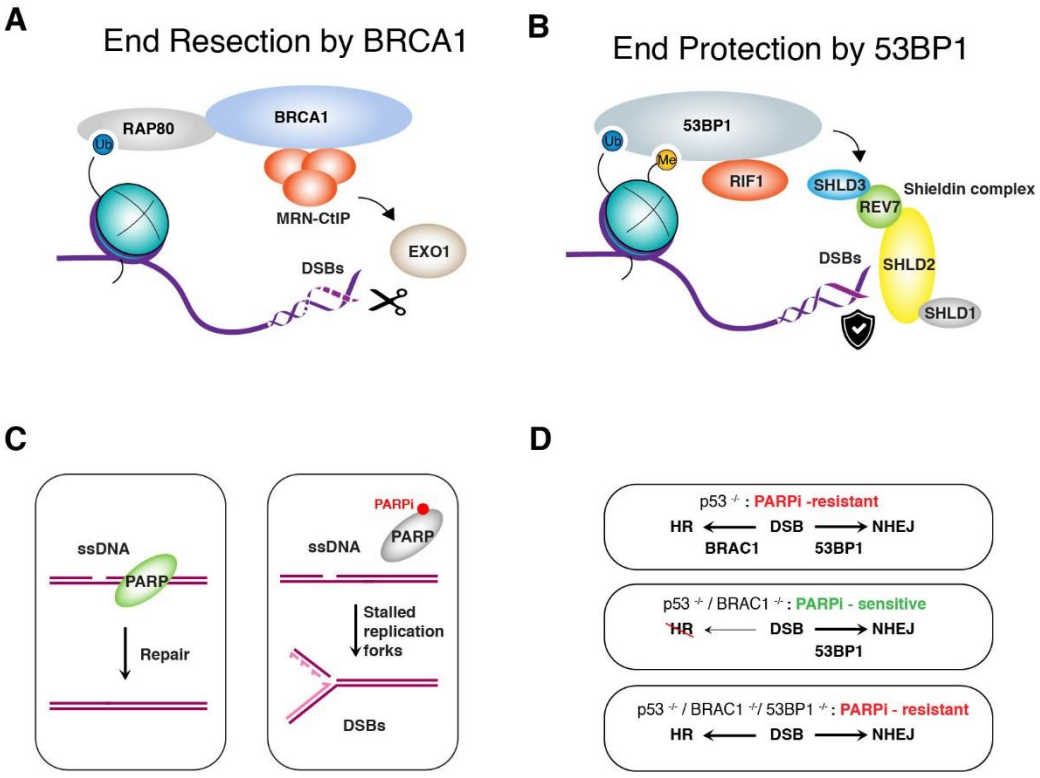

Figure 1.2: BRCA1 and 53BP1 control repair pathway choice. (A) End resection mediated by BRCA1. Histone modification at DNA break site recruit RAP80-BRCA1. BRCA1 forms a complex with MRN-CtIP and stimulate EXO1 for long-range resection of DSBs. This activity commits repair pathway to HR. **(B)** End protection is similarly mediated by histone modification at DNA break site and recruitment of 53BP1-RIF1. Shieldin recruitment and assembly at DSBs blocks resection. **(C)** PARP is involved in DNA damage signaling where its activity is necessary for SSB repair. Inhibition of PARP-by-PARP inhibitors (PARPi) results in conversion of SSBs to DSBs due to stalled replication forks during DNA replication in S phase. **(D)** Cancer cells ($p53^{-/-}$) show PARPi resistance due to functional HR and NHEJ pathways. Loss of BRCA1 inactivates HR resulting in PARPi sensitivity. Further loss of 53BP1 reactivates HR resulting in PARPi resistance.

1.2.1 Shieldin promotes PARPi resistance in BRCA1-defective cells

It has been shown that loss of Shieldin is a factor responsible for PARPi resistance in HR-deficient cells (Gupta et al., 2018; Noordermeer et al., 2018). REV7 was identified as a factor responsible for promoting NHEJ in mouse mammary cells. Loss of REV7 restored HR pathway in tumours derived from *BRCA1*$^{-/-}$ *p53*$^{-/-}$ cells (Xu et al., 2015). Clonogenic survival assays show depletion of SHLD1, SHLD2 and SHLD3 led to resistance to olaparib (PARP inhibitor) in BRCA1-defective cells (Noordermeer et al., 2018; Gupta et al., 2018). Similarly, supplementing Shieldin subunits after depletion caused sensitivity of BRCA1$^{-/-}$ cells to olaparib. The phenotype of SHLD2 depletion was as strong as 53BP1 loss (Noordermeer et al., 2018). These results show tumour cells that have lost Shieldin are able to acquire PARPi resistance. Moreover, the levels of Shieldin complex particularly SHLD1 and SHLD2 subunits correlate to PARPi sensitivity in patient driven xenografts of BRCA1-defective cells propagated in mouse models (Dev et al., 2018). Therefore, Shieldin mediated cytotoxicity of PARPi in BRCA1-defective cells is of clinical relevance. Elucidating how Shieldin complex regulates repair pathway choice will help in understanding one of the many factors responsible for acquired PARPi resistance in certain resistant tumours. It will therefore be of help in providing better therapies in future.

1.2.2 Model for Shieldin function

The current understanding of Shieldin function is that the complex localises to DSBs via the SHLD3-RIF1 interaction (Gupta et al., 2018; Noordermeer et al., 2018). REV7 bridges SHLD3 to SHLD2 by interacting with the conserved motif of SHLD3 and N-terminal region of SHLD2. SHLD2 using its C-terminal OB folds binds ssDNA. SHLD2 then recruits SHLD1 and together are known to block the access of multiple exonucleases to ssDNA ends thereby blocking resection (Gupta et al., 2018; Dev et al., 2018; Noordermeer et al., 2018). However, researchers argue that this mechanism fails to explain why Shieldin complex that inhibits resection binds ssDNA (Setaiputra and Durocher, 2019). It has been

shown *in vitro* that SHLD2 prefers longer ssDNA substrates over shorter (Gao et al., Noordermeer et al., 2018; Dev et al., 2018). Moreover, long stretches of ssDNA are characteristics of resection and not inhibition. The "resection rescue" model thus proposes that Shieldin recruits CST- Pol α complex via its SHLD1 subunit at DSBs and at dysfunctional telomeres (Mirman et al., 2018; Barazas et al., 2018). Pol α then carries out fill-in synthesis wherein ssDNA is re-synthesised to dsDNA. (Miyake et al., 2009; Feng et al., 2017; Wang et al., 2012). Thus, Shieldin functions to reverse the resection caused by any unwarranted exonuclease activity thereby keeping DNA alterations to the minimum and allow for repair by NHEJ (Figure 1.3).

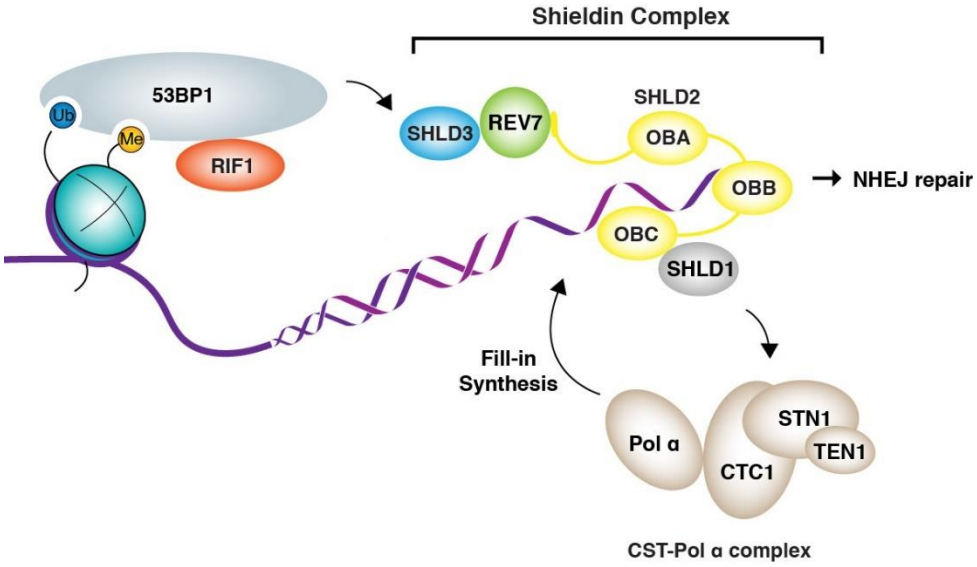

Figure 1.3: Model for Shieldin function. Proposed resection rescue model. In G1/early S phase 53BP1-RIF1 recruit four component Shieldin complex (SHLD1/2/3-REV7) at the broken DNA ends. Using presence of three OB folds (OBA-B-C), SHLD2 binds the ssDNA. This ssDNA binding activity is considered to be a crucial for deciding which pathway will be activated for repair of DNA DSBs. The short-range resection by early exonucleases makes the DNA end unfit for repair by NHEJ. Shieldin then recruits CST-Polα complex via SHLD2-SHLD1 module. Pol α re-synthesizes the resected DNA thereby activating NHEJ pathway.

1.3 Structural elements of Shieldin complex

SHLD1 is the smallest member of Shieldin complex consisting of 205 amino acids. It known to interact with SHLD2 C-terminus (Gupta et al., 2018; Noordermeer et al., 2018; Gao et al., 2018). Its binding to SHLD2 is shown to enhance DNA binding activity of SHLD2 by possibly increasing SHLD2 stability in cells (Gao et al., 2018; Dev et al., 2018). Following the identification of Shieldin as an end resection inhibition factor, it was identified that SHLD1 play a role in recruiting CST-Polα complex for fill-in synthesis (Mirman et al., 2018). Deletion of SHLD1 impairs repair by NHEJ at dysfunctional telomeres. Surprisingly, loss of SHLD1 in Shieldin complex did not compromise CSR and at dysfunctional telomeres suggesting Shieldin might not be strictly necessary for recruitment of CST- Polα complex at the context of CSR and telomeres. Future *in vitro* studies, would be necessary to understand the molecular basis of Shieldin-CST relationship.

SHLD2 is the largest protein in the complex consisting of 835 amino acids and functions as a scaffold in the Shieldin complex. Sequence alignment and 3D structure predictions show the protein consists of a largely unstructured N-terminal region with folded C-terminal region containing presence of three OB folds (Dev et al., 2018; Ghezraoui et al., 2018). OB fold domain A, B, and C are suggested to be involved in ssDNA binding whereas OB fold C is necessary in interaction with SHLD1 (Noordermeer et al., 2018; Dev et al., 2018; Gupta et al., 2018). A report shows SHLD2 binds both ssDNA and dsDNA with preference for longer stretches of ssDNA (Gao et al., 2018). Within the Shieldin complex, SHLD2 interacts with HORMA domain REV7 via a conserved N-terminal motif (Gupta et al., 2018; Ghezraoui et al., 2018). SHLD2 DNA binding activity is shown to be very crucial for Shieldin complex function. SHLD2 fusion with RNF8 an upstream factor of 53BP1 supressed HR in BRCA1$^{-/-}$ 53BP1$^{-/-}$ cells.

SHLD3 is a 250 amino acid containing protein. It is the first subunit of the Shieldin complex that is recruited to DSBs (Gupta et al., 2018). It contains a REV7 binding motif (RBM) at the N-terminus (residue 45-55). The C-terminal region comprising of residues 140 – 250 is predicted to be folded with sequence homology to EIF4-E (Dai et al., 2019).

The middle region comprising of residue 85-135 shows high level of disorder. Recruitment of SHLD3 is thought to be mediated by interaction of its C-terminal folded domain with RIF1 as its colocalization is dependent on 53BP1-RIF1 (Gupta et al., 2018). However, whether such a direct interaction exists is not investigated.

REV7 is a HORMA domain protein. Due to the extensive literature present on the most well characterised HORMA domain MAD2. It will be easier to understand molecular features of HORMA domain proteins using MAD2 as a template. Therefore, the next section elaborates on introduction to these features of HORMA domain proteins.

1.4 HORMA domain proteins

1.4.1 Introduction

HORMA domain proteins were first identified as a set of three divergent proteins present in *Saccharomyces cerevisiae* that were shown to share a common fold. (Aravind and Koonin, 1998). The domain was named after the three first members that were identified: meiotic recombination regulator HOP1, the DNA repair factor REV7 and the spindle assembly checkpoint (SAC) protein MAD2. Since then, additional HORMA domains have been identified. These include another SAC protein $p31^{comet}$, and two autophagic proteins ATG13 and ATG101. In 2015, putative HORMA domain proteins were discovered in bacteria using comparative genomic analysis (Burroughs et al., 2015). These were shown to be bona fide HORMA domain proteins where they mediate bacteriophage immunity (Ye et al., 2020). Biochemical and functional studies on MAD2 in the years from 2000 – 2008 revealed a set of principles that govern the function of HORMA. (Mapelli et al., 2006; Mapelli et al., 2007, Sironi et al., 2002, Simonetta et al., 2007., Vink et al., 2006., Yang et al, 2007; Mapelli and Musacchio, 2007; Ye et al., 2015). The subsequent studies on SAC activation revealed the linchpin role HORMA domain MAD2 plays in the controlled assembly of mitotic complex thereby, serving as a unique signaling node. Whether these principles are applicable to other HORMAs has not been investigated. In general, these studies lay out a developing picture of HORMA domain proteins existing as two

topologically distinct states which convert from one state to another (Rosenberg and Corbett, 2015). This conversion can also happen spontaneously but with extremely slow rates. This is due to requirement of high activation energy of conversion. Open state of HORMA is the inactive state which converts to a protein bound closed state. It is in this closed state, HORMA is known to be catalytically active and can initiate signaling. Once bound to its partner, this active state needs to be disassembled in order to silence its signaling activity. This is carried out by a conserved AAA+ ATPase remodeler Pch2/TRIP13. The bacterial HORMAs were also found to be present in an operon together with AAA+ ATPase TRIP13. Thus, HORMA domain proteins and TRIP13 together constitute an evolutionary conserved functional module. This also shows the HORMA-TRIP13 signaling module is of archaic origin.

1.4.2 Structural features of HORMA domain

HORMA is a small protein domain consisting of roughly 200 amino acids. The domain consists of a rigid core consisting of three α-helices (αA, αB, and αC) sandwiched between β-sheets (β4, β5, and β6 on front and β2, β3 hairpin on back) (Figure 1.4). Flanking the core are the N- and C-terminal regions which are mobile. Depending on the different position of the C-terminal region relative to the core, the HORMA adopts either a closed state or an open state. When the C-terminal region folds into two β-strands (β7 and β8), the HORMA is said to be in the open state. While if the C-terminal region folds in two new β-strands (β8' and β8'') the HORMA is said to be in the closed state. When forming the β8' and β8'' strands, the C-terminal region appears to wrap around the core domain and in doing so can trap/capture a short peptide (called the closure motif) from a binding partner. The bound peptide is embraced by the C-terminal region and hence it is also termed as the safety-belt region (see topology diagrams, Figure 1.4A). In case of MAD2, the consensus motif consists of following sequence K/RψψxφxxxP, where K/R is a lysine or arginine; ψ is an aliphatic residue, φ is a hydrophobic residue and P is a proline. For both MAD2 and REV7 these sequences are present on their binding partners however, In HOP1 and p31^{comet} the closer motif is present at their C-terminal region. For the autophagy

HORMA domain proteins ATG101 and ATG13, these conserved sequences have not been identified. In solution, MAD2 open and closed states have different thermodynamic stability with reports suggesting, the closed MAD2 bound to closure motif state is thermodynamically more stable when compared to open MAD2 (Figure 1.4B).

Another key feature associated with HORMA domain proteins is the ability to undergo homo and hetero dimerization using a distinct dimer interface. This dimer interface lies mainly on helix αC of the HORMA domain core. This is well studied in MAD2, which can form both homodimer and a heterodimer with $p31^{comet}$ (Figure 1.4C). MAD2 forms topology sensitive dimer (also called conformational dimer) wherein one protomer is open conformer (O) and the other protomer is closed (C). (Mapelli M. et al., 2007). This conformational dimer is necessary for assembly of MCC complex (Mapelli et al., 2006; Simonetta et al., 2007; Vink et al., 2006). Apo MAD2 can also form closed-closed (C-C) homodimer (Yang et al., 2007). Despite presence of no MAD2 dimer in MCC, point mutations in the dimer interface abolished MCC assembly completely suggesting MAD2 dimerization is necessary for MCC assembly (Mapelli et al., 2006; Mapelli et al., 2007). MAD2 similarly forms a closed: closed heterodimer with $p31^{comet}$. This dimer is necessary for disassembly of MCC by AAA+ ATPase TRIP13 (Yang et al 2008), and introduction of point mutants in the dimer interface of MAD2 abolishes its disassembly by TRIP13 (Ye et al., 2015). This show that MAD2 dimer mutants can also keep the SAC in permanent mitotic arrest. Similar to MAD2, other HORMA domain proteins are also known to dimerize. REV7 can form homodimer in solution or when bound to REV3 (Rizzo et al., 2018). Recent Cryo-EM structure revealed exists as a REV7 dimer in yeast DNA polymerase ζ (Malik et al., 2020). It is unclear whether the dimer formation in DNA polymerase ζ happens via the dimer interface. Structural analysis of the autophagy HORMAs show that ATG13 and ATG101 form similar closed-open dimer where ATG13 is present as a closed protomer while ATG101 as an open protomer (Qi et al., 2015). Though functional studies on REV7 and autophagic HORMAs are warranted, it is clear that HORMA dimerization is a key aspect of their function. The only HORMA that is not known to dimerize are the meiotic HORMADs.

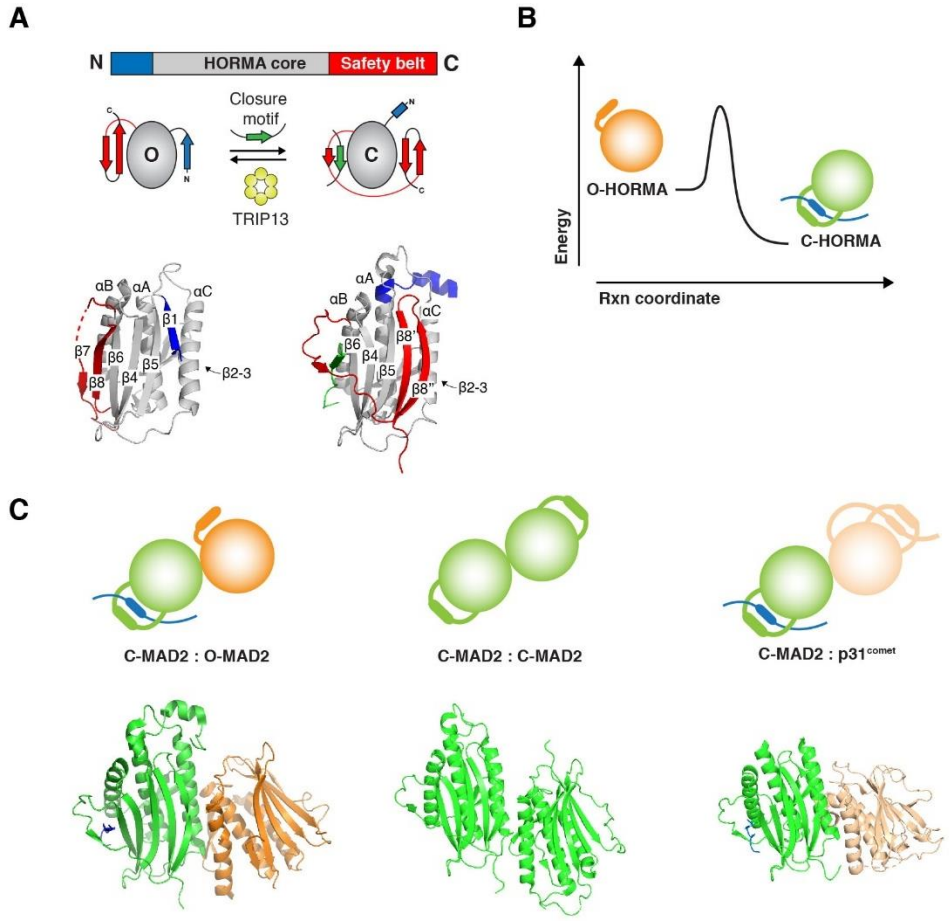

Figure 1.4: Mechanism of HORMA domain signalling by MAD2. (A) Cartoon representation of MAD2 conformational states and interconversion. MAD2 exists as two distinct topologies with different N- and C-terminal arrangements against the core β-sheet (grey); O-MAD2 and C-MAD2 are shown on either side [PDB: 2V64]. Conversion is slow but spontaneous and in presence of closure motif allows its capture by MAD2. The reverse conversion is catalysed by a conserved AAA+ ATPase TRIP31. **(B)** Energy profile illustrating MAD2 conformer stability. O-MAD2 is characterized to be less stable as compared to C-MAD2 bound to CDC20. The high activation energy requirement makes the topological switch under physiological conditions very slow. **(C)** MAD2 dimerization**.** C-MAD2 (green) undergoes asymmetric homodimerization with O-MAD2 (orange) [PDB: 2V64], symmetric homodimerization with C-MAD2 (green) [PDB: 2VFX], and asymmetric heterodimerization with $p31^{comet}$ (wheat) [PDB: 2QYF]. In all the cases, HORMA dimerization involves residues present on αC helix.

1.4.3 Spindle Assembly Checkpoint: MAD2 Case study

For faithful segregation of chromosomes into daughter nuclei, the kinetochore-microtubule attachment is “very” crucial. Lack of proper attachment follows unequal segregation of chromosomes. This causes aneuploidy resulting in various genetic defects and ultimately leads to cell death. In healthy cells, the spindle assembly checkpoint (SAC) monitors the accurate kinetochore attachment. MAD2 is a crucial part of the SAC response, where it assembles the soluble mitotic cell checkpoint (MCC) complex. MAD2 in a unique but conserved fashion binds a conserved peptide region on CDC20. This leads to sequestering of CDC20 by MAD2 in MCC. The assembled MCC then inhibits the E3 ubiquitin ligase APC/C (the anaphase-promoting complex/clyclosome). Once all the kinetochores are stably attached, the formation of new MCC ceases. The disassembly of existing MCC leads to release of CDC20 which then activates APC/C for degradation of cell-cycle specific proteins. This leads to mitotic exit and progression to anaphase. MAD2, thus plays a key role in safeguarding genome integrity (Figure 1.6). Further sections describe in detail how MAD2 carries out this task using structural plasticity of its HORMA fold.

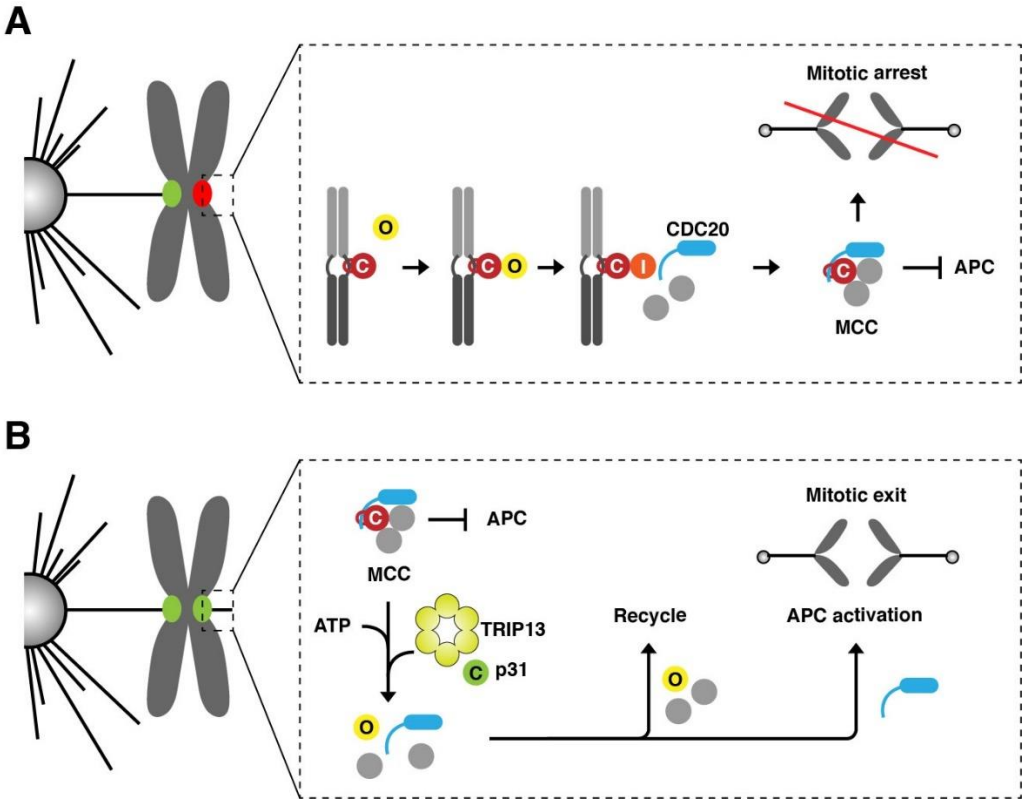

Figure 1.6: HORMA MAD2 in spindle assembly checkpoint signaling. (A) SAC signaling is initiated when kinetochore remain detached. MAD1:C-MAD2(grey and red) recruit O-MAD2(yellow) and assemble MCC which inhibits APC/C activity. The recruitment of O-MAD2 follows transient dimerization with C-MAD2 in which O-MAD2 first converts to I-MAD2 which readily binds CDC20 MIM. Once MAD2 captures CDC20 the MCC assembly is complete which then inactivates APC/C. **(B)** When kinetochores are properly attached MCC production stops and TRIP13: $p31^{comet}$ activity disassemble CDC20: C-MAD2/MCC to produce free CDC20 and O-MAD2. CDC20 then activates APC/C and promotes mitotic exit.

1.4.4 MCC assembly: SAC activation and the template model

Kinetochores devoid of attached microtubules retain a copy of C-MAD2 bound to SAC protein MAD1 (Antoni et al., 2005; Luo et al., 2002; Vink et al., 2006). MAD2 is bound to MAD1 in a way analogous to CDC20 using the same safety belt interaction (De Antoni et al., 2005; Sironi et al., 2002). The MAD1: C-MAD2 complex functions to recruit soluble

free O-MAD2 for CDC20 binding. For MCC assembly, docking of O-MAD2 onto C-MAD2 bound to MAD1 is necessary. This happens through MAD2 (O-C) conformational dimer formation (Mapelli M. et al 2007). In this bound state, O-MAD2 is more readily able to bind CDC20 closure motif and thus assembles MCC with faster rate (Simonetta et al., 2007; Vink et al., 2006). Later, it was shown that MAD1:C-MAD2 present at kinetochore acts as the catalyst for an even faster assembly of MCC (Faesen et al., 2017). By combining these findings, a simple yet elegant model was put forth by Musacchio and colleagues (Figure 1.7A). The template model proposes that O-MAD2 is activated by a catalyst MAD1: C-MAD2 present at the kinetochores. C-MAD2 acts as a template for conversion of O-MAD2 and binding CDC20 for MCC assembly. This MAD1: C-MAD2 catalyst driven conversion of MAD2 assembles MCC in a matter of minutes whereas uncatalyzed conversion of MAD2 for MCC assembly takes hours (Figure 1.7B).

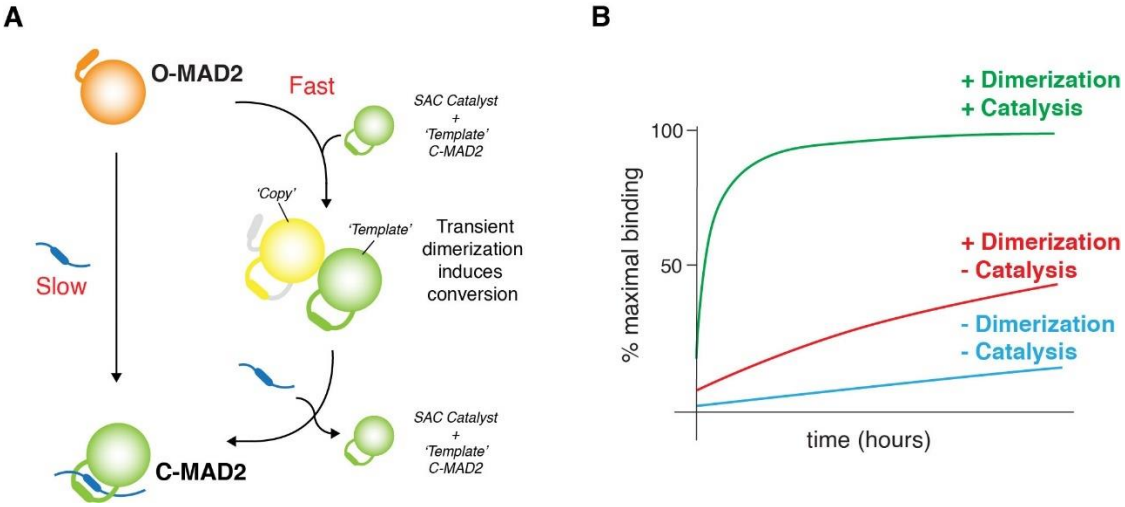

Figure 1.7: Assembly of MCC is governed by MAD2 dimerization (A) Schematic illustration of template model for MAD2 conversion. MAD2 conformational dimerization is necessary for assembly of MCC and inhibition of APC/C for mitotic arrest. In absence of dimerization, MAD2 binds CDC20 (blue) slowly. **(B)** Effect of MAD2 dimerization and external catalyst on assembly kinetics. In absence of catalyst and ability to dimerize MAD2 shows reduced binding kinetics to CDC20 due to spontaneous conversion from open to closed (blue curve). MAD2 dimerization slightly enhances binding kinetics to CDC20 (red curve). The presence of external catalyst enhances MAD2 binding to CDC20 instantaneously (green curve).

1.4.5 TRIP13 and p31^{comet} mediated disassembly of HORMA domains

1.4.5.1 MCC disassembly

The disassembly of MCC is carried out by a conserved hexameric AAA+ ATPase TRIP13 in mammals (Miniowitz Shemtov et al., 2015; Eytan E et al., 2014). However, TRIP13 alone shows limited activity towards C-MAD2:CDC20 and can only convert limited C-MAD2 to O-MAD2 (Ye et al., 2015). The targeting of C-MAD2 bound complexes to TRIP13 is achieved by an adaptor molecule p31^{comet}. p31^{comet} role in inactivation of MCC was known even prior identification of TRIP13 as an active component of MCC disassembly (Xia et al, 2004; Teichner et al, 2011; Westhrope F. et al 2011). p31^{comet} is able to tether HORMA remodeller TRIP13 and MAD2 and so can enhance TRIP13's activity towards MAD2 (Figure 1.8 A and B). p31^{comet} heterodimerizes with MAD2 utilizing MAD2 dimer interface and interacts with N-terminal domain (NTD) of TRIP13 using lysine K100 and K110 (Yang et al., 2007; Ye Q. et al., 2017). Further, mutation of these residues abolishes TRIP13 and p31^{comet} interaction (Ye et al., 2015). The molecular mechanism of MCC disassembly is as follows, the cycle begins with heterodimerization of C-MAD2:CDC20 and p31^{comet} using the HORMA dimer interface (Yang et al 2007). CDC20:MAD2: p31^{comet} complex then interacts with NTD of TRIP13 (Ye et al., 2015). Binding of p31^{comet}: MAD2:CDC20 complex to TRIP13 positions C-MAD2 closer to the pore region of TRIP13. The residues present in pore loop regions of TRIP13 can than interact with the N-terminus of MAD2. The repeated ATP hydrolysis by TRIP13 allow the monomeric subunits to "pull" the N-terminus of MAD2. This pulling through the hexamer pore resulting in the unwinding and stretching of the polypeptide chain of αA helix. This results in partial conversion of C-MAD2 (unbuckled state) and release of CDC20 from safety-belt interaction. Further unwinding by TRIP13 converts C-MAD2 to O-MAD2. Since p31^{comet} specifically interacts with C-MAD2 (Xia et al, 2004; Yang et al, 2007), on unfolding of C-MAD2 to O-MAD2, the dimer becomes unstable and ternary complex of

TRIP13:MAD2: p31^{comet} destabilizes leading to complete disassociation (Ye Q. et al., 2017; Alfieri et al., 2018) (Figure 1.8 C). The free p31^{comet} / TRIP13 can now target next MCC molecule for disassembly. Other than MAD2, TRIP13 and p31^{comet} are shown to target HORMA domain HOP1, REV7 and bacterial HORMAs. In *S.cerevisiae*, Pch2/TRIP13 directly interacts with HOP1 (Chen et al 2014). Though it is known to disassemble meiotic HORMADs, the exact molecular details are unknown (Börner et al., 2008; Wojtasz et al., 2009; Chen et al 2014).

1.4.5.2 Shieldin disassembly

Since REV7 and MAD2 are structurally similar and assemble into complexes by binding to partner proteins via safety belt, their disassembly would also follow similar mechanism. Unsurprisingly, a study set out to find additional REV7 binding partners identified AAA+ ATPase TRIP13 using tandem-affinity-tagged REV7 coupled to mass spectrometry (Clairmont et al., 2020; de Krijger et al., 2021). Authors found Shieldin complex subunits could co-elute with TRIP13 and vice versa. TRIP13 acts as a negative regulator for REV7 and antagonizes Shieldin activity in cells. Additionally, upregulation of TRIP13 activity disrupted Shieldin activity and therefore, inactivated NHEJ leading to fusion of telomeres in G1 phase. However, this activity did not interfere in 53BP1 and RIF1 foci formation suggesting TRIP13 functions downstream of 53BP1-RIF1. Furthermore, TRIP13 enhances end resection and promotes HR. It is unclear how exactly TRIP13 at molecular level enhances end resection. TRIP13 is also shown to affect REV7-REV3 interaction and negatively regulate Pol-ζ activity. This shows that TRIP13 might serve as a negative regulator for multiple REV7 containing complexes. TRIP13 *in vivo* is shown to disassembly REV7-SHLD3/REV7-REV3 it is unclear whether REV7 reverts to open state (Figure 1.8 D). Also, TRIP13 activity towards MAD2-CDC20 is limited without adaptor protein p31^{comet} (Ye et al., 2015). Such a measurement of TRIP13 activity towards REV7 is lacking. A recent study showed involvement of p31^{comet} in Shieldin/ Pol-ζ disassembly (Sarangi et al., 2020). In cells p31^{comet} was found to be associated with all Shieldin complex subunits. Moreover, p31^{comet} binds to REV7 using its dimer interface in a way similar to

MAD2. The authors showed that p31 is a negative regulator of Shieldin similar to TRIP13 in cells however, showed limited *in vitro* experiments. A disassembly assay with purified components would be required to answer this. With Pol-ζ containing two copies of C-REV7 and reports suggesting C-REV7 can dimerize within the same complex (Rizzo et al., 2018) it is unclear whether disassembly of Pol- ζ and Shieldin follows similar molecular mechanism like one for MAD2 or different. Also, *in vitro* proof of direct interaction between REV7 and $p31^{comet}$ is lacking. In MAD2 disassembly, TRIP13 action on N-terminus of MAD2 breaks H-bonding between αA and β8''. Such an interaction network in REV7 is missing and replaced by hydrophobic interaction (Ye et al., 2017). It is unclear whether REV7 can be disassembled or not with TRIP13 alone or TRIP13-$p31^{comet}$ and thus warrants thorough *in vitro* study (Figure 1.8 D).

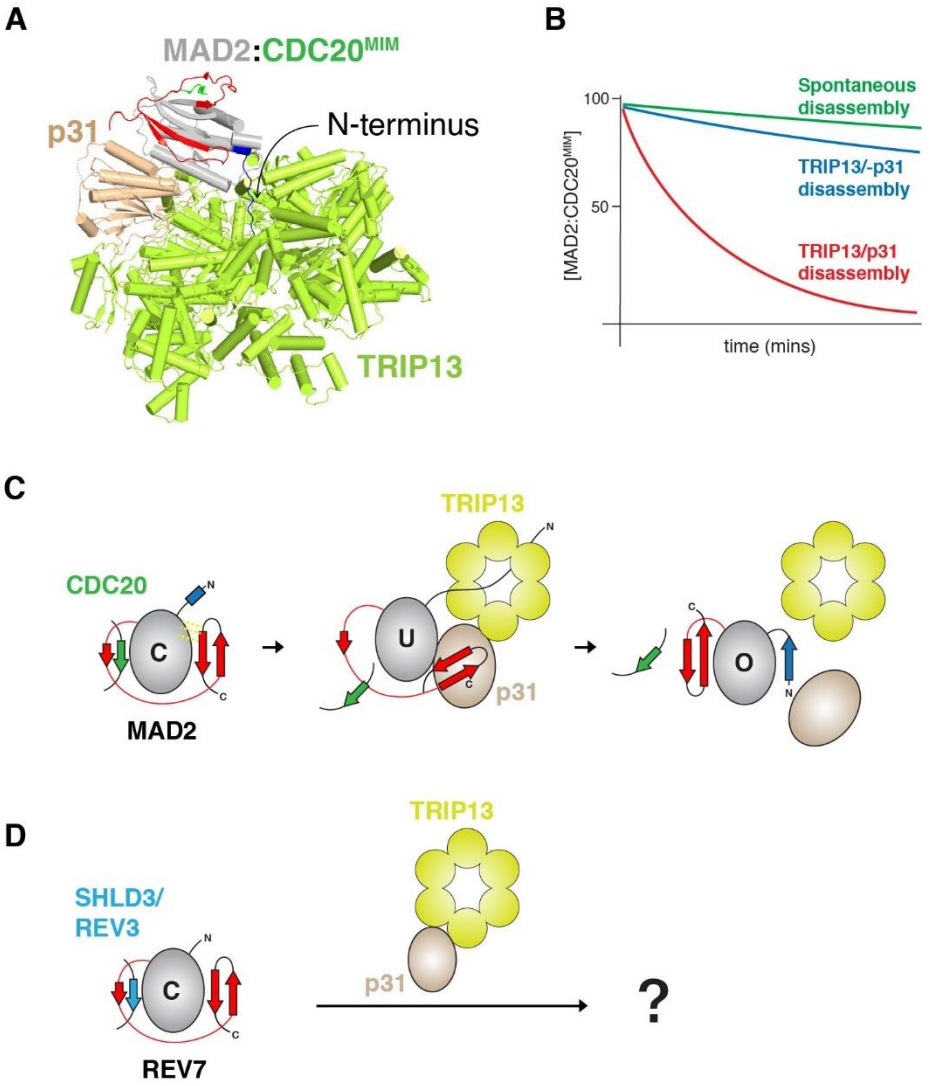

Figure 1.8: Disassembly of HORMAs by hexameric AAA+ ATPase TRIP13 and p31^{comet}. (A) Cryo-EM structure of C-MAD2:CDC20: p31^{comet} (grey, green and wheat respectively) bound to TRIP13^{EQ} (lime) in catalytic active state (Alfieri et al., 2018) [PDB: 6F0X] **(B)** Effect of TRIP13/p31^{comet} on MCC disassembly for exit from mitotic arrest. Spontaneous conversion of C-MAD2 to O-MAD2 and release of CDC20 is very slow resulting in mitotic arrest by SAC detrimental for cell. Presence of TRIP13 alone minimally affects disassembly. TRIP13 with cofactor p31^{comet} speeds up disassembly dramatically. **(C)** Schematic illustration of MCC complex disassembly by TRIP13 and p31^{comet}. C-MAD2:CDC20$^{MIM/closure\ motif}$ undergoes heterodimerization with another HORMA p31^{comet} using dimer interface. C-MAD2:CDC20^{MIM}: p31^{comet} interact with TRIP13. TRIP13 catalyses disassembly of MCC by pulling on N-terminus

of MAD2. This breaks H-bonding interaction of residues in αA and β8'' in C-MAD2 (yellow dots) and converts MAD2 to open conformation. TRIP13:C-MAD2:CDC20^{MIM}: p31^{comet} complex then falls apart and can resume disassembly of the next MCC molecule. **(D)** REV7 disassembly mechanism is proposed to be similar to MAD2.

1.5 REV7 is a multifaceted HORMA

REV7 is a HORMA domain consisting of 200 amino acids. It is abundant in nucleoplasm and has a large number of binding partners that bind through both safety-belt and non-safety belt interaction (de Krijger, Boersma, and Jacobs et al., 2021). Thus, REV7 is involved in multiple distinct nucleo-centric pathways. The following section elaborate the role REV7 plays in these pathways.

1.5.1 REV7 in Shieldin complex

REV7 was first identified to regulate repair pathway choice through a functional genetic screen at both human telomeres and DNA double strand break. Moreover, REV7 was identified to be necessary for inhibiting end resection and for promoting CSR (Boersma et al., 2015; Xu et al., 2015). Loss of REV7 shows a similar phenotype as loss of 53BP1 in BRCA1-deficient cells. REV7 is able to interact with SHLD2 using REV7 interaction motif (RIM) (Gupta et al., 2018). It was also found that REV7 binds SHLD3 and SHLD2 using two distinct surfaces (Ghezraoui et al., 2018). Thus, in Shieldin complex REV7 bridges SHLD3-RIF1 assembly arm to SHLD2-SHLD1 ssDNA binding effector arm.
Structural studies on HORMA REV7 shows REV7 adopts a MAD2 like fold (Hara et al., 2007). At the time of this writing 32 structures of REV7 / REV7 containing complexes have been deposited to the PDB. Phylogenetic analysis show REV7 is the most related to MAD2. This can be seen from structural similarity between the two. Closed conformer of REV7 looks similar to C-MAD2 (Figure 1.8). Similar to MAD2, REV7 binds partner protein containing REV7-binding motif (RBM) in safety belt conformation. For REV7, a

similar consensus sequence exists in form of xψψxPxxxpP, where p is a less conserved proline (de Krijger, Boersma and Jacobs, 2021; Clairmont and D'Andrea, 2021). (Figure 1.5). Crystallographic studies show REV7 binds SHLD3 in a safety-belt conformation (Dai et al., 2019). To date there is no structure of open REV7 however, since REV7 binds REV3/SHLD3 in a closed state, it is likely to assume an open state. *In vitro* studies show REV7 can form dimer in solution. Similar to MAD2 dimer interface, REV7 also shows presence of dimer interface composed of αC and β8''. In addition to this, the short β-sheet hairpin (β4) is also involved in REV7 dimerization (Rizzo et al 2018). The dimer interface shows multiple key residues to be involved in REV7 dimerization. A report identified several residues of REV7 (E35, V39, K44, R124, V132, D134, A135) to be involved in dimerization using yeast two hybrid screening (Rizzo et al., 2018). Yeast two-hybrid study suggests REV7 can dimerize with $p31^{comet}$ similar to MAD2 suggesting shared model for disassembly for HORMA domains by AAA+ ATPase TRIP13.

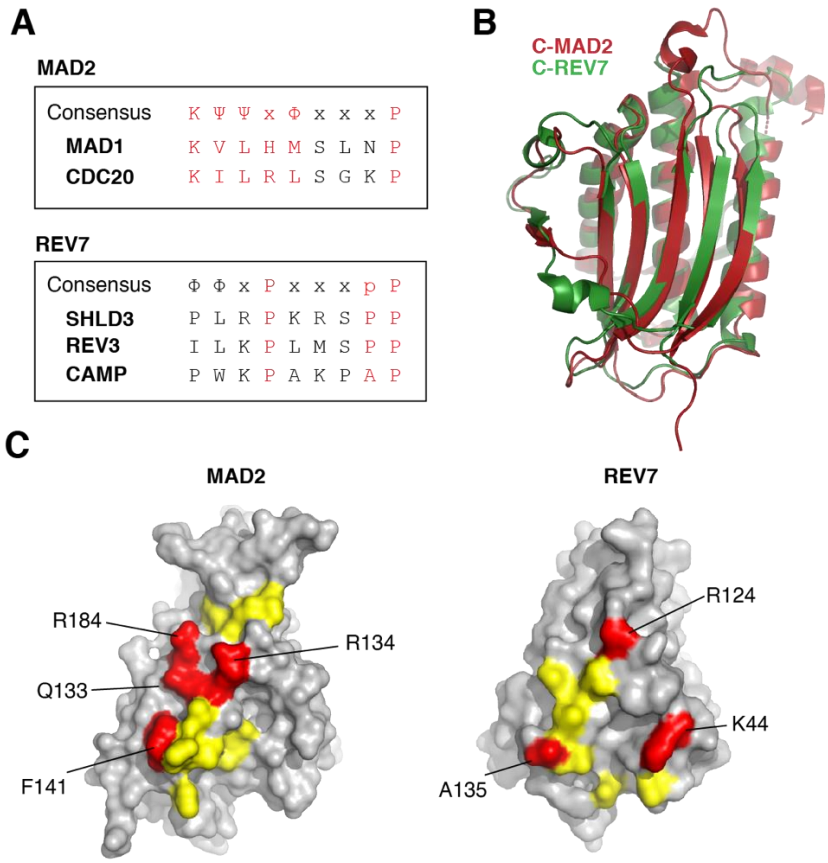

Figure 1.8: HORMA domain REV7 and MAD2 are structurally similar. (A) Schematic representation of consensus sequence motif present for MAD2 and REV7 binding in safety belt conformation. **(B)** Structural alignment of C-MAD2 [PDB:2V64] and C-REV7 [PDB:3ABD]. **(C)** Dimer interface consisting of αC helix of MAD2 and REV7 (as shown in B) contain key residues (red) shown to be involved in homo/hetero dimerization.

1.5.2 REV7 in DNA polymerase ζ

Unlike in Shieldin complex, REV7 has been studied extensively in the context of translesion synthesis and Fanconi Anaemia (Bluteau et al., 2016; Kim et al., 2012; Hara et al., 2010). In these pathways, REV7 is involved in assembly of DNA polymerase ζ which

is an extender polymerase. REV7 coordinates the activity of pol- ζ with another polymerase REV1 which serves as an inserter polymerase (Prakash et al., 2005; Waters et al., 2009) Together, pol- ζ and REV1 carry out DNA synthesis past damaged bases by first inserting bases opposite a lesion (REV1 activity) and then extending it further (REV3 activity) (Figure 1.9 A). In pol- ζ, two REV7 molecules bind REV7 interacting regions (RIR) present on REV3 (residues 1,877-1,898 and 1,993-2,003) (Hara et al., 2010, Tomida et al., 2015). Structural studies have shown that REV7 binds both RBMs present in RIR of REV3 in the safety belt conformation similar to how MAD2 binds CDC20 (Hara et al., 2010, Rizzo et al., 2018) (Figure 1.9 B). REV1 binds REV7 at the β8' and β8'' which are part of the close conformation, suggesting REV1 can only be incorporated after closure of REV7 on REV3 RBMs (Xie et al 2012; Kikuchi et al., 2012; Wojtaszek et al., 2012). A recent Cryo-EM structure confirms presence of REV7 dimer in yeast Pol ζ (Malik et al., 2020). Surprisingly, the dimer of REV7 present in pol ζ differs from canonical HORMA dimer present in MAD2 (Figure 1.9 C). These REV7 protomers do not use dimer interface for dimerization. The REV7 dimer assumes a noncanonical head-to-tail arrangement which differs from C-MAD2:O-MAD2 head-to-head arrangement. Similar study showed REV7 able to form head-to-head arrangement with $REV3^{RIR}$ of human Pol ζ (Rizzo et al., 2018). However, both human and yeast pol- ζ can incorporate only a single copy of REV1. Another possibility is that REV7 would undergo dimerization for faster assembly of pol-ζ however the dimer would break in order to incorporate REV1 for the insertion polymerase activity. This would suggest the yeast Cryo-EM structure arrangement of REV7 would be the final state of REV7 in pol ζ. These studies show the central role REV7 plays in assembly and function of DNA polymerase ζ and how structural plasticity of REV7 is key for assembling multi-polymerase complexes.

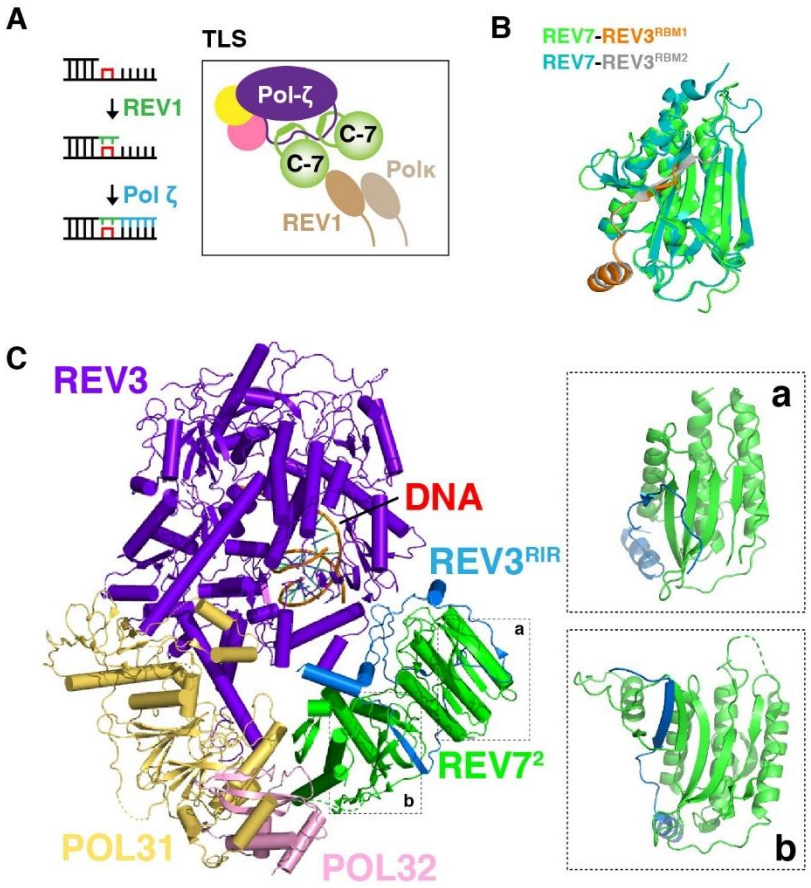

Figure 1.9: Architecture of DNA polymerase ζ. (A) Schematic representation of TLS pathway coordinated by activities of Y-family inserter polymerase (REV1, Polκ, Polη, Polι) and extender polymerase Pol ζ (REV3, REV7, POL31 and POL32). Inserter polymerases interact extender polymerases through the REV7 subunit (shown in box). **(B)** Superimposed structures of REV7-REV3^{RBM1} (green and orange) [PDB:3ABD] and REV7-REV3^{RBM2} (cyan and grey) [PDB: 6BC8]. **(C)** Cryo-EM structure of *S.cerevisiae* Pol ζ holoenzyme coloured by domain [PDB: 6V8P]. Similar to human Pol ζ, yeast Pol ζ shows presence of two C-REV7 protomers (enlarged in panels a and b).

1.5.3 Additional REV7 containing complexes

Previously, REV7's role in mitosis was attributed to interaction with CDH1 and thereby as an inhibitor of APC/C and (Pfleger et al., 2001., Chen et al., 2001; Listovsky et al.,

2013). However, CDH1 lacks REV7-binding motif and has recently shown to interact with REV7 in REV1-like manner (Pernicone et al., 2020). Interestingly, REV7 forms distinct foci in mitotic cells away from CDH1. This suggests REV7 to be involved in a completely new pathway associated with spindle formation and chromosome alignment (Bhat et al., 2016). A study showed REV7 interacts with kinetochore-microtubule specific protein CHAMP1 (also known as ZNF828, C13orf80, or CAMP) (Itoh et al., 2011; Vermeulen et al., 2010). Further, a structural study has shown that REV7 binds CHAMP1 via safety belt conformation similarly how REV7 binds REV3 and SHLD3 (Hara et al., 2017). Similar to REV3 and SHLD3, CHAMP1 contains REV7 binding motif which show presence of conserved prolines. In addition to RBM, CHAMP1 also contains a highly conserved WK motif upstream of the conserved proline. Mutation of conserved prolines or WT motif alone cause loss of interaction; suggesting the REV7 can accommodate peptides of different sequences and different specificities. This also points out at possibly different form of REV7 binding to CHAMP1. Role of CHAMP1 is not well understood and reports suggest CHAMP1 is involved in kinetochore-microtubule interactions. A recent study suggests CHAMP1 along with REV7 is involved in DNA repair regulation. High levels of CHAMP1 favoured HR repair pathway in cells subjected to DNA DSBs using high doses of UV radiation (Li et al., 2021). Moreover, CHAMP1-REV7 complex formation is crucial for activation of HR pathway. The authors suggest CHAMP1 sequesters REV7 from actively forming Shieldin complex or Pol-ζ. Thus, its acts as a negative regulator for REV7 activity in DNA repair.

GTPase Ras-associated nuclear protein (RAN) is an upstream regulator of REV7 (Medendorp et al., 2009). A recent crystal structure identified REV7-RAN interaction to be similar to REV7-REV3/SHLD3/CHAMP1. REV7 embraces the RBM present on RAN (residue 175-186) in safety belt conformation. REV7 binds RAN in both its GTP-bound and GDP-bound form however, shows higher affinity for GTP-bound state (Wang et al., 2019). This work suggests presence of mitotic regulation of REV7 in inhibiting APC/C via CDH1. Whether the same mechanism is present for other REV7 mediated pathway is currently not known. Interestingly, this process draws stark convergence with MAD2 which is regulated by Ras GTPase RIT1 in mitosis (Cuevas-Navarro et al., 2021). This

shows HORMA domain proteins which regulate major pathways with their active states are in turn under tight regulation themselves providing another layer of regulation.
An interesting example of HORMA domain targeted by pathogen effector is *Shigella* Invasin IpaB. This protein contains a RBM on its N-terminal region (residues 61-70) which is able to interact with REV7. It locks REV7 in a closed conformation via safety-belt interaction (Wang et al., 2019). Interaction of IpaB with REV7 is thought to sequester active REV7 in cells thereby modulating REV7 activity negatively in mitosis. This leads to disruption of the cell cycle through a poorly understood mechanism. This causes inappropriate cell cycle arrest promoting bacterial colonization of intestinal epithelium (Iwai et al., 2007). This is particularly opposite as seen in bacterial HORMAs which are involved in antiphage immunity and function as protein sensing defence system (Ye et al., 2020).

1.5.4 Questions regarding the mechanism of Shieldin assembly

We lack a mechanistic understanding of processes such as recognition of DNA by Shieldin and its assembly. Also, given the important role MAD2 plays in MCC assembly, it is likely REV7 plays a similar role in Shieldin assembly. Moreover, it is unclear whether Shieldin complex subunits themselves are sufficient for this. The following questions remain to be answered:

- **What is the stoichiometry of the Shieldin complex?** REV7 is a HORMA domain protein within Shieldin complex. Given that HORMA domains can form dimers and REV7 exists as a dimer in Pol ζ, it is unclear whether REV7 exists as a dimer in Shieldin.

- **Can REV7 adopt topologically distinct states?** REV7 and MAD2 are structurally very similar. Similar to MAD2, REV7 is known to be present in closed state. Whether an open state similar to MAD2 exists, is currently unclear.

- **Does REV7-SHLD3 interaction follow slow binding kinetics?** The safety-belt interaction between MAD2 and CDCD20 makes the binding very slow due to the requirement of considerable activation energy for topology switch. Similarly, REV7 binds SHLD3 RBM in a safety belt conformation. It is unclear whether REV7-SHLD3 interaction *in vitro* shows similar slow binding.

- **What is the function role of SHLD3 in Shieldin complex?** SHLD3 is the first subunit to localise at DSB. In cells, SHLD3 is known to recruit REV7-SHLD2 at DSBs using RBM present at its N-terminus, yet its precise function in Shieldin mechanism remains unclear.

However, these questions cannot be addressed in cells. In this thesis, I aim to address aforementioned questions by reconstituting Shieldin complex using purified proteins with a key focus on HORMA aspects of REV7 particularly studies on topology and kinetics of interaction.

1.6 Aim and thesis outline

HORMA MAD2 mediated assembly of MCC is cooperative and the safety-belt binding between MAD2-CDC20 shows small on rates *in vitro* (Sironi et al., 2002; Simonetta et al., 2007). A similar safety-belt binding is identified in Shieldin complex between HORMA REV7 and SHLD3 (Dai et al., 2019). Whether Shieldin assembly is also cooperative and slow *in vitro* has not been demonstrated.

In the first part of my thesis, I reconstituted Shieldin complex with REV7, SHLD3 and N-terminal fragment of SHLD2 and found that Shieldin contains a REV7 dimer. Similar to MCC, Shieldin assembly is cooperative with SHLD2 mediating REV7 dimer formation. During the course of this thesis, it was shown that REV7 exists in two different topologies (Clairmont et al., 2020). Also, it was shown with crystallographic studies that Shieldin complex contains O-C REV7 dimer (Liang et al., 2020; Xie et al., 2021). I created topology mutants of REV7 to trap REV7 in either open conformer or closed conformer. Using these mutants, I show that REV7 exists as a C-I dimer in Shieldin complex where conversion of only one REV7 protomer for SHLD3 binding is necessary. To see whether this observation holds true I carried out kinetic measurement of REV7-SHLD3 binding using surface plasmon resonance (SPR). In line with my finding, I observe the Shieldin assembly rate centered around REV7 binding to SHLD3 has a small association rate and is independent of dimer formation. Though the dimer formation is necessary for Shieldin assembly at DSBs it does not affect the kinetics of assembly.

The second and final part of my thesis deals with characterizing and providing a molecular function to SHLD3. Previous studies suggest SHLD3 is recruited at DSBs in a 53BP1-RIF1 dependent manner (Gupta et al., 2018; Noordermeer et al., 2018). However, it is unclear what recruits SHLD3 at DSBs. Since SHLD3 is the first Shieldin protein to localise at DSBs I reasoned that it could bind DNA directly. I determined that SHLD3 is a DNA binding protein in Shieldin complex and this activity is present in its C-terminal domain. By combining the observations from reconstitution experiments, kinetic measurements and

DNA binding experiments, I developed a model for Shieldin recruitment and assembly at DSBs. Our results provide strong evidence to the hypothesis that REV7 conversion from open to closed is the rate limiting step in Shieldin assembly.

2.Materials and Methods

2.1 Materials

The following section lists materials used in this thesis

Table 2.1: DNA probes used in this thesis.

Name	Sequence (5'-3')
FAM Ntelo-6-mer	AGTGCC
Ntelo-6-mer	GGCACT
FAM Telo-6-mer	TTAGGG
Telo-6-mer	CCCTAA
FAM Ntelo-12-mer	AGTGCCAGTGCC
Ntelo-12-mer	AGTGCCAGTGCC
Ntelo-12-mer	GGCACTGGCACT
FAM Telo-12-mer	TTAGGGTTAGGG
Telo-12-mer	CCCTAACCCTAA
FAM Ntel-50-mer	AAGGGGAGCGGGGGAGGATAATAGGAAGGGGAG CGGGGGAGGATAATAGG

All DNA probes were purchased from Sigma-Aldrich.

Table 2.2: Commercial kits used in this thesis.

Name	Company	Catalog number
QIAprep Spin Miniprep Kit	Qiagen	27106
Plasmid Mediprep Kit	Invitrogen	K210015
QIAquick PCR purification Kit	Qiagen	28106

Table 2.3: Miscellaneous materials used in this thesis.

Name	Company	Catalog number
BSA	Sigma-Aldrich	A9418
Coomassie Brilliant blue G-250	Serva	17524.02
Coomassie Brilliant blue R-250	Serva	17525.02
Dithiothreitol (DTT)	Roth	6908.2
Tris(2-carboxyethyl)phosphine hydrochloride (TCEP)	VWR	K831-10G
Phenylmethyl sulphonyl fluoride (PMSF)	Roth	6367.2
Complete protease Inhibitor cocktail	Sigma-Aldrich	S8830
Amylose resin	NEB	E28021L
Trypsin	Hampton Research	HR2-429
α-Chymotrypsin	Hampton Research	HR2-429
MBPTrap-column (5 mL)	Cytiva	28-9187-80
HisTrap-column (5 mL)	Cytiva	17-3712-06
GSTrap-column (5 mL, 1 mL)	Cytiva	28-4017-48
HiTrap Q HP column (1 mL)	Cytiva	29-0513-25
HiTrap S HP column (1 mL)	Cytiva	29-0513-24

HiTrap Heparin HP column (1 mL)	Cytiva	17-0406-01
Immidazole	Sigma-Aldrich	288-32-4
Maltose	VWR	1B1184
Glutathione	Thermo Scientific	78259
Amicon Concentrator (15 ml, 4ml, 0.5ml)	Merck	UFC803024 UFC903024 UFC501024
Ministart syringe filters	Satorius	16592-K
Gibson Master Mix	Homemade	-
Precission protease	Homemade	-
Polycarboxylate hydrogel, medium charge density Sensor chip	Xantec	SCR HC 30M
Regeneration buffer Glycine-HCl	Xantec	B G15-50

Table 2.4: Materials used for culturing *E.coli* and Insect cells in this thesis.

Name	**Company**	**Catalog number**
LB medium	BioChemica	23143289
ESF 921 medium	Expression Systems	96-001-01
Sf-900 medium	Gibco	12658-019
X-tremeGENE Transfection Reagent	Roche	06365787001
IPTG	Roth	2316.5
5-Brom-4-chlor-3-indoxyl-β-D-galactopyranoside (X-Gal)	Roth	2315.3
Ampicillin	Roth	K029.2
Chloramphenicol	Roth	3886.2
Kanamycin	Roth	T832.2
Tetracycline	Roth	HP63.2
Gentamycin	Roth	0233.4

Spectinomycin	Sigma-Aldrich	S9007
LB-agar	Roth	X969.2

Table 2.5: Special equipments used in this thesis.

Name	**Company**
ÄKTA pure	Cytiva
ÄKTA start	Cytiva
ÄKTA micro	Cytiva
VISCOTEK 305 TDA	Malvern Pananlytical
Sonifier SFX-250	Branson
Amersham Imager 680	GE healthcare
Infinite M1000 Microplate reader	Tecan
2SPR Dual Channel system	Xantec
Fluorescence Microscope	Zeiss
Sorvall Evolution Centrifuge	Thermo Scientific

Table 2.6: Softwares used in this thesis.

Name	**Developer**	**Version**
OmiSEC	Malvern Pananlytical	v5.12
TraceDrawer	Xantec	v1.5
JalView	Barton Group (University of Dundee)	v2.11.1.5
PyMol	Schrödinger, LLC	v 2.5.2
AlphaFold 2	DeepMind (Alphabet Inc.)	
Adobe Illustrator	Adobe Inc.	v15.1.0
Graphpad PRISM	GraphPad Software Inc.	v8.3.0
ImageJ	NIH, USA	Java 6

2.2 General methods for DNA cloning and protein expression

2.2.1 Competent cell preparation

Competent cells were prepared by thawing and inoculating 50-100 µL in 2 mL LB medium overnight under shaking condition. The cells were diluted in 50 mL fresh LB medium and cultured until OD_{600} of 0.4 was achieved. The cells were pelleted at 4000 rpm at 4 °C for 10 minutes using TX 400 rotor. The supernatant was discarded and pellet was resuspended in 10 mL ice-cold 0.1M $CaCl_2$. The culture was left on ice for ~ 1 hour followed by centrifugation at 4000 rpm at 4 °C for 10 minutes. The supernatant was discarded and pellet was resuspended in 2 mL ice-cold 0.1M $CaCl_2$. 500 µL of 50% Glycerol was added with a final concentration of 10% Glycerol in the bacterial suspension. Aliquots of 100 µL were prepared and flash frozen using liquid nitrogen and stored at -80 °C.

2.2.2 Gibson Assembly

All cloning reactions were carried out using Gibson assembly (Weissman et al., 2016). To do this, homemade Gibson master mix was prepared. 5x ISO-Buffer consisting of 3 mL 1M Tris-HCl (pH7.5), 300 µL 1M $MgCl_2$, 60 µL of 100 mM dATP, dCTP, dGTP, dTTP each, 300 µL of 1M DTT, 1.5 g PEG-8000, 300 µL of 100 mM NAD and 1.8 mL water was prepared, aliquoted and stored at -20 °C. Gibson master mix was prepared by adding 320 µL of 5xISO-Buffer, 0.64 µL of 10 U/ µL T5 exonuclease (T5E4111K, Epicentre), 20 µL of 2 U/ µL Phusion HF polymerase (M0530, New England Biolabs), 160 µL of 40 U/ µL Taq ligase (M0208, New England Biolabs), and 700 µL of water. Aliquots of 15 µL were prepared and stored at -20 °C. The Gibson assembly reactions were performed in Eppendorf PCR tubes with a total volume of 20 µL. To do this, 5 µL of linearized vector and PCR product in 1:5 molar ratio was added to 15 µL of Gibson master mix. The reaction was incubated at 50 °C for 60 minutes. 2 µL of Gibson reaction mixture was used for

transformation of NEB 5-alpha competent *E.coli*. Vector linearization was carried out using BamHI HF® and HinDIII HF® (New England Biolabs) restriction enzymes. Vector to be linearized (~ 1 µg) was incubated with 2 µL of restriction enzymes at 37 °C overnight in CutSmart® buffer (New England Biolabs). Vector purification was carried out using PCR purification kit (Qiagen) according to manufacturer's protocol. Oligonucleotides used for cloning are listed in the supplement (Tables S4, S5, S6, S7, S8). Purification PCR product was carried out using PCR purification kit (Qiagen) according to manufacturer's protocol. Plasmids used in this study are listed in Table S1 and *E. coli* strains used are listed in Table S2. NEB 5-alpha Competent *E.coli* (New England Biolabs) cells were used for cloning purposes.

Bacterial transformations were carried out by thawing 20 µL of competent cell stock on ice and subsequently adding 2 µL of DNA (approximately 120 - 200 ng in total). The suspension was mixed gently by repeated pipetting. After incubation on ice for 5 mins, the suspension was subjected to heat shock at 42°C for 1 min. The suspension was again incubated on ice for 5 mins prior plating on LB plate with appropriate antibiotics.

For generation of pBIG1 plasmids, gene products from pLIB were amplified using oligonucleotides listed in Table S8. To generate a polycistronic insert containing two genes, oligonucleotides CasI_for and CasI_rev (See Table S8 for sequence) was used as forward and reverse primers to amplify gene 1 from pLIB respectively. Similarly, CasII_for and Casω_rev was used as forward and reverse primers to amplify gene 2 from pLIB respectively. Both PCR products were cleaned up using PCR purification kit (Qiagen) using manufacturer's protocol. pBIG1 vector linearization was carried out similarly as described above using SwaI restriction enzyme (R0604, New England Biolabs) and NEBuffer® 3.1. After digestion, the vector was purified using PCR purification kit (Qiagen) using manufacturer's protocol. The linearized vector and PCR products (gene 1 and gene 2) were mixed in 1:5 molar ratio in 5 µL total volume. The vector-insert mixture was mixed with 15 µL of Gibson master mix and incubated at 50 °C for 60 minutes. 2 µL of Gibson reaction was used to transform NEB5-alpha competent cells as described previously and plated on LB plates containing chloramphenicol.

To generate polycistronic insert containing three genes, a similar protocol was used with gene 2 PCR amplification carried out using CasII_for (forward primer) and CasII_rev (reverse primer) while gene PCR amplification carried out using CasIII_for (forward primer) and Casω_rev (reverse primer). Correct colonies were picked by colony PCR (single PCR for each gene) and subsequently sequenced.

For protein expression, *Rosetta* or LOBSTR strains were used. Transformation was carried out by thawing 50 µL of competent cell stock on ice and subsequently adding 2 µL of DNA (approximately 120 - 200 ng in total). The suspension was mixed gently by repeated pipetting. After incubation on ice for 5 mins, the suspension was subjected to heat shock at 42°C for 1 min. The suspension was again incubated on ice for 5 mins. Immediately the bacterial suspension was inoculated in 50 mL of LB medium with appropriate antibiotics overnight at 37°C prior transferring to a 1 litre culture flask again with appropriate antibiotics. After reaching OD_{600} 0.7-0.8 the cultures were transferred to 16 °C and cultured for another 1 hour. After one hour, 0.1 mM IPTG was added to the culture and further incubated overnight at 16 °C under shaking condition. The cells were harvested (4000 x g, 20 min, 4°C) and resuspended in 25 mL chilled 1x phosphate buffered saline (PBS) pH 7.4 consisting of 137 mM NaCl, 27 mM KCl, 43 mM Na_2HPO_4 and 14 mM NaH_2PO_4. The bacterial culture was centrifuged again at 4000 x g for 20 min at 4°C. After discarding the supernatant, the pellets were either subjected to lysis immediately or stored at -20 °C for further use.

2.2.3 Bacterial and Insect cell culturing

Bacteria were grown in LB medium (Miller L H., 1993) for both cloning and expression purposes. When needed, antibiotics were added with the following final concentrations: 100 µg/mL ampicillin, 50µg/mL kanamycin, 25 µg/mL chloramphenicol, 10 µg/mL tetracycline, 10 µg/mL gentamycin, 50 µg/mL spectinomycin. Both SF9 insect cells and Hi5 insect cells were cultured in Sf-900 medium and ESF 921 medium in the absence of any antibiotics respectively.

For protein expression from insect cells, SF9 culture infected with virus was mixed with 1 litre culture of Hi5 cells at cell density of ~ 1 x 10^6 cells/mL. The culture was incubated further for 48-72 hours while actively monitoring cell viability using Casy cell counter and analyzer (Omni life science). The cells were harvested (500 x g, 30 min, 4°C) at the end of 72 hour period or when the viability dropped below 85 %. Cells were resuspended in 25 mL ice-cold 1x PBS pH 7.4. The culture was centrifuged again at 500 xg, 30 min at 4°C. After discarding the supernatant, the pellets were either subjected to lysis immediately or stored at -20 °C until further use.

2.2.4 Site-Directed Mutagenesis

Oligonucleotides used for site-directed mutagenesis are listed in Table S4, S5. Oligonucleotides containing single point mutation or multiple point mutations were purchased from Sigma-Aldrich. Mutagenesis was carried out using modified protocol from (Liu H. and Naismith J., 2008). Primers (forward or reverse) were designed such that the point mutation/s were placed in the center of the oligonucleotide with long 3' and 5' arms. The complementary primer was designed harbouring no mutations. The primer pairs were used to amplify the complete plasmid (~6 min extension time). The PCR mixture was subjected to Dpn-I digestion (R0176, New England Biolabs) using manufacturer's protocol. After digestion, the vector was purified using QIAquick PCR purification kit using manufacturer's protocol. The purified vector was used to transform NEB 5-alpha competent cells and plated onto LB plate with appropriate antibiotics as described previously. Colonies were picked and sequenced using *E. coli* NightSeq (Microsynth) using manufacturer's protocol.

2.3 Cell culture

2.3.1 Generation of Bacmid

Bacmid generation was carried out by transforming DH10EMBacY (Berger I. et al., 2004) cells with pLIB plasmids containing Shieldin complex or its individual components. Bacterial transformations were carried out by thawing 100 µL of competent cell stock on ice and subsequently adding 2-3 µL of DNA (approximately 0.5 - 1 µg in total). The suspension was mixed gently by repeated pipetting. After incubation on ice for 10 mins, the suspension was subjected to heat shock at 42°C for 1 min. The suspension was again incubated on ice for 10 mins. The culture was then transferred to 0.5 mL LB medium and incubated overnight at 37 °C. 200 µL of transformant was plated on LB plates supplemented with 50 µg/mL kanamycin, 10 µg/mL tetracycline and 10 µg/mL gentamycin with 100 µg/mL X-Gal and 1 mM IPTG for blue-white colony screening. After incubation for 48 hours at 37°C, white colonies were picked and inoculated in fresh 2 mL LB medium supplement with the above-mentioned antibiotics at 37 °C overnight. After pelleting the culture (max speed, table top centrifuge), the supernatant was discarded and the pellet was resuspended in 300 µL resuspension buffer (Mini-prep kit, Qiagen). After brief incubation on ice, 300 µL of lysis buffer (Mini-prep kit, Qiagen) was added with gentle mixing and incubated further for 4 minutes. Finally, 300 µL of neutralizing buffer was added (Mini-prep kit, Qiagen). After gentle mixing, the suspension was centrifuged for 10 minutes (max speed, table top centrifuge). After a similar second centrifugation step, the supernatant was mixed with equal volumes of ice-cold isopropanol and stored overnight at -20 °C. The suspension was then centrifuged again (max speed, table top centrifuge) and supernatant discarded. The pellet was washed with 1 mL of 70% ethyl alcohol and centrifuged again at RT for 5 mins at max speed. The removal of ethanol was carried under sterile conditions in hood and the pellet was air dried for 10-20 mins. The pellet was resuspended in 40 µL of water.

2.3.2 Baculovirus Production (V0 and V1)

Baculovirus production for insect cell expression was carried out using an adapted protocol from Berger I. et al, (2013). Fresh stock of 3 mL cultured SF9 cells (at cell density of 1 x 10^6 cells/mL) was inoculated in sterile 6 well plates. For V0 virus production, transfection mixture was prepared in a tube consisting of 20 µL of bacmid DNA, 5 µL of XtremeGENE transfecting agent (Roche), 400 µL of Sf-900 medium (Gibco). The reaction mixture was incubated for 20 mins in dark for virus particle formation. The transfection mixture was added drop by drop in 6 well plates containing SF9 cells. Thereafter, the plates were incubated for 72-96 hours at 27 °C in dark. After 96 hours, the supernatant (containing virus particles) was added to 10 cm plate culture seeded with log-phase SF9 cell culture (cell density ~ 1 x 10^6 cells/mL) and cultured further for 72 hours at 27 °C in dark. The supernatant was collected and stored at 4 °C in falcon tubes. Another round of amplification was carried out to generate V1 virus particles by inoculating 1-2 mL of V0 virion particle suspension in 25 mL of fresh SF9 cells (cell density 1 x 10^6 cells/mL). The culture was inoculated for 72 hours at 27°C in dark and course of virial infection was monitored qualitatively using YFP reporter fluorescence (fluorescent: infected, nonfluorescent: uninfected) and measuring increase in diameter from 16 microns (healthy, uninfected) to ~20-22 microns (infected). The supernatant was collected and stored at 4 °C in falcon tubes. Prior infection of Hi5 insect cells for large scale protein production, V1 virus was subjected for test expressions in 25 mL Hi5 cells. After infection of Hi5 cells for 72 hours, the cells were harvested and resuspended in 2 mL lysis buffer containing 10 µM PMSF. The cells were lysed with sonicator at 4°C once for 10 sec with 10% power. A sample of 10 µL was aliquoted and mixed with 4x SDS gel loading buffer. The remaining sample was centrifuged at max speed for 10 minutes at 4°C. After clearing, the lysate was mixed with Amylose resin (New England Biolab) or pierce glutathione agarose (Thermo Scientific) prewashed with lysis buffer. After 10 minutes incubation, the beads were centrifuged at 500 x g, 4°C for 5 mins. Excess buffer was discarded and the beads were washed three times with 1 mL of ice-cold lysis buffer. After final wash, the supernatant was carefully removed and the bead-protein conjugate was mixed with 4x SDS gel loading

buffer. The post-sonication lysate sample and bead-protein conjugate sample were analysed using SDS-PAGE.

2.4 Reconstitution of Shieldin complex

This section contains part of already published data (Krijger et al, 2021) and has been written by Vivek Susvirkar.

2.4.1 Strains and cell lines used for protein expression

For protein expression in *E. coli*, LOBSTR competent cells were used. Where indicated, *Rosetta* competent cells were used instead.

2.4.2 Expression of Shieldin complex in insect cells

REV7 constructs were cloned into plasmid pLIB-MBP containing T7 promoter (Weissmann et al., 2016), with a N-terminal Maltose binding protein (MBP) fusion tag followed by a PreScission site (3C) protease cleavage site. Since wild type REV7 undergoes homo dimerization, arginine at 124 position was mutated to alanine (R124A) to get monomeric REV7 (Hara et al., 2007). Similarly, mutation of alanine 135 to aspartic acid (A135D) and lysine 44 to alanine (K44A) identified to form the dimerization interface along with the previously identified R124 generates a more penetrant mutant (Rizzo A. et al, 2018). The resultant $REV7^{R124A}$ (single mutant) and $REV7^{K44A,R124A,A135D}$ (triple mutant) were similarly cloned into plasmid pLIB-MBP. Sequence encoding for SHLD3 was cloned into plasmid pLIB. SHLD2 N-terminal fragment (residues1-95) was cloned into pLIB-GST. The pLIB constructs were amplified and cloned into pBIG1 vector with MBP tag on REV7 constructs and GST tag on SHLD2 constructs. Bacmid generated from pBIG1 construct was used to infect Hi5 insect cells. Post-infection, Hi5 cells were harvested (500 x g, 30 minutes, 4°C) and resuspended in lysis buffer consisting of 25 mM

HEPES-NaOH pH 7.5, 300 mM NaCl, 5 % glycerol and 0.5 mM TCEP. After addition of 10 µM PMSF and protease inhibitor cocktail (1 pill crushed and dissolved in 10 mL of lysis buffer separately), the cells were lysed by sonicator at 4°C with 20% power with pulses for 5 sec with the microtip with 10 sec pause between pulses for a total of 3 minutes. The lysed cells were subjected to centrifugation for 30 minutes at 500 x g at 4°C. After clearing, the lysates were filtered through a 0.8 micron filter tip and loaded onto an MBP-trap column (Cytiva) pre-equilibrated with lysis buffer. After washing the bound proteins with lysis buffer for 20 CV. Bound protein complex was eluted using lysis buffer supplemented with 5 mM maltose in a step gradient. Shieldin complex was further purified by anion exchange chromatography. Complex was resuspended in buffer A2 (20mM HEPES-NaOH pH 7.5, 0.5 mM TCEP) to reduce NaCl concentration from 300 mM to 50 mM. The resultant protein solution was loaded onto a 6 mL Resource S Column (Cytiva) equilibrated in 20 mM HEPES-NaOH pH 7.5, 50 mM NaCl, 0.5 mM TCEP. The proteins were eluted in a salt gradient to 1 M NaCl. Fractions containing purified protein complex were pooled and loaded onto Superdex 200 HiLoad 16/60 column (Cytiva) equilibrated with 10 mM HEPES-NaOH pH 7.5, 150 mM NaCl, 0.5 mM TCEP.

2.4.3 Expression of Shieldin complex components in *E.coli* cells

REV7 constructs were cloned into plasmid pColi-HisMBP containing T7 promoter (Weissmann et al., 2016), with a N-terminal 6x His-Maltose binding protein (MBP) fusion tag followed by a PreScission (3C) protease cleavage site. SHLD3 N-terminal constructs was cloned into plasmid pColi-GST or pColi HisMBP. SHLD3 C-terminal constructs were cloned into plasmid pRSF containing N-terminal 6xHis tag followed by a PreScission (3C) protease cleavage site. SHLD2 N-terminal fragment (residues1-60) was cloned into pColi-HisMBP. For purification of REV7 constructs, an overnight bacterial culture was diluted in LB medium and grown at 37 °C for 5-6 hours. At an OD_{600} of 0.7, cells were moved to 16 °C and expression induced with 0.1 mM IPTG. After overnight induction, the bacterial cells were harvested (4000 x g, 20 minutes, 4 °C) and resuspended in lysis buffer consisting of 25 mM HEPES-NaOH pH 7.5, 300 mM NaCl, 5 % glycerol and 0.5 mM TCEP. After

addition of 1 mL of PMSF (final concentration 10 µM), the cells were lysed by sonicator at 4 °C with 30% power with pulses for 5 sec with the microtip with 10 sec pause between pulses for a total of 3 minutes. The lysed cells were subjected to centrifugation for 30 minutes at 4000 x g at 4 °C. After clearing, the lysates were loaded onto an MBP-trap column (Cytiva) pre-equilibrated with lysis buffer. After washing the bound proteins with lysis buffer for 20 CV, elution was carried out using lysis buffer supplemented with 5 mM maltose in a step gradient. After overnight incubation with PreScission protease, REV7 constructs were further purified by reverse affinity. Fractions containing purified REV7 were pooled and loaded onto Superdex 200 HiLoad 16/60 column (Cytiva) equilibrated with 10 mM HEPES-NaOH pH 7.5, 150 mM NaCl, 0.5 mM TCEP. Fractions containing REV7 were pooled and flash frozen in liquid nitrogen and stored at -80 °C until use.

To purify HisMBP-REV7 and HisMBP-SHLD2$^{1-60}$ constructs, a similar purification protocol as mentioned above was used leaving out overnight incubation with PreScission protease.

To purify HisMBP-REV3$^{1871-2014}$, a similar purification protocol as mentioned above was used leaving out overnight incubation with PreScission protease. However, to purify REV3$^{1871-2014}$ for SPR analysis incubation with PreScission protease was carried out followed by MBP tag removal by reverse-affinity. The protein sample was subjected directly to size exclusion chromatography Superdex 200 10/30 column (Cytiva) equilibrated with 10 mM HEPES-NaOH pH 7.5, 150 mM NaCl, 0.5 mM TCEP. Fractions containing REV3$^{1871-2014}$ were pooled and flash frozen in liquid nitrogen and stored at -80 °C until further use.

To purify HisMBP-SHLD3 N-terminal constructs, a similar purification protocol as mentioned above was used leaving out overnight incubation with PreScission protease. However, to purify SHLD3$^{1-62}$ for SPR analysis incubation with PreScission protease was carried out. The protein sample was subjected directly to size exclusion chromatography Superdex 200 HiLoad 16/60 column (Cytiva) equilibrated with 10 mM HEPES-NaOH pH 7.5, 150 mM NaCl, 0.5 mM TCEP. Fractions containing SHLD3$^{1-62}$ were pooled and flash frozen in liquid nitrogen and stored at -80 °C until further use.

To purify His-SHLD3 C-terminal constructs, protein was eluted from 5 mL His-Trap Excel column (Cytiva) using washing buffer containing 500 mM Imidazole. After overnight incubation with PreScission protease, further purification was carried out on Superdex 200 10/30 column (Cytiva) equilibrated with 10 mM HEPES-NaOH pH 7.5, 150 mM NaCl, 0.5 mM TCEP. Fractions containing SHLD3-CTD were pooled and flash frozen in liquid nitrogen and stored at -80 °C until further use.

To purify HisMBP-SHLD3 C-terminal constructs, a similar purification protocol as mentioned above was used. An additional purification was incorporated. After tag cleavage with PreScisson protease, protein sample diluted to 20 mM using buffer A2 and was loaded onto a HiTrap S HP column (Cytiva). Bound proteins were eluted using a salt gradient of 0-500 mM NaCl. SHLD3-CTD was subjected to size exclusion chromatography using Superdex 200 10/30 column (Cytiva) equilibrated with 10 mM HEPES-NaOH pH 7.5, 150 mM NaCl, 0.5 mM TCEP. Fractions containing SHLD3-CTD were pooled and flash frozen in liquid nitrogen and stored at -80 °C until further use.

To purify Shieldin complex, 5 mL bacterial pellets containing HisMBP-REV7^{R124A} or GST-SHLD3$^{1-83}$ or MBP-SHLD2$^{1-60}$ were co-lysed in lysis buffer. After addition of 1 mL of PMSF (final concentration 10 µM), the cells were lysed by sonicator at 4 °C with 30% power with pulses for 5 sec with the microtip with 10 sec pause between pulses for a total of 3 minutes. The lysed cells were subjected to centrifugation for 30 minutes at 4000 x g at 4 °C. After clearing, the lysates were loaded onto a GST-trap column (Cytiva) pre-equilibrated with lysis buffer. After washing the bound proteins with lysis buffer for 20 CV, elution was carried out using lysis buffer supplemented with 10 mM Glutathione in a step gradient. After overnight incubation with PreScission protease, REV7 constructs were further purified by reverse affinity using MBP-Trap column. Fractions containing purified REV7 were pooled and loaded onto Superdex 200 HiLoad 16/60 column (Cytiva) attached to 1 mL GSTrap affinity column (Cytiva) equilibrated with 10 mM HEPES-NaOH pH 7.5, 150 mM NaCl, 0.5 mM TCEP. Fractions containing Shieldin complex were pooled and flash frozen in liquid nitrogen and stored at -80 °C until further use.

2.5 Biochemical Assays

2.5.1 *In-vitro* pulldowns

For pulldown experiments via MBP tag of SHLD3$^{45-60}$, 10 µL of bait (MBP-SHLD3$^{45-60}$) was incubated with 50 µL of Amylose Resin (New England Biolabs) pre washed with buffer C. After incubation for 10 mins on ice, the suspension was briefly centrifuged for 1min. The excess buffer was discarded and the beads-protein mixture was washed once with 500 µL of buffer C. Prey protein (REV7 constructs) were added at four-fold excess and incubated for 30 mins. After washing twice with 500 µL of buffer D (10mM HEPES-NaOH pH 7.5, 500 mM NaCl ,0.5 mM TCEP), the excess buffer was removed. After brief centrifugation at max speed (15,000 rpm), 4x SDS gel loading dye was added to the samples and were analysed by SDS-PAGE.

2.5.2 Measurement of SHLD3-REV7 kinetics using *in-vitro* pulldown assay

The pulldown assay performed in this thesis is a modified protocol adapted from Simonetta et al., (2009). For kinetic pulldown experiments via MBP tag of SHLD3$^{28-83}$, 10 µL of bait (MBP-SHLD3$^{28-83}$) was incubated with 50 µL of Amylose Resin (New England Biolabs) pre washed with buffer C. After incubation for 10 mins on ice, the suspension was briefly centrifuged for 1min. The excess buffer was discarded and the beads-protein mixture was washed once with 500 µL of buffer C. Prey protein (REV7 constructs) were resuspended in 200 µL of buffer C. The protein solution was added to the bead solution and incubated for specific time points. At the end of specific time points, the sample was washed twice with 500 µL of buffer C. Excess buffer was discarded and after a brief spin at max speed, 4x SDS gel loading dye was added. Samples were analysed by SDS-PAGE.

2.5.3 Analysis of kinetic reactions

To analyse the kinetic profile, the intensity of each unique separated band was quantified using ImageJ. For each time point, the bait band intensity (B.I) was compared with prey band intensity on the same lane (at 0-hour MBP-SHLD3$^{28\text{-}83}$ vs REV7) to account for different loading efficiencies of bait protein on SDS gel (Figure 2x). The band intensities were normalized with molecular weight of proteins and used to calculate percentage maximal binding rate assuming 1:1 binding stoichiometry (Dai et al, 2019).

$$\%\, maximal\ binding = \frac{B.I^{normalized\ Prey}}{B.I^{normalized\ Bait}}\ X\ 100$$

2.5.4 Anion Exchange Chromatography

To carry out anion exchange chromatography, 500 µL protein sample (1mg/mL) were resuspended in buffer A2 (20mM HEPES-NaOH pH 7.5, 0.5 mM TCEP) to reduce NaCl concentration from 150 mM to 20 mM. The protein solution was then loaded onto HiTrap Q anion exchange column (Cytiva) equilibrated in 20 mM HEPES-NaOH pH 7.5, 20 mM NaCl, 0.5 mM TCEP. The proteins were eluted in a salt gradient to 500 mM NaCl. Eluted fractions where mixed with 4x gel loading buffer and loaded on 12% SDS gels. For Shieldin complex formation, insect cells infected with either MBP-REV7^{R124A}-SHLD3 or GST-SHLD2$^{1\text{-}95}$ were co-lysed in lysis buffer and affinity purified. The purified fractions were resuspended in buffer A2 (20mM HEPES-NaOH pH 7.5, 0.5 mM TCEP) to reduce NaCl concentration from 150 mM to 50 mM. The resultant protein solution was loaded onto a 6 mL Resource Q Column (Cytiva) equilibrated in 20 mM HEPES-NaOH pH 7.5, 50 mM NaCl, 0.5 mM TCEP. The proteins were eluted in a salt gradient to 1 M NaCl. Eluted fractions where mixed with 4x gel loading buffer and loaded onto 12% SDS gels.

2.5.5 Size exclusion chromatography

To test for complex formation, proteins were incubated in buffer C on ice for 1 hour. After incubation the protein samples were loaded onto either Superdex 75 10/300 column (Cytiva) or Superdex 200 10/300 column (Cytiva) equilibrated in buffer C. Protein samples were collected as 0.5 mL aliquots. Eluted samples were mixed with 4x SDS gel loading buffer and analysed using SDS-PAGE. To test for complex formation on Superdex 200 increase 3.2/300, proteins were incubated in buffer C on ice for 1 hour and loaded onto column equilibrated in buffer C. Protein samples were collected as 50 µL aliquots. Eluted samples were mixed with 4x SDS gel loading buffer and analysed using SDS-PAGE.

2.5.6 Fluorescence Polarization Assay

DNA probes used for fluorescence polarization assay are listed in Table 2.1. 5,6-FAM (5,6-Carboxyfluorescein) labelled DNA probes were purchased from Sigma-Aldrich. The DNA probes (100 µM initial stock) were diluted to 5 nM stock using buffer FP consisting of 20 mM HEPES-NaOH pH 7.5, 100 mM NaCl, 5% glycerol, 0.5 mM TCEP. 5 µL of 5 nM labelled DNA probe (final concentration 1 nM) was mixed with 5 µL of buffer FP containing 0.25 mg/mL BSA, 15 µL of protein solution (final concentration 40 µM) (Shieldin complex or SHLD3-CTD) and incubated for 30 min at RT in dark. The 18 µL of sample was transferred to a Greiner flat bottom plate and fluorescence measurements were carried out using Infinite M1000 Microplate reader (Tecan). For K_D determination, protein stock was serially diluted 2-fold prior adding to the DNA probe. The experiment and fluorescence measurements were performed as described above. For competition assay, 5 µL of 5 nM labelled DNA probe (final concentration 1 nM) was mixed with 5 µL 0.5 µM unlabelled DNA probe (final concentration 100 nM), 15 µL of protein solution (final concentration 40 µM) (SHLD3-CTD) and incubated for 30 min at RT in dark. The experiment and fluorescence measurements were performed as described above. Fluorescence Anisotropy (FA) was calculated as follows:

$$Fluorescence\ Anisotropy\ = \frac{I^{parallel} - I^{perpendicular}}{I^{parallel} + 2.I^{perpendicular}}$$

2.5.7 Surface Plasmon Resonance

All surface plasmon resonance (SPR) experiments were performed on 2SPR Dual Channel system (Xantec). The SPR experiments were carried out in SPR running buffer consisting of 10 mM HEPES-NaOH pH 7.5, 0.05% Tween detergent, 2.5 % glycerol, 150 mM NaCl, 0.5 mM TCEP. Prior run, the buffer was degassed and filtered. Protein ligands ($SHLD3^{1-62}$/$REV3^{1871-2014}$) were covalently cross-linked to SCR HC30M sensor chip using EDC-NHS coupling reaction. To do this, 20 mg of EDC salt was dissolved in 500 µL of activation buffer (Xantec) to prepare fresh activation buffer (critical step, must be always fresh). Prior carrying out test runs, ligand immobilization was optimized by first immobilizing different ligand concentrations and then testing obtained B_{max} against various analyte (REV7) concentrations. Concentrations of ligand giving optimal B_{max} was selected and used for quantitative estimation (50-100 µg/mL for $SHLD3^{1-62}$, 100 µg/mL for $REV3^{1871-2014}$). Immobilization of SHLD3/REV7 was carried out under a steady flowrate of 25 µL/min by activating the sensor surface with freshly prepared activation buffer for 8 minutes followed by protein peptide solution for 8 minutes. After flowing water over immobilized peptide for 8 minutes, quenching solution (Xantec) was flown over the sensor surface for 4 minutes. For baseline stabilization, SPR running buffer was flown over the sensor chip containing immobilized peptide overnight. Kinetic measurements were carried out using different concentrations of analyte (REV7 mutants). Blank runs consisting of SPR running buffer were carried out after every three runs of analyte.

2.5.8 Analysis of SPR data

SPR curves were exported to TraceDrawer software (Xantec). The left channel was subtracted from the right channel using ‘set the reference channel’ function. The curves

were cut to make them equally long using the 'curve X axis extents' function. Regular spikes arising from pump refilling were removed using 'cut spikes' function. The curves were normalized by subtracting blank curve. The curves were then subjected to affinity evaluation using Affinity/EC50 function. Analyte concentrations were retrieved from sample set and curve intervals were set in the dissociation phase. The values were plotted as signal vs concentration and K_D value was determined. For a detailed protocol, please refer to TraceDrawer 1.5 handbook (https://www.xantec.com). The curves were subjected to kinetic measurement using Graphpad Prism. Prior K_{ON} measurement the curves were modified to remove the dissociation curves. The resultant association curves were subjected to one site - specific binding equation for curve fitting. The rate constant K obtained from curve fitting was plotted against analyte concentration. The K_{ON} was determined from the slope of the straight line represented by the equation:

$$Y = Y_{max}.(1 - e^{-k.X})$$

2.5.9 Limited proteolysis

To check for unstructured regions, present in proteins, proteins were subjected to proteolytic digestion experiment. Protease working stocks (10µg/mL) were prepared and aliquoted from the parent stock (10mg/mL) using manufacturers protocol (Hampton Research). Proteins were mixed with proteases in 10 mM HEPES-NaOH pH 7.5, 150 mM NaCl, 5% Glycerol, and 0.5mM TCEP in a molar ratio of 100:1 respectively. Incubation was carried out at multiple time points (5, 15, 30, 60 min) at 25°C. The reaction was quenched by adding 4x SDS gel loading dye. The samples were analysed by SDS-PAGE.

3.Results

3.1 Reconstitution of Shieldin complex reveals unusual stoichiometry.

To understand molecular mechanism behind Shieldin function, I sought to establish a reconstituted system that would faithfully recapitulate Shieldin assembly and recruitment at DNA breaks. To do this, I purified human Shieldin complex subunits from insect cells. I used REV7^{R124A} mutant which is shown to me more stable and exists as monodisperse particles in solution (Hara et al., 2007). Virus containing MBP-REV7^{R124A}, SHLD3 and GST-SHLD2$^{1-95}$ were added to Hi5 culture and grown for 72 hours at 27°C in dark. Cleared lysate was subjected to affinity purification using HisTrap column and eluted with imidazole gradient. Fractions containing Shieldin complex subunits were pooled and subjected to anion exchange chromatography using Resource-Q column. Elution using 5-100 % NaCl gradient showed separation of two different protein species (Figure 3.1A upper panel). The first peak (Q1) contained a complex of MBP-REV7^{R124A} and SHLD3 while the second peak (Q2) contained a complex of MBP-REV7^{R124A}, SHLD3 and SHLD2$^{1-95}$ (Figure 3.1A lower panel). For simplicity, in this thesis the complex consisting of Shieldin subunits REV7$^{R124A/WT}$, SHLD3 and SHLD2$^{1-95}$ will be termed as Shieldin complex. Quantification of band intensities showed the two complexes contained similar amounts of SHLD3 however double the amount of REV7 in complex containing SHLD2. This data revealed an unusual stoichiometry suggesting presence of REV7 dimer in Shieldin complex (Figure 3.1B). To validate my results, I cleaved the fusion tags and purified the complex further using size exclusion chromatography (SEC). I measured absolute molar mass of Shieldin complex using SEC coupled to static light scattering (SEC-SLS) and estimated the molecular weight to be 87 ± 2.54 kDa. This estimated

molecular weight is only equal to theoretical molecular weight of a Shieldin complex that contains one copy each of SHLD3, SHLD2 and two copies of REV7. Together, these results show that Shieldin complex contains a REV7 dimer.

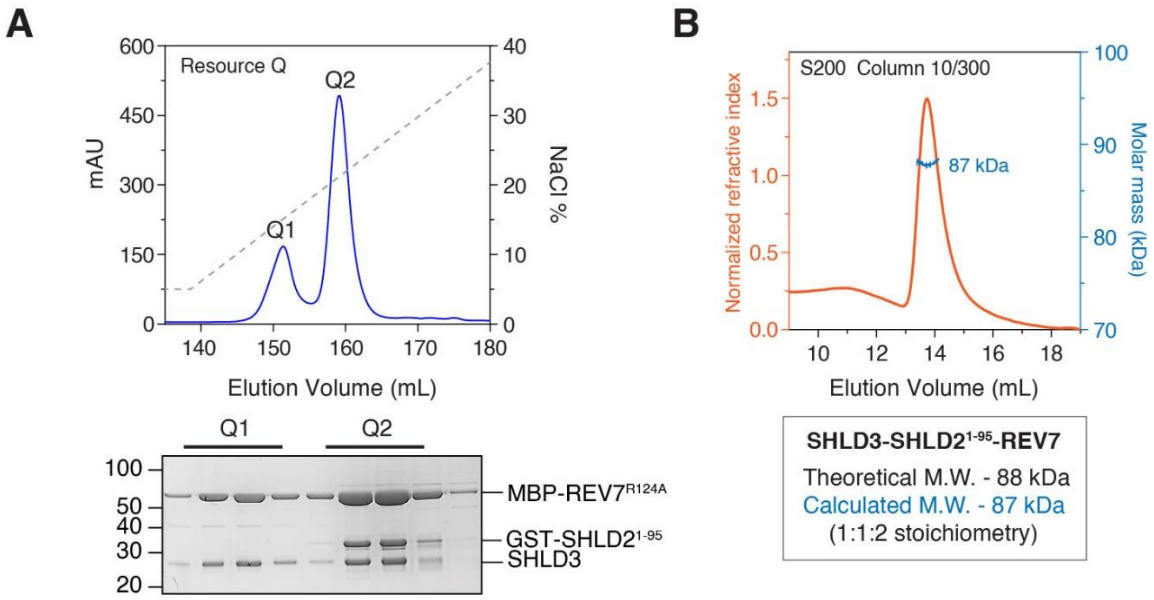

Figure 3.1: The Shieldin complex contains REV7 dimer. **(A)** Q-column purification yields two peaks corresponding to two complexes containing REV7 in different stoichiometric amounts. The peak eluted at lower salt concentration corresponds to SHLD3-REV7^{R124A} (Q1) while the peak eluted at higher salt concentration corresponds to SHLD2$^{1-95}$-SHLD3-REV7^{R124A} (Q2). Fractions (0.5 mL) corresponding to different peaks were analyzed using SDS-PAGE and Coomassie staining (the lower panel). **(B)** Absolute molar mass determination of Shieldin complex using Superdex 200 increase 10/300 column coupled to static light scattering device (SEC-SLS).

3.2 Role of SHLD2 in Shieldin assembly

To investigate whether SHLD2 brings about dimerization of REV7, I carried out SEC experiments with co-expressed Shieldin complex subunits in insect cells. Shieldin complex

containing SHLD2 eluted as a dimer of REV7:REV7-SHLD3. Shieldin complex lacking SHLD2 eluted as a monomeric REV7-SHLD3. This was observed for both $REV7^{WT}$ and $REV7^{R124A}$ (dimer defective mutant). This result confirmed that the dimerization of REV7 is SHLD2 dependent (Figure 3.2A and B).

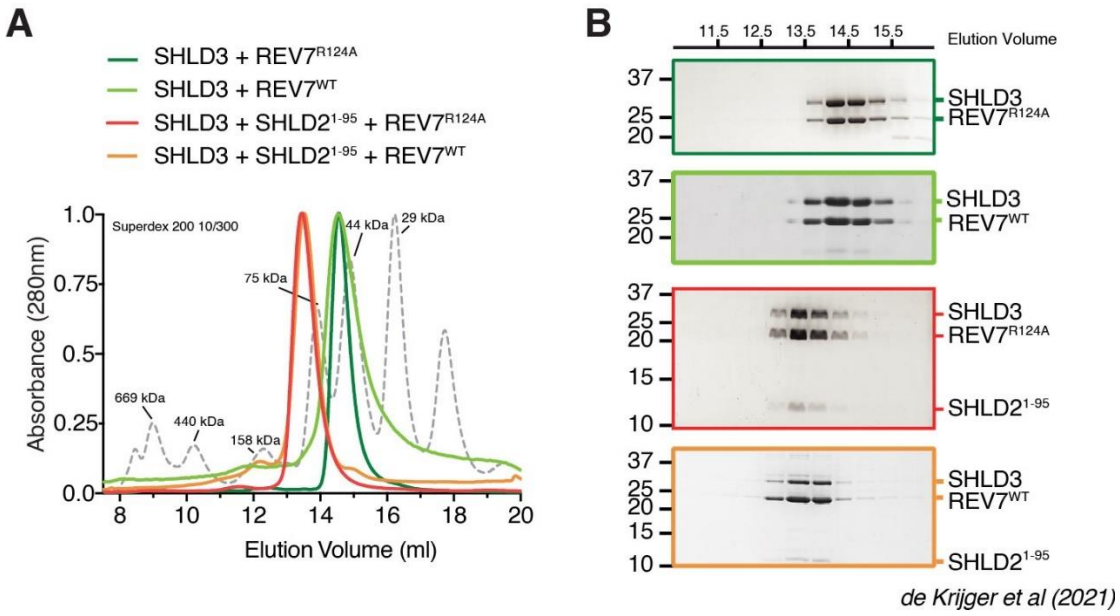

Figure 3.2: REV7 dimerization in the Shieldin complex is mediated by SHLD2 N-terminal region. (A) $SHLD2^{1-95}$ induces dimerization of REV7 in the Shieldin complex. SEC-profiles of SHLD3-REV7 complex (WT: light green, R124A: dark green) and SHLD3-$SHLD2^{1-95}$-REV7 complex (WT: red, R124A: orange). Shift in elution-profile indicates an apparent increase of molecular weight of ~54 to ~90 kDa upon addition of $SHLD2^{1-95}$. Molecular weight of REV7 is 24.5 kDa, of SHLD3 is 29 kDa and of $SHLD2^{1-95}$ is 11 kDa. **(B)** Coomassie-stained SDS-PAGE gels of the experiment shown in (A)

3.3 Characterization of C-REV7 and O-REV7 conformers

Pol-ζ contains two RBMs which are captured by two REV7 protomers in closed state. Our data shows that Shieldin complex contains a REV7 dimer. Therefore, it is possible that REV7 contains either a C-REV7:O-REV7 dimer or C-REV7:C-REV7 dimer. It was shown that SHLD3 contains a single RBM for REV7 binding (Dai et al., 2019). We posited that REV7 is present as a O-C dimer in Shieldin complex due to the presence of only a single RBM on SHLD3. This would mean that for Shieldin assembly conversion of a single protomer of REV7 from open to closed would be rate limiting.

To test this model, it was imperative to first investigate whether REV7 can exists in two topologies. It was shown REV7 can exist in two topologically distinct states like MAD2 (Clairmont et al., 2020). Moreover, these two topology distinct states elute as two separate peaks on anion exchange-column (Q-column). MAD2 can spontaneously convert from closed to open state. A similar conversion is reported for REV7 (Clairmont et al., 2020). To properly address the dimer identity in Shieldin, it became necessary to trap REV7 in either open or closed state. For this, I used known MAD2 mutants to design equivalent mutants in REV7. Briefly, full-length MAD2 adopts either open or close conformation. Deletion of first 15 residues of N-terminus shifts the equilibrium to closed conformation (ΔN15). This is likely due to N-terminus (1-15) forms β1 strand and interacts with β5 strand of the core thereby, stabilizing the open conformation. Deletion of β1 strand destabilizes the open conformation and allows for β8'' strand interaction β5 with leading to adoption of closed conformer. (Figure 3.3A). Similarly, deletion of last 10 residues (β8'' strand) of C-terminus (ΔC) destabilizes the closed conformer thereby, allowing for N-terminal β1- β5 interaction. This shifts the equilibrium to open conformation. Deletion of residues in loop region 105 – 113 and replacing them with glycine-serine triplicate (shortening the loop) locks β1 strand (N-terminus) next to β5 strand. This mutant is trapped in open conformation (LL short for "loop-less"). Further deletion of first 15 residues of N-terminus (β1) in the LL mutant reverts the mutant to close conformation (ΔN, LL) (see

Figure 3.3 A). To make sure that the separation is achieved purely on the basis of different topology and not REV7 dimerization, these mutants were generated with addition of R124A to them to eliminate any possibility of contamination with REV7 homodimer. All REV7 mutants were tested for the topology they adopt on a Q-column. I noticed several differences as compared to published data by Clairmont et al (2020). Their study identifies $REV7^{R124A}$ species to elute at 100 mM NaCl concentration to be C-REV7 whereas $REV7^{R124A}$ species to elute at 300 mM to be O-REV7. Moreover, they report Open REV7 to be thermodynamically more stable as compared to closed REV7. In contrast, I observe $REV7^{R124A}$ to adopt closed conformation elute from my REV7 purifications (Figure 3.3B). This suggests that closed REV7 is thermodynamically more stable as compared to open. Also, I could only observe open conformer of REV7 with the LL mutation. In MAD2, LL mutation was devised to trap and stabilize open conformer on close MAD2 conformer (Mapelli et al., 2007). This suggests REV7 can adopt open conformation however, readily switches to closed conformation. In O-MAD2, N-terminus forms β1 strand interaction with β5 strand of the core and occupies the same position as that of β8' in C-MAD2. Thus, on deletion of the N-terminus (ΔN15) MAD2 is seen adopting closed conformation (Figure 3.3A). To test whether this is also the case of REV7. I deleted the N terminus of REV7 leads to it adopting close conformation. Similarly, deletion of N terminus of LL-REV7 leads to it adopting close conformation (Figure 3.3C). This confirms REV7 follows MAD2-like conversion between open and closed state. Secondly, $REV7^{\Delta C}$ mutant which in MAD2 adopts open conformation is reported to elute as an open conformer (Clairmont et al., 2020) whereas, I observe it elutes as close conformer (Figure 3.3C). This difference can be explained if closed REV7 is the thermodynamically preferred conformation. ΔC mutant is unable to lock REV7 in stable open conformation as efficiently as the LL mutant. Table 3 summarise the Q-column experiments.

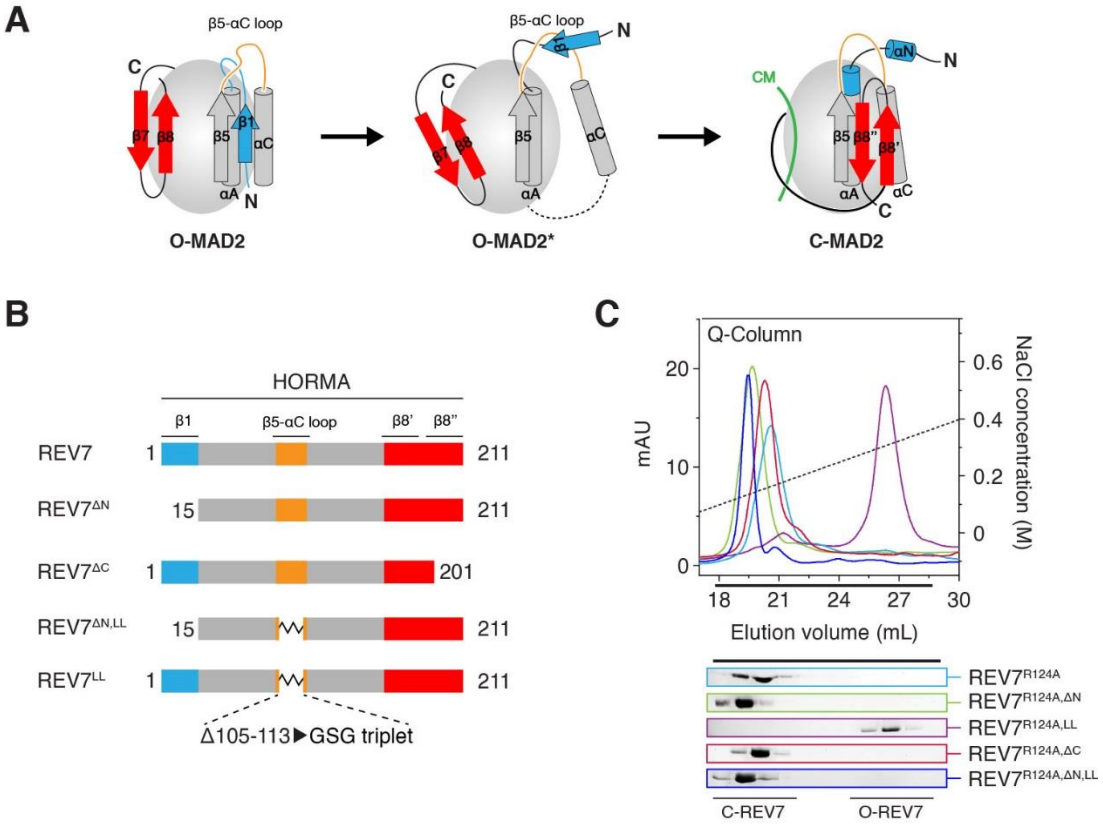

Figure 3.3: Anion-Exchange chromatography to separate REV7 topology mutants. (A) Cartoon representation of the MAD2 closure showing secondary structure elements involved in conversion (adapted from Mapelli et al., 2007). In the open state N-terminal and C-terminal regions coloured as blue and red respectively. Conversion requires the N-terminal region (β1 strand) to be relocated by passing through the β5-αC loop to allow capture of CM by C-terminal region. (CM- closure motif) **(B)** Schematic representation of various mutant designs used to trap REV7 in either open or closed topology. **(C)** Anion-exchange chromatographic analysis of $REV7^{R124A}$ topology mutants. In agreement with the previous study (Clairmont et al., 2020). $REV7^{R124A}$ exists in open and close conformation that is identified based on the salt concentration (dotted line) at which these species elute from an anion exchange column. $REV7^{R124A}$ species in the O-REV7 conformation elute at higher NaCl concentrations (320 mM) relative to the C-REV7 conformation (150 mM). $REV7^{R124A}$, $REV7^{R124A/\Delta C}$ $REV7^{R124A/\Delta N}$ $REV7^{R124A,\Delta N,LL}$ eluted as C-REV7. $REV7^{R124A,LL}$ eluted as O-REV7. Eluted fractions were collected and analyzed by SDS-PAGE.

Since only the closed conformer of MAD2 binds CDC20 in the safety-belt interaction, I asked whether REV7 shows a similar binding preference. To test this, I carried out pulldown experiments. MBP tagged SHLD3 containing the RBM (residues 45 – 65) was immobilized on amylose beads. After adding WT REV7 topology mutants, the reaction was incubated for 30 minutes at 4°C. In the given time frame, only the WT and ΔN mutants were able to bind SHLD3. LL and ΔC mutants failed to bind SHLD3 (Figure 3.4A). A similar result was obtained for R124A mutants suggesting dimerization plays no role in influencing REV7 binding to SHLD3. This result shows only close REV7 is able to bind SHLD3 since WT and ΔN mutant are in closed conformation while LL is in open conformation (Figure 3.4B). In this setup, ΔC mutant of REV7 in unable to bind SHLD3 as the C-terminal (β8') seems to be necessary for stable closure of HORMA fold on SHLD3. This is in agreement with the published data (Clairmont et al., 2020).

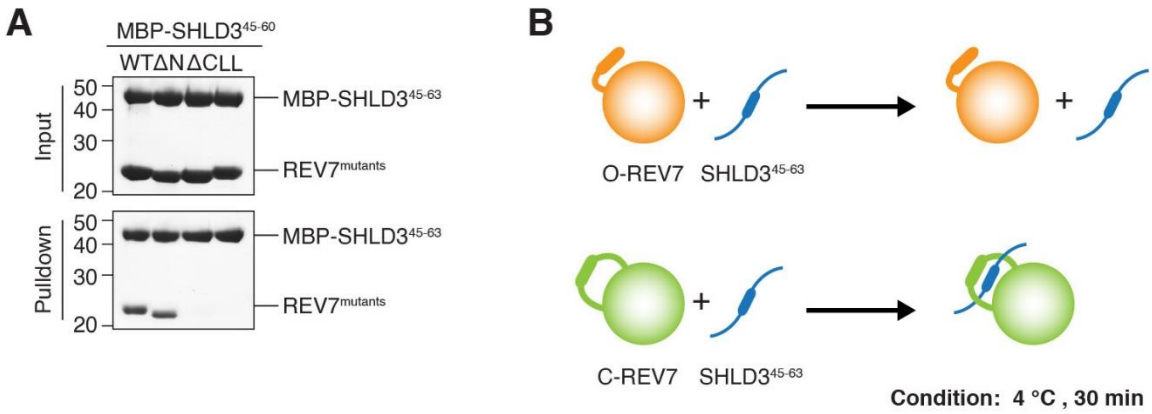

Figure 3.4: SHLD3 binding preferences of REV7 topology mutants. (A) MBP-SHLD3$^{45-63}$ on Amylose beads was incubated with REV7 species labelled in black on the upper part of the panel. After 30 min incubation, the excess REV7 was washed out. After two washing steps, Coomassie staining and SDS-PAGE were used to visualize bound species. **(B)** Cartoon representation of the experiment carried out in (A). Only closed topology mutant of HORMA REV7 binds SHLD3 in canonical safety-belt interaction.

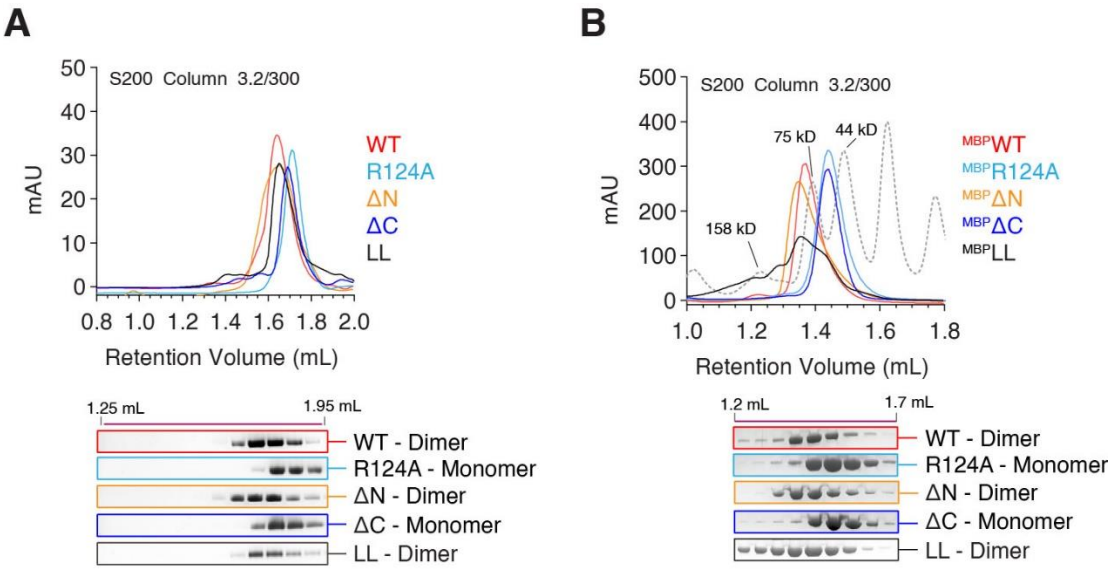

Figure 3.5: Dimerization profiles of REV7 mutants. (A) SEC profiles of $REV7^{WT}$, $REV7^{R124A}$, $REV7^{\Delta N/WT}$, $REV7^{\Delta C/WT}$, and $REV7^{LL/WT}$ on Superdex-200 3.2/300 column equilibrated in buffer B **(B)** SEC profiles of MBP- $REV7^{WT}$, MBP-$REV7^{R124A}$, MBP-$REV7^{\Delta N/WT}$, MBP-$REV7^{\Delta C/WT}$, and MBP-$REV7^{LL/WT}$ on Superdex-200 3.2/300 column equilibrated in buffer B.

I next tested whether closed REV7 or open REV7 could possibly dimerize. Full-length REV7 similar to full-length MAD2 can readily homodimerize as reported by Rizzo et al (2018). This homo dimerization utilizes the dimerization interface of REV7 and mutation of the dimerization interface residues abolishes dimer formation (Rizzo et al., 2018, Hara et al., 2010). I used WT REV7 topology mutants and carried out SEC experiments to investigate this. Like MAD2, REV7 eluted from SEC column at 16-17 mL corresponding with an apparent molecular weight of 48 kDa whereas $REV7^{R124A}$ eluted at 16.5-18 mL as a monomer (Figure 3.5A, see lower panel). MAD2 can only form C-MAD2:C-MAD2 or O-MAD2:C-MAD2 homodimer (Mapelli et al., 2007; Yang et al., 2007). Surprisingly, both ΔN (closed REV7) and LL (Open REV7) eluted at 16-17 mL suggesting either topology of REV7 can exist as a homodimer in solution as long as the dimer interface is unperturbed. On the other hand, ΔC eluted at 16.5-18 mL suggesting it is present in the

monomeric state. The above experiment was performed again with MBP fusion tag attached to N-terminus of REV7 mutants and yielded a similar result (Figure 3.5B). Taken together, these result show REV7 can be trapped in two topologically distinct states with only the closed state of REV7 able to bind SHLD3. REV7 homodimerization seems to be independent of topology similar to MAD2 where O-C homodimer as well as C-C homodimer is possible (Mapelli et al., 2007; Yang et al., 2007).

Table 3: Comparison of topology mutants between HORMA domain proteins MAD2 and REV7.

MAD2			**REV7**		
Mutants (published)	**HORMA Topology**	**Dimerization**	**Mutants (This study)**	**HORMA Topology**	**Dimerization**
$MAD2^{WT}$	Open/Close	Yes	$REV7^{WT}$	Open/Close	Yes
$MAD2^{F141A}$	Open/Close	No	$REV7^{R124A}$	Open/Close	No
$MAD2^{\Delta N10}$	Close	Yes	$REV7^{\Delta N10}$	Close	Yes
$MAD2^{\Delta N15}$	Close	Yes	$REV7^{\Delta N15}$	Close	Yes
$MAD2^{\Delta C}$	Open	No	$REV7^{\Delta C}$	Close	No
$MAD2^{LL}$	Open	No	$REV7^{LL}$	Open	Yes
$MAD2^{\Delta N, LL}$	Close	Not tested	$REV7^{\Delta N, LL}$	Close	Not tested

3.4 Shieldin assembly involves closed-intermediate REV7 dimer formation

During the course of this PhD thesis two crystal structures of Shieldin complex containing REV7 dimer were published (Liang et al., 2020; Xie et al., 2021). The authors reported the presence of REV7 dimer in Shieldin complex in agreement with the data present in this thesis. The REV7 dimer was described as O-C conformational dimer based on the observation that the first protomer is present bound to SHLD3 in safety-belt conformation whereas the second protomer lacks the safety-belt interaction. Since formation of MAD2 open: closed conformational homodimer is a necessary step in MCC assembly (Mapelli et al., 2007; Faesen et al., 2017) I reasoned whether this is also true for Shieldin assembly. I used REV7 topology mutants generated in the previous section to assemble Shieldin complex. The complex assembly was monitored using SEC experiments where uncomplexed MBP-SHLD2 eluted as a distinct peak from MBP-SHLD2 in a complexed form (Figure 3.6A and B).

If Shieldin contains an O-REV7: C-REV7 dimer, presence of equimolar concentrations of $REV7^{\Delta N15}$ (C-REV7) and $REV7^{LL}$ (O-REV7) would enable assembly whereas presence of only $REV7^{\Delta N15}$ (C-REV7) would fail to assemble Shieldin. Surprisingly, the results show that Shieldin complex assembly is possible with equimolar concentrations of $REV7^{\Delta N15}$ and $REV7^{LL}$ as well as $REV7^{\Delta N15}$ alone suggesting Shieldin assembly is not mediated by canonical conformational dimer formation between REV7. The first protomer of REV7 ($REV7^{\Delta N15}$) binds SHLD3 in the safety belt conformation whereas incorporation of the second REV7 protomer in Shieldin can be either open or closed conformation ($REV7^{LL}$ /$REV7^{\Delta N15}$). The model in figure 3.6C shows the assembly of Shieldin complex revolving around conversion of REV7 from open to close for binding SHLD3 in safety belt conformation. This is followed by interaction of REV7-SHLD3 complex with SHLD2 which is mediated by incorporation of a second protomer of REV7 which is topology independent

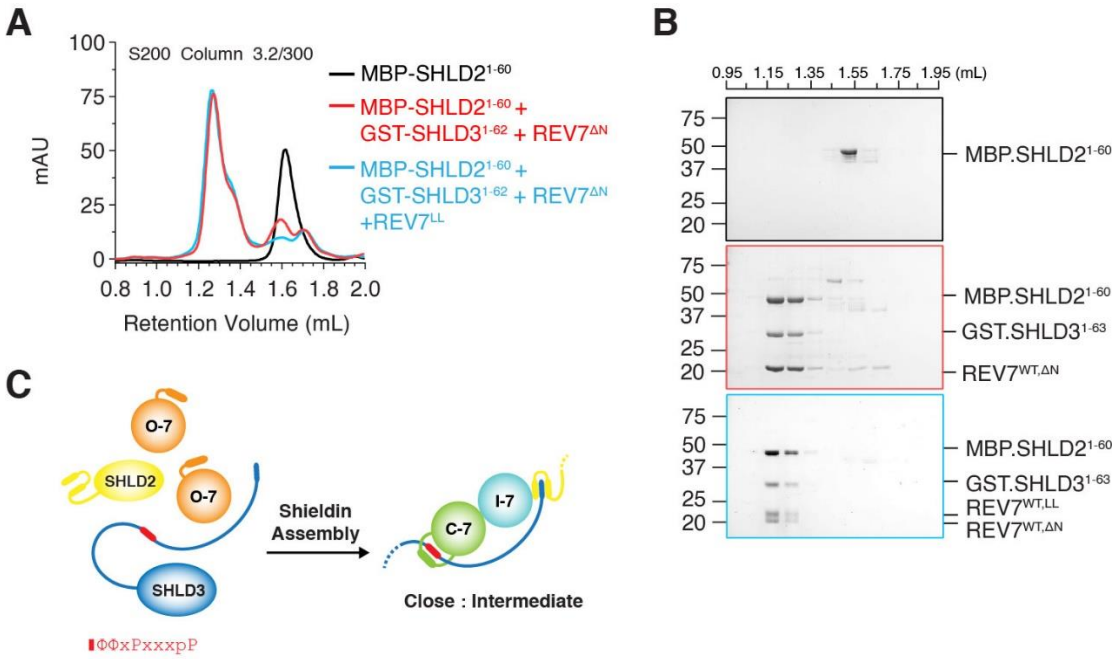

Figure 3.6: Shieldin complex contains C-REV7: I-REV7 dimer. (A) Size exclusion chromatography (SEC) profiles show the interaction between REV7^{WT}, GST-SHLD3$^{1–62}$ and MBP-SHLD2$^{1–60}$ on a Superdex 200 Increase 3.2/300 column. The peaks eluted at 1.25 ml are of the stable Shieldin complex composed of MBP-SHLD2$^{1–60}$-REV7^{WT}-SHLD3$^{1–82}$ while the peaks eluted at 1.6–1.7 ml are free REV7^{WT}. Black line represents free/uncomplexed MBP-SHLD2$^{1-60}$. Red line represents Shieldin complex formation by REV7$^{WT, \Delta N}$. Blue line represents Shieldin complex formation by REV7$^{WT,\Delta N}$ and REV7^{WT,LL}. **(B)** Coomassie-stained SDS-PAGE gels of SEC runs as shown in (A). **(C)** Cartoon representation of Shieldin assembly involving closure of REV7 (safety-belt interaction) on SHLD3-RBM followed by C-I dimer formation via dimerization interface and recruitment of SHLD2. Open conformer of REV7 is denoted as O-7 (orange), closed conformer of Rev7 is denoted as C-7 (green), and intermediate conformer of REV7 is denoted as I-7 (turquoise).

3.5 REV7-SHLD3 association shows slow binding kinetics.

REV7 and SHLD3 are the upstream components of Shieldin complex and are thus known to be necessary for Shieldin assembly (Gupta et al., 2018). Moreover, REV7 is a member of HORMA domain family that are known to bind their partner proteins in a unique safety-belt conformation and show small association rates. I hypothesized a similar underlining principle governing REV7-SHLD3 binding interaction. To test this, I sought to study REV7-SHLD3 association kinetics. For this, MBP-tagged $SHLD3^{28-83}$ (peptide containing REV7 binding peptide) was immobilised on Amylose beads. On adding eight-fold excess of $REV7^{WT}$, the reaction was allowed to proceed for indicated time points and terminated by removing soluble REV7 and washing twice with buffer. The samples were treated with 4x SDS loading dye and analysed using SDS-PAGE (Figure 3.7A). The SDS gel was digitized and the band intensities of both SHLD3 and REV7 were normalized and plotted as percentage binding against time (Figure 3.7B).

This experiment shows similar to MAD2, REV7 follows a similar slow binding kinetics, where the association rates are remarkably small. This unusual slow binding might be due to considerable energy requirement for topology switch which serves as a kinetic barrier for REV7-SHLD3 interaction. Interestingly, we observe the R124A mutant which is defective for dimerization, to be slower. This suggests that REV7 dimerization is one of the catalytic factors necessary for faster assembly of Shieldin complex. I tested K44A, R124A, A135D triple dimerization mutant of REV7 for SHLD3 binding which was shown to be more effective in breaking REV7 dimerization than R124A (Rizzo et al., 2018). I did not see any effect in binding kinetics as compared to R124A single mutant suggesting, the single mutant is sufficient in abolishing REV7 dimerization completely. Since fusion tags influence oligomeric states (Chen C. et al., 2013; Cheung et al., 2010), I introduced GST Fusion tags to $REV7^{WT}$ and $REV7^{R124A}$ and tested its ability to dimerize REV7 using SEC (Figure 3.8A and B). The idea here is that GST induced dimerization will supplement REV7 dimer defect brought by R124A by increasing the local concentration. As expected,

GST-REV7^{R124A} eluted at an apparent molecular weight of 98 kDa indicative of dimer similar to GST-REV7^{WT}. However, when testing GST-REV7^{R124A} for SHLD3 binding, I see partial rescue by GST tag of dimer defective R124A mutant.

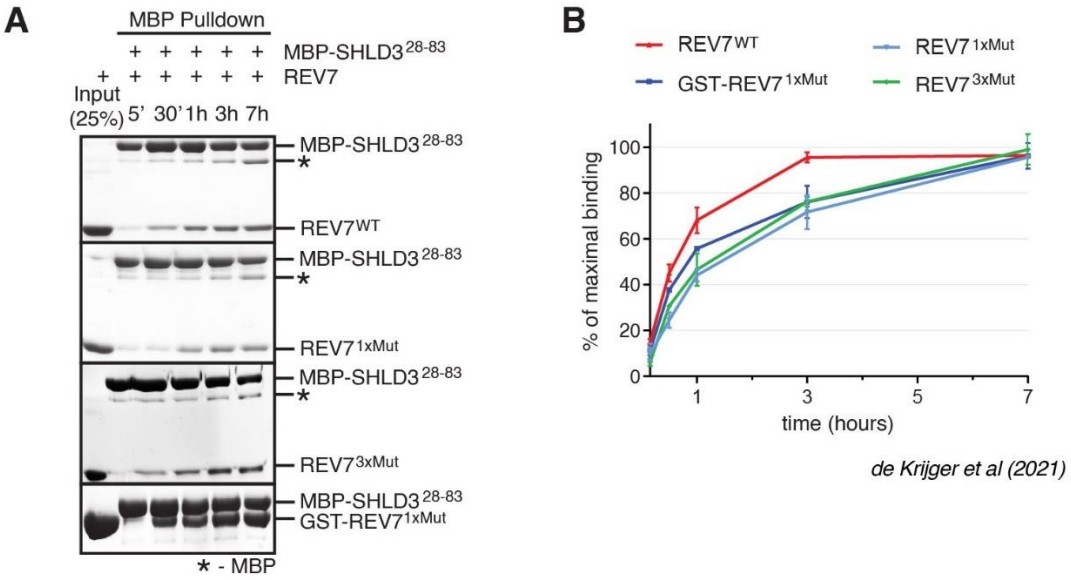

Figure 3.7: REV7 binding to SHLD3 follows an unusual slow kinetics. (A) Time course of Shieldin assembly between components REV7 and SHLD3 shows that assembly of SHLD3-REV7 complex is slow, but accelerated by REV7 dimerization. Coomassie-stained SDS-PAGE gels show a time course of pulldowns of MBP-SHLD3 (bait) and REV7-constructs (prey). The SHLD3-fragment used here contains only the RBM, which is captured by the seatbelt of REV7. A single-point mutation at R124 hinders REV7 dimerization and subsequently lowers binding kinetics (1xMut). Triple mutation (3xMut) of residues K44, R124, and A135 in the dimerization interface of REV7 has the same effect as 1xMut on binding kinetics. Inducing dimerization by creating GST-fusion partially rescues the assembly kinetics. Representative of n = 4 (REV7^{WT}/REV7^{1xMut}) or n = 2 (REV7^{3xMut}/GST-REV7^{1xMut}). **(B)** Graphical representation of data in (A). Red curve represents binding kinetics between REV7^{WT} and SHLD3$^{28-83}$ peptide. Light blue and green curves represent the reduction in binding kinetics of REV7^{1xMut} and REV7^{3xMut} with SHLD3$^{28-83}$. Dark blue curve represents partial restoration of binding kinetics between REV7^{1xMut} and SHLD3$^{28-83}$ induced by dimerization of the GST-tag on

REV7^{1xMut}. Graphs represent mean ± s.e.m, n = 4 for REV7^{WT}/REV7^{1xMut}, n = 2 for REV7^{3xMut}/GST-REV7^{1xMut}.

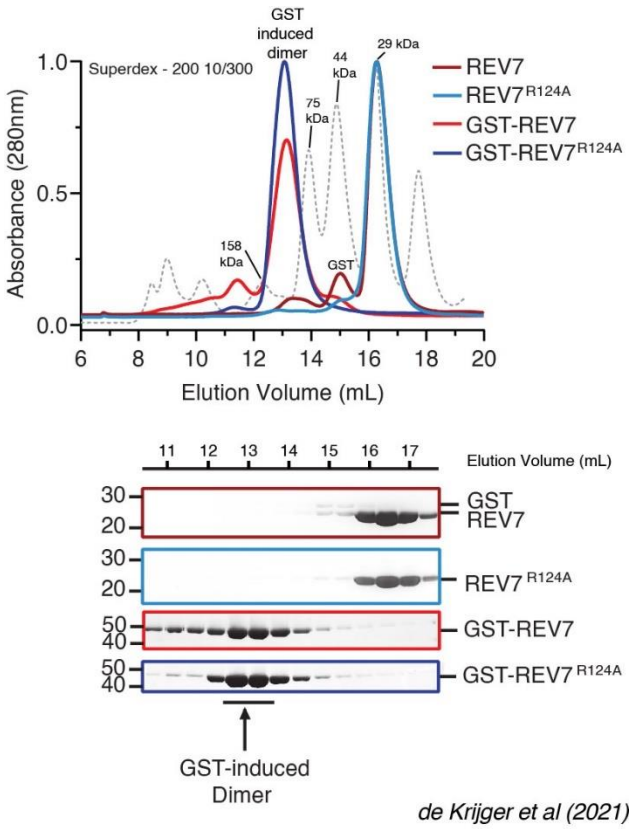

Figure 3.8: GST-induced dimerization of REV7^{R124A}. SEC profiles of REV7$^{WT/R124A}$ and N-terminal GST fusion REV7$^{WT/R124A}$ on Superdex-200 column. Coomassie-stained SDS-PAGE gels of REV7 constructs as shown in (lower panel)

Taken together, these results confirm a key hypothesis involving slow binding of HORMA REV7 to SHLD3. REV7 dimerization moderately increases the binding speed of Shieldin assembly.

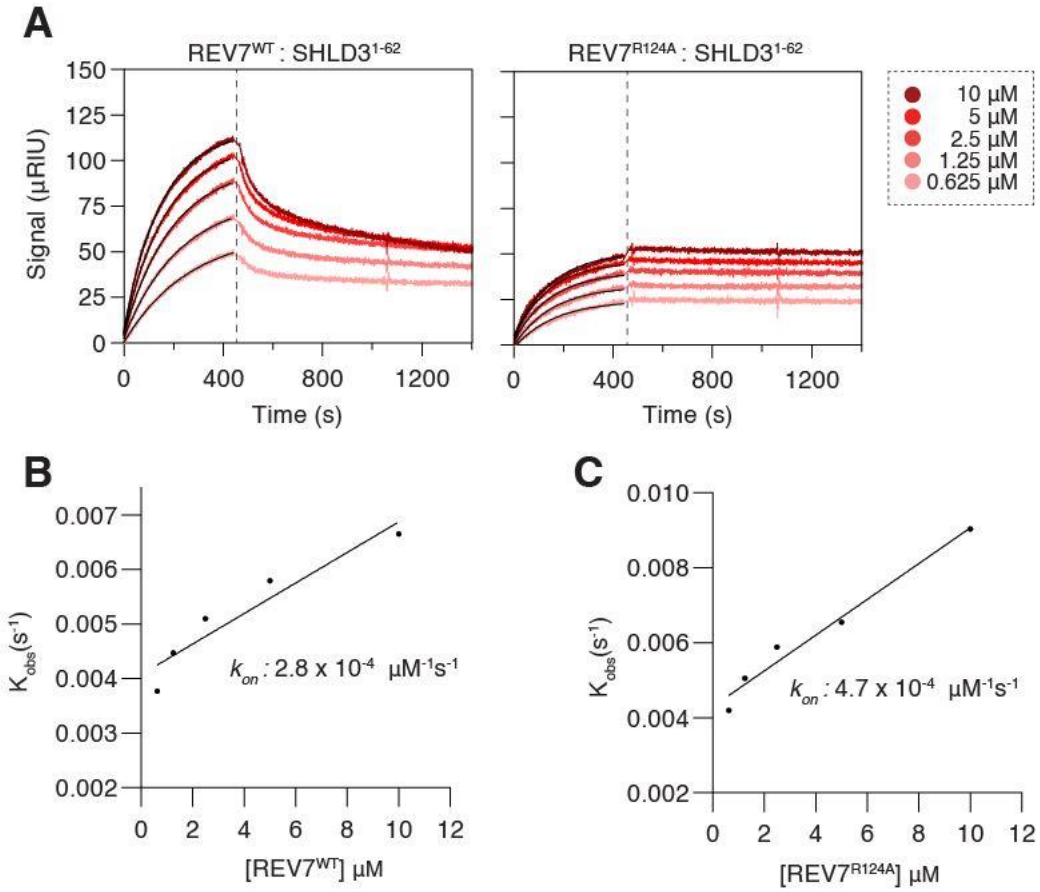

Figure 3.9: Binding Kinetics of REV7$^{WT/R124A}$-SHLD3$^{1-62}$. (A) Surface plasmon resonance sensogram showing the binding kinetics for REV7$^{WT/R124A}$ and immobilized SHLD3$^{1-62}$. Data are shown as red lines (different concentrations shown in the right panel as a subset), and the best fit of the data to a 1:1 binding model is shown in black for association phase. **(B)** Determination of k_{on} (association rate constant) for binding between REV7^{WT} - SHLD3$^{1-62}$ and **(C)** for binding between REV7^{R124A}- SHLD3$^{1-62}$.

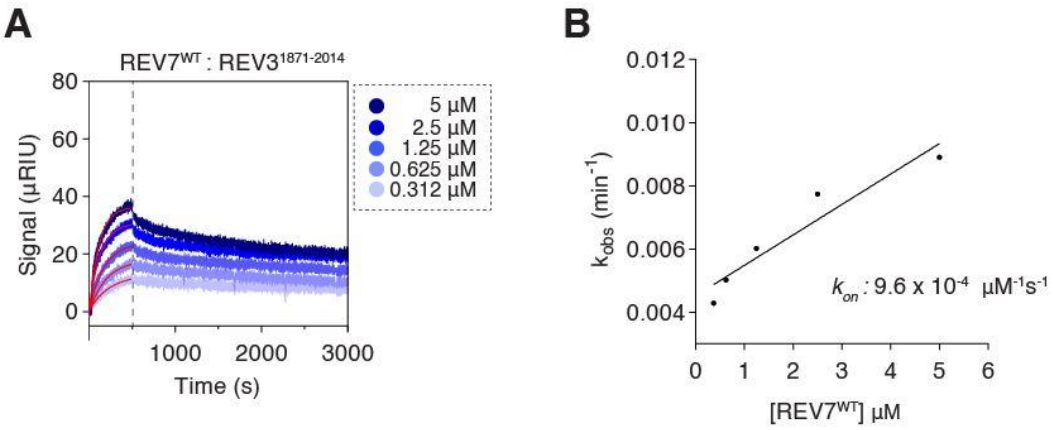

Figure 3.10: Binding kinetics of REV7^{WT}-REV3$^{1871-2014}$. (A) Surface plasmon resonance sensogram showing the binding kinetics for REV7^{WT} and immobilized REV3$^{1871-2014}$. Data are shown as blue lines (different concentrations shown in the right panel as a subset), and the best fit of the data to a 1:1 binding model is shown in red for association phase. **(B)** Determination of k_{on} (association rate constant) of REV7^{WT} for REV3$^{1871-2014}$.

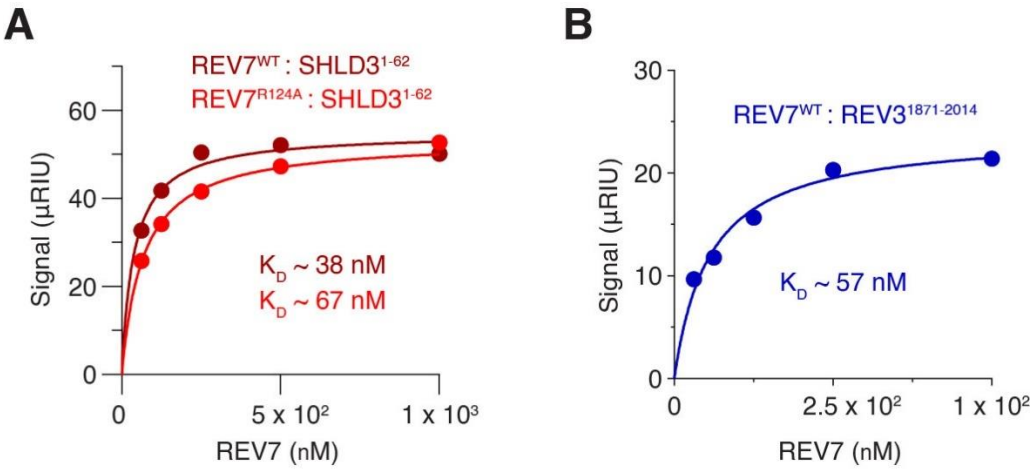

Figure 3.11: Determination of K_D of REV7$^{WT/R124A}$-SHLD3$^{1-62}$ and REV7^{WT}-REV3$^{1871-2014}$. (A) Equilibrium dissociation constant (K_D) for REV7$^{WT/R124A}$-SHLD3$^{1-62}$ was calculated from SPR curves. The peak response values (Y) in the dissociation phase for different analyte concentrations were plotted against the respective analyte concentration value (X). The K_D was determined using a one site-specific binding equation (GraphPad). **(B)** A similar analysis as in (A) was carried out for REV7^{WT}-REV3$^{1871-2014}$.

Next, I tried to quantify the association rates for REV7 binding to SHLD3 using surface plasmon resonance (SPR). To do this, I immobilized SHLD3 on SPR chip using EDC-NHS coupling reaction. REV7 at different concentrations was passed on SHLD3 and the sensogram was recorded. To begin, I first calculated the K_D of the binding interaction using inbuilt affinity evaluation program of TraceDrawer. The experimental binding strength from my experiments of ~ 38 nM was in agreement with reported K_D of ~15 nM (Gupta R. et al., 2018, Dai Y. et al., 2020) (Figure 3.11A). As expected, and in line with my *in-vitro* pulldown experiments, REV7 showed a slow association rate of 10^{-4} $\mu M^{-1}s^{-1}$ (Figure 3.9A right panel and B). MAD2 shows a similar association rate constant (k_{on}: 10^{-5} $\mu M^{-1}s^{-1}$) when binding to CDC20 (Piano V. et al., 2021, Simonetta et al., 2007). Unsurprisingly, REV7 binding to SHLD3 peptide showed no visible dissociation. This is expected for safety-belt interaction and similarly observed for MAD2-CDC20 binding (Piano et al., 2021). Also, I find the REV7 WT and R124A both show similar binding kinetics (Figure 3.9A, B and C). This is in contrast to the *in-vitro* pulldowns results which show a difference in association rates between WT and dimer defective R124A mutant. A similar difference in pulldown experiments (Simonetta et al., 2007) and recently performed FRET experiments could be seen in case of MAD2 (Piano V. et al., 2021). This could be possibly due to MAD2 requiring conformational dimer formation for CDC20 binding whereas in Shieldin REV7 homodimerization is topology independent. Moreover, my purifications yield closed conformer of REV7 which is proficient in SHLD3 binding.

Next, I tested binding kinetics of REV7 to REV3 peptide and observed similar small association rate (k_{on}: 9.6 x 10^{-4} $\mu M^{-1}s^{-1}$) (Figure 3.10A and B) (see Figure 3.7B for calculated binding strength of REV7-REV3 interaction). This confirms that the kinetic mechanism behind Shieldin assembly and that of other REV7 containing complexes like DNA Polymerase ζ is similar.

Taken together, the kinetic analysis here on REV7 confirms the hypothesis that REV7 conformational conversion is very slow and is the rate limiting step in Shieldin assembly.

3.6 SHLD3 contains a DNA binding domain

Multiple studies reported SHLD2 can bind DNA and is therefore involved in recruiting Shieldin to DSBs (Noordeermer et al., 2018, Dev et al., 2018, Gao et al., 2018; Findlay et al., 2018). However, Shieldin assembly at DNA breaks follows hierarchical recruitment where SHLD3 co-localises first followed by REV7 and then SHLD2-SHLD1 (Gupta et al., 2018). This suggests SHLD3 is either recruited through protein-protein interaction mediated by possible upstream factors or through direct interaction with DNA. Interestingly, while purifying Shieldin complex, I noticed the complex could bind Resource S and Heparin columns (Figure 3.12A and B). This indicates Shieldin complex contains an electropositive patch present on either one of the proteins. Since protein binding heparin columns are potential DNA binders, I hypothesized Shieldin complex contains a DNA binding protein. To test this, I incubated 5,6-FAM labelled ssDNA with Shieldin complex and carried out SEC analysis. The result showed that our complex lacking full-length SHLD2 could still associate with ssDNA suggesting an additional DNA binding protein in the Shieldin complex (Figure 3.12C upper and lower panel). Next, I quantified Shieldin's DNA binding affinity using various DNA substrates. The results show that Shieldin could bind both ssDNA and dsDNA with equal affinity and shows no selective preference between telomeric and non-telomeric substrates (Figure 3.13A and B). Together, this supports the possibility that Shieldin contains multiple DNA binding proteins.

Since the complex purified here contained two copies of REV7 and an N-terminal peptide of SHLD2 with none of them potential DNA binding candidates, I focused my search on SHLD3. The N-terminus comprising of residues 1-83 is required to form Shieldin complex (Liang et al., 2020). To test whether the DNA binding activity lies in C-terminal region, I purified a truncated variant of Shieldin complex that lacked C-terminal region from residues 83-250 of SHLD3. This SHLD3 construct can still form Shieldin complex. This complex eluted at the appropriate molecular weight on a SEC (Figure S2). I then tested which of these two complexes could bind ssDNA. As expected, Shieldin complex lacking

C-terminus of SHLD3 was unable to bind ssDNA (Figure 3.14). This result show that the Shieldin complex contains an additional DNA binding domain in SHLD3.

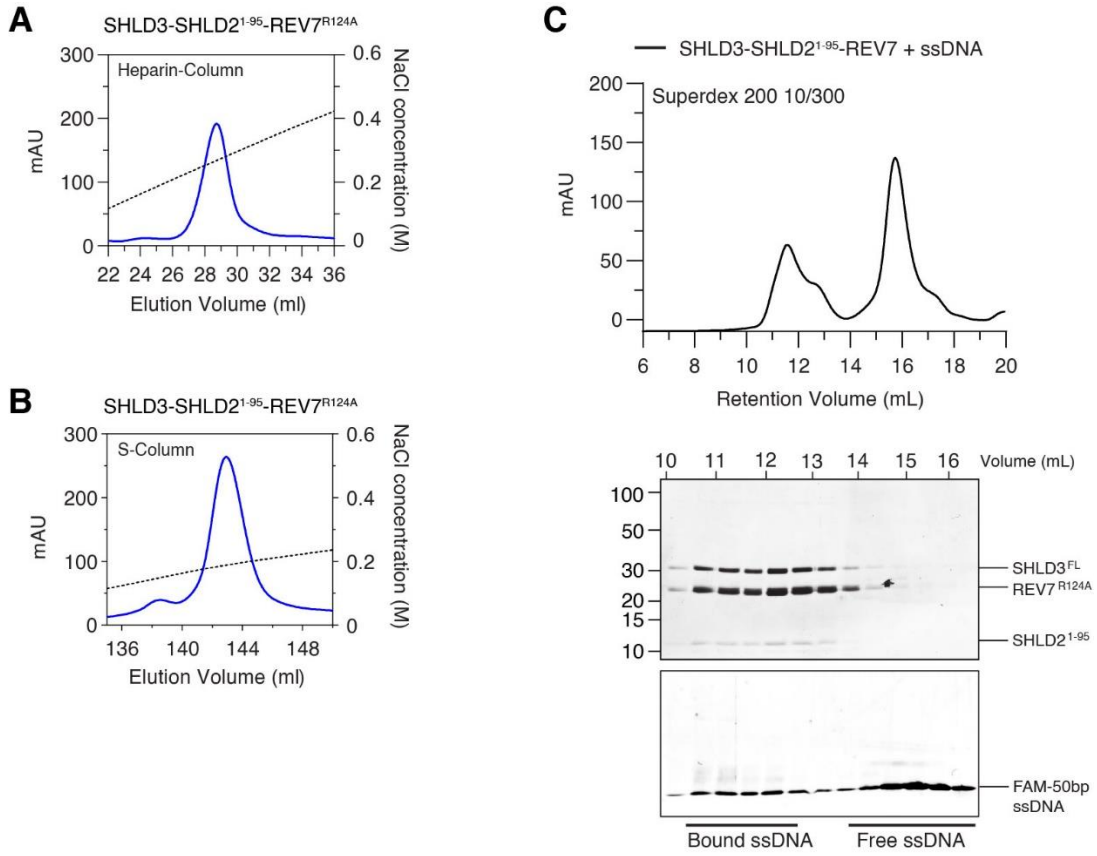

Figure 3.12: Shieldin complex exhibits DNA binding activity outside SHLD2. (A) Purification of Shieldin complex on 1 mL Heparin column. Shieldin complex elutes at higher concentration of salt of approximately ~ 250 mM NaCl. **(B)** Purification of Shieldin complex on 1 mL Resource S column. Shieldin complex elutes at higher concentration of salt of approximately ~ 220 mM NaCl. **(C)** SEC profile of Shieldin complex (SHLD3-SHLD2$^{1-95}$-REV7^{R124A}) bound to 5,6-FAM labelled ssDNA on Superdex-200 10/300 column. The peak eluted at 11-12 mL represents Shieldin complex bound to ssDNA, the peak eluted at 13 mL is of free Shieldin complex and the peak eluted at 15-17 mL is free 5,6-FAM labelled ssDNA (upper gel). Bound and free ssDNA species were visualised using fluorescence readout from the conjugated 5,6-FAM dye using a green filter (lower gel).

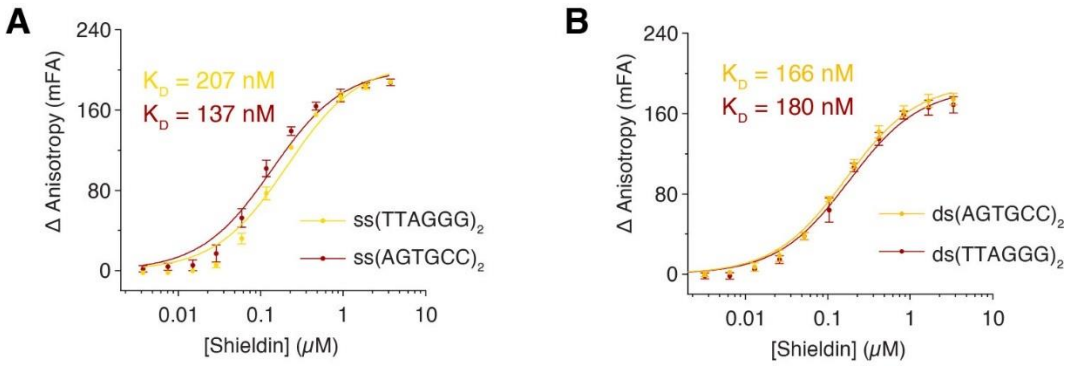

Figure 3.13: **Shieldin complex exhibits similar binding affinities for different DNA substrates. (A)** Fluorescence anisotropy measurement of Shieldin complex for binding affinities against non-telomeric ss- or ds-DNA. **(B)** Fluorescence anisotropy measurement of Shieldin complex for binding affinities against telomeric ss- or ds-DNA. Error bar represents s.d. (n = 3 independent experiments)

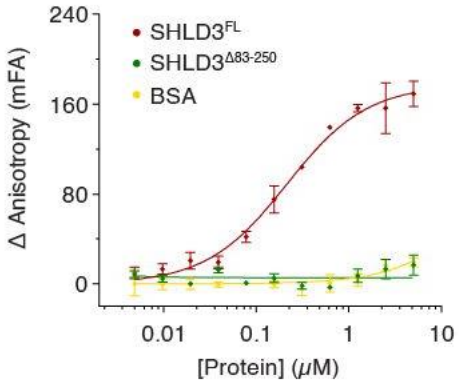

Figure 3.14: **SHLD3 is a DNA binding protein.** Fluorescence anisotropy measurement of different Shieldin complexes for binding affinities against ssDNA substrate. Shieldin complex with deletion of SHLD3 residues 83-250 is deficient in DNA binding. Brown line represents Shieldin complex, green line represents Shieldin complex$^{\Delta SHLD3\text{-}CTD}$, yellow line represents BSA. Error bar represents s.d. (n = 3 independent experiments).

3.7 SHLD3 contains a conserved C-terminal DNA binding domain.

Since SHLD3 C-terminus contains DNA binding activity, I tried to understand molecular basis of DNA binding. To do this, I first sought to purify SHLD3 C-terminus. I subjected Shieldin complex to protease digestion using different proteases (Figure S1B and Figure 3.15A). As expected, HORMA REV7 which is completely folded was resistant to all proteases except subtilisin which was used as a positive control for protease digestion. In contrast, SHLD3 was digested by all proteases with varying degrees. A stable fragment was released of ~ 17 kDa which on longer incubation was digested further to 13 kDa (Figure S1B and Figure 3.15A). This digestion pattern was seen for SHLD3 in complex with REV7 or with REV7-SHLD2 suggesting SHLD3 is not entirely folded and contains flexible regions which are fairly unprotected by REV7-SHLD2 binding. (Figure S1A snd B). Disorder prediction suggested the N-terminal region (residues 1 – 135) to be disordered while the C-terminal region (residues 140-250) to have higher degree of order. Consurf analysis of SHLD3 showed the C-terminal region to be well conserved across multiple species (Figure S4 and Figure 3.15B). I purified a stable C-terminal truncated construct (residue 139 - 250) of SHLD3 which eluted as a monomer in solution in line with Shieldin complex containing a single copy of SHLD3. This fragment was able to bind Resource S and Heparin columns similar to full-length construct of SHLD3 in the Shieldin complex suggesting presence of DNA binding activity (Figure S3 and Figure 3.16A).

Indeed, similar to full-length construct this C-terminal fragment could bind ssDNA and would release the DNA substrate when incubated with excess unlabelled ss or ds DNA (Figure 3.16B). Next, I tested the affinity of this fragment to various DNA substrates. Again, similar to full-length construct this fragment could bind multiple DNA subtrates with similar binding affinity (Figure 3.17A and B). Together, this results show that Shieldin complex contains a DNA binding protein in SHLD3 and the acitivity resides exclusively in its C-terminal domain.

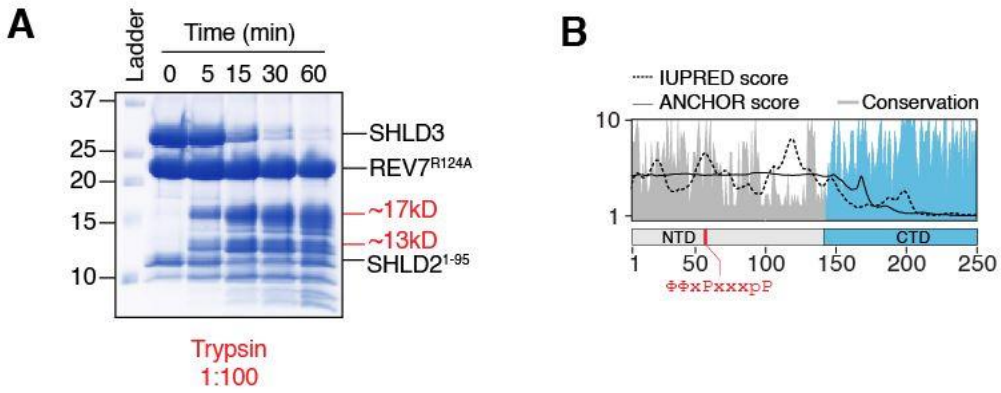

Figure 3.15: SHLD3 contains a folded and conserved C-terminal region. (A) Proteolytic digestion of Shieldin complex with trypsin (100:1 molar ratio of Shieldin to trypsin) shows stepwise degradation of SHLD3 to a 17 kDa fragment and then to 13 kDa fragment. **(B)** Disorder prediction of SHLD3 using IUPRED shows the N-terminal domain (residues 1-150) to be disordered while the C-terminal domain to be ordered (Erdős et al., 2021). The conservation score (CONSURF) shows higher degree of conservation in the N-terminal region comprising of residues 1-83 and C-terminal region comprising of residues 140-250 (Ashkenazy et al., 2016).

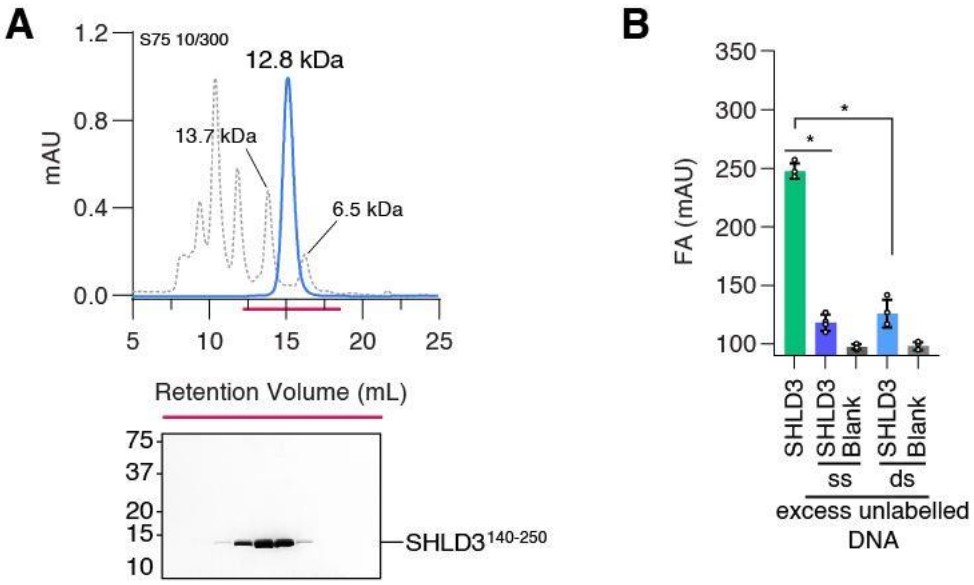

Figure 3.16: SHLD3 contains a C-terminal DNA binding domain. (A) SEC profile of SHLD3$^{140\text{-}250}$ on Superdex-75 10/300 column **(B)** Competition assay shows SHLD3(CTD) binds both ss-DNA similar to full length SHLD3. It could further compete out using either 100-fold ss-DNA or ds-DNA. Error bar represents s.d. (n = 3 independent experiments). One-tailed Student's test are indicated: *p < 0.001.

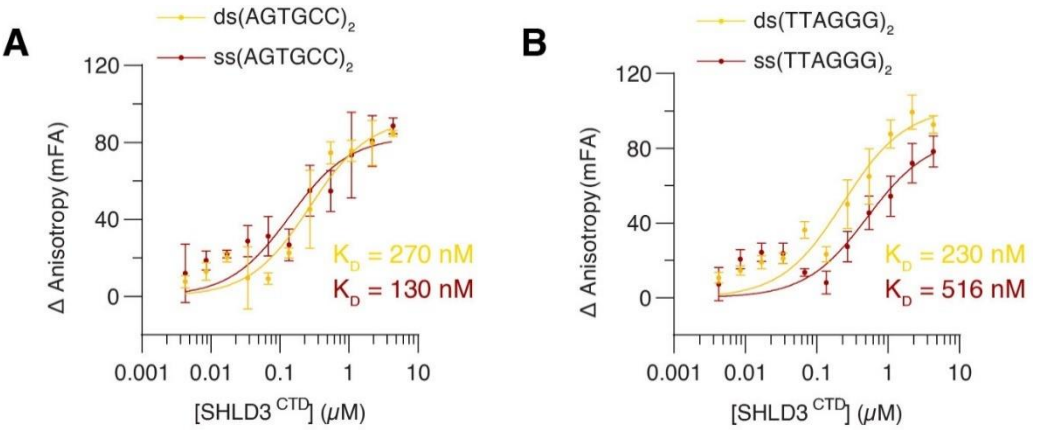

Figure 3.17: SHLD3-CTD exhibits similar binding affinities as full-length SHLD3. (A) Fluorescence anisotropy measurement of SHLD3-CTD for binding affinities against non-telomeric ss- and ds-DNA. **(B)** Fluorescence anisotropy

measurement of SHLD3-CTD for binding affinities against telomeric ssDNA and dsDNA. Error bar represents s.d. (n = 3 independent experiments)

Next, I decided to model SHLD3 C-terminal domain using Alphafold 2 and RoseTTA fold (Jumper et al., 2021; Baek et al., 2021,). To do this, I used Colabfold which matches Alphafold2 and RoseTTAfold. Colabfold is 20-30 times faster than Alphafold in predicting 3D models due to its replacment of Alphafolds input feature generation step with fast MMseq2 search (Steinegger and Söding 2017; Mirdita et al., 2021). Briefly, the full-length sequence of SHLD3 was submitted to Colabfold and 3D modelled using default settings with no templates. This provided high quality predictions for SHLD3 with high confidence scores in C-terminal region as compared to N-terminal region which calculated by pLDDT score (higher score denotes high confidence and lower score denotes low confidence) (Figure S5 and S6). As excepted from sequence aligments, SHLD3 models both from Alphafold 2 and RoseTTA fold showed N-terminal region to be unfolded and C-terminal region to contain a folded domain (Figure 3.18A and B). This is in agreement with our biochemical analysis. Interestingly, even though SHLD3 N-terminus is unfolded it showed well predicted secondary structure elements with α-helices at position 19-27 and 62-75 that correspond to the crystal structure data (Dai et al., 2019; Liang et al., 2020; Xie et al., 2021).

The fold adopted by C-terminus of SHLD3 is very similar to EIF4-E with a RMSD score of 5.138 suggesting shared biochemical function. Expectedly , EIF4-E is a protein involved in translation initiation that contains nuceotide binding activity. The nucleotide binding cavity in EIF4-E is composed of extensive loop regions with several conserved basic amino acids identified to be involved in DNA binding (Sekiyama et al., 2015). Suprisingly, such extensive loops are absent in SHLD3 C-terminus. Despite this, it retains a putative electropositive patch which could potentially bind ssDNA or dsDNA (Figure 3.18C). To investigate this, I identified two residues H242 and K243 present within the electropositive patch to be invariantly conserved across multiple species conatining SHLD3 subunit of Shieldin (Figure 3.19A and Figure S4). Mutating H243 and K243 to alanine reduced

SHLD3 DNA binding affinity to both ssDNA and dsDNA. (Figure 3.19B). Moreover, I show the same residues are involved in binding to ssDNA and dsDNA containing telomeric sequences (Figure S7). Taken together, these results show that C-terminal domain contains electropositive patch which is necessary for SHLD3 to bind DNA.

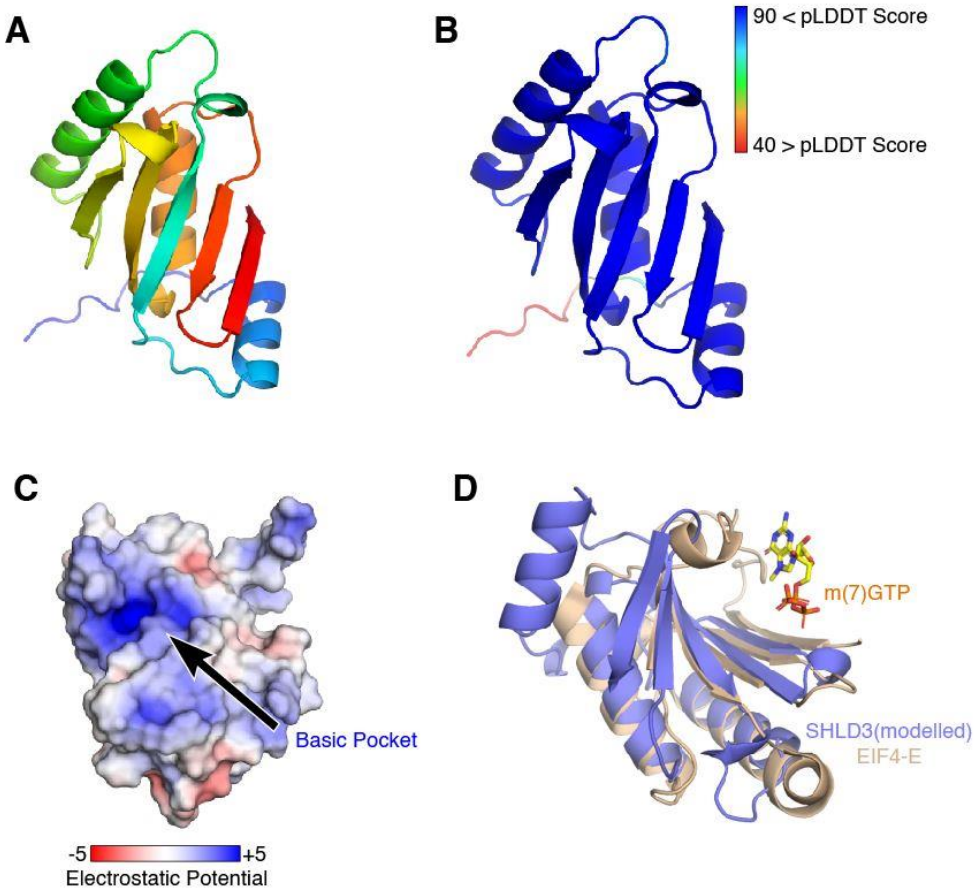

Figure 3.18: Alphafold2 prediction of C-terminal domain for SHLD3. (A) Predicted 3D-structure of SHLD3 C-terminal domain (CTD) comprising of residues 139-250. (Model: cartoon, colour: rainbow) **(B)** Confidence score retrieved from Alphafold2 shows very high confidence in model (pLDDT score of > 90 suggest highly accurate model) **(C)** Surface electrostatic analysis reveals presence of an electropositive patch in SHLD3-CTD. **(D)** Structural alignment of SHLD3-CTD (modelled) and human EIF4-E (PDB: 5BXV) shows SHLD3-CTD adopts fold similar to nucleotide binding EIF4-E. Proteins are coloured as

follows; SHLD3-CTD (marine blue), EIF4-E (beige), m (7) GTP shown as stick model.

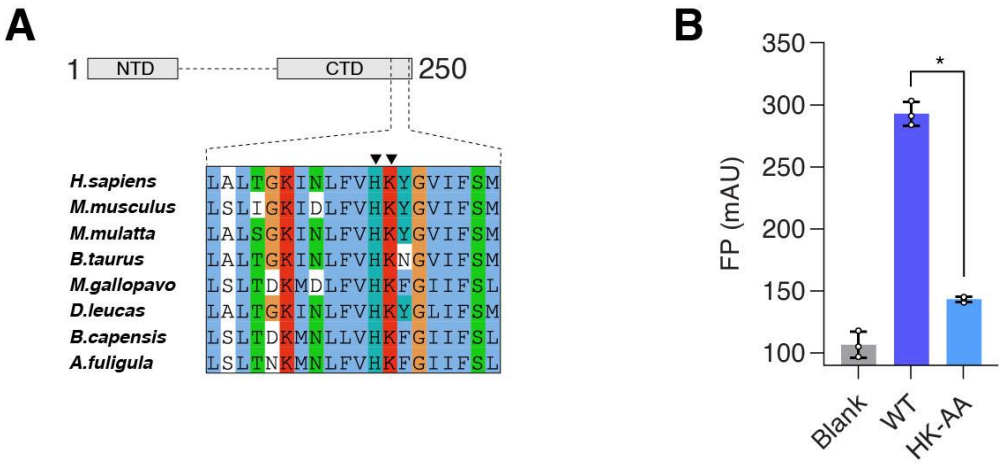

Figure 3.19: Mutagenesis of conserved H242 and K243 reduces SHLD3-CTD's DNA binding affinity. (A) Residues H242 and K243 are well-conserved across SHLD3 homologues from higher eukaryotes. Sequence alignment was performed with Clustal package in Jalview (Waterhouse et al, 2009; Sievers et al., 2011). Residues are coloured according to Clustalx scheme, where the conserved residues are coloured as follows: blue (hydrophobic), red (positively charged), orange (glycine), cyan (Hydrophobic) and green (polar). **(B)** Mutation of H242 and K243 to alanine reduced binding affinity of SHLD3-CTD to ssDNA. Error bar represents s.d. (n = 3 independent experiments). One-tailed Student's test are indicated: *$p < 0.001$.

4. Discussion

This thesis provides mechanistic insights into Shieldin complex assembly and DNA binding. By biochemical reconstitution of the Shieldin complex, I have shown REV7 undergoes homodimerization in order to recruit downstream Shieldin complex subunits for optimal activity. Moreover, Shieldin assembly centered around REV7-SHLD3 interaction at DSB site is unusually slow. I have provided mechanistic insights into recruitment of Shieldin complex at DSBs by showing that SHLD3 is a DNA binding protein. SHLD3 interacts directly with DNA and together with REV7 assembles Shieldin complex to initiate the DSB repair by NHEJ. In the following section, the results from this project are discussed.

4.1 Shieldin assembly is cooperative

MCC assembly for SAC activation is cooperative. To test whether this is also true for Shieldin, I purified REV7 with SHLD3 and SHLD2 N-terminal fragment. In the presence of SHLD2 N-terminus, a REV7 dimer was purified bound to a single SHLD3. Also, I noticed REV7 dimer mediated by SHLD2 can compensate a single point mutant in the dimer interface. This suggested SHLD2 could mediate REV7 dimer formation not through the dimer interface but rather through a novel binding interface possibly via an allosteric interaction. During the course of this thesis the crystal structure of REV7-SHLD3$^{1-62}$-SHLD2$^{1-60}$ was published (Liang et al., 2020; Xei et al., 2021). These structures show that indeed REV7 forms a dimer in Shieldin complex in agreement with our *in vitro* data. Moreover, it showed REV7 forms dimer using canonical dimer interface similar to how MAD2 forms conformational dimer. The study shows Shieldin complex fails to assemble when R124 mutant is introduced in REV7. Surprisingly, when I used the R124 mutant I

was able purify the full complex from insect cells. This discrepancy can be explained as even though R124 mutant fails to dimerize alone in solution, even at high concentrations (up to 50 µM) similar to MAD2, the extensive intramolecular interactions within the complex are likely to compensate a single point mutant in the dimer interface suggesting a potential for cooperative assembly. In support of this idea, the complete loss of SHLD2 from the SHLD3-REV7 complex in cells was observed only when mutation of two more residues (K44 and A135) was introduced in the dimer interface, (de Krijger et al., 2021) suggesting $REV7^{R124A}$ in cells can assemble Shieldin complex.

Moreover, the report from Liang et al., 2020 claims REV7 dimer is mainly mediated by SHLD3 with SHLD2 playing a supportive role. This is because they observe REV7 dimer with SHLD3 N-terminus alone. This is in contrast with my observation where $REV7^{WT}$-SHLD3 elutes as a monomer. This can be explained as I purify preformed complex from insect cells. Liang et al., worked with WT REV7 which is reported to form dimer at concentrations of 10 µM or more (Rizzo et al., 2018). My data shows at a concentration of 10 µM REV7 is mainly present as a dimer. It is possible that the REV7 dimer Liang et al., measured in $REV7^{WT}$-SHLD3 by SEC-MALLS could be REV7 dimer in isolation. They concluded that, the dimer was stabilized in presence of SHLD2. This in agreement with what I see with my sample. This shows Shieldin complex contains two more weak interaction sites outside the safety belt interaction between REV7-SHLD3. This includes REV7 dimerization and SHLD2-REV7 β-sheet interaction. Additionally, Liang et al., reports SHLD3 contains a conserved FXPWFP motif that binds REV7 at C-terminus (Figure S4). Taken together, these different observations regarding Shieldin stability suggests that Shieldin follows cooperative model of assembly wherein the interaction of individual subunits are dynamic. However, the relative contributions of individual components to overall stability of Shieldin are still unclear and would require further investigation.

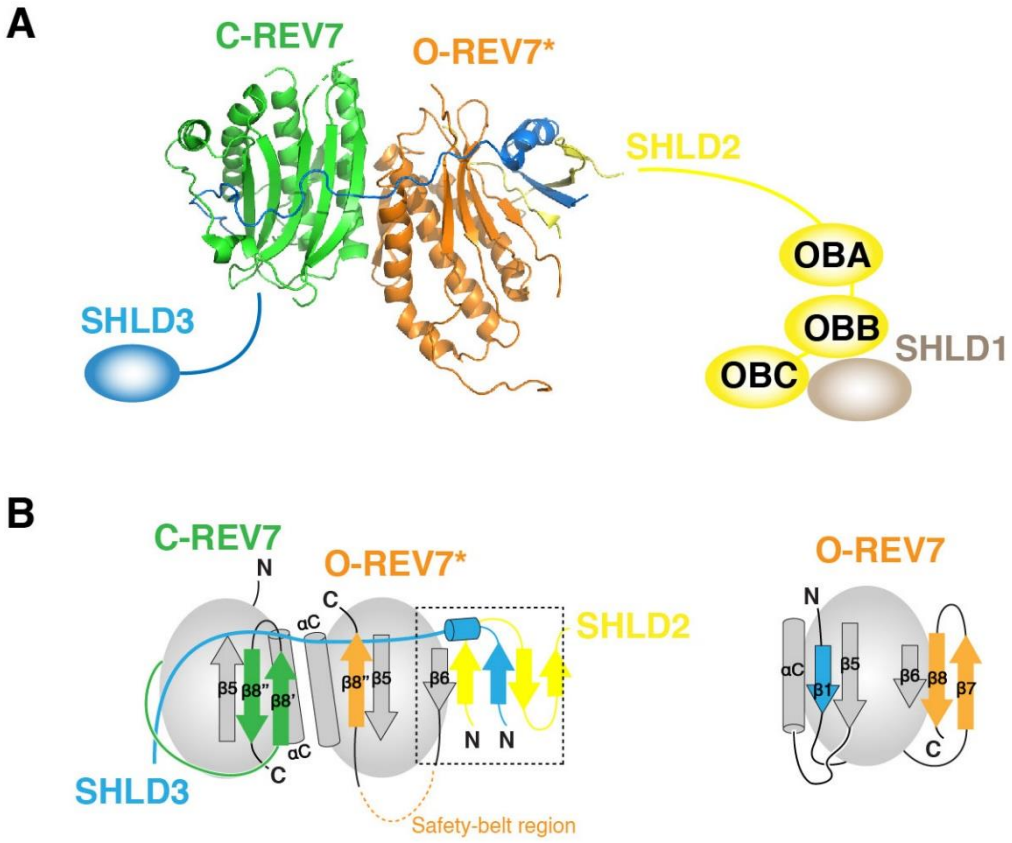

Figure 4: Shieldin complex containing C-O* REV7 dimer reported by Liang et al., 2020. (A) Crystal structure of Shieldin complex containing C-O* REV7 dimer (green and orange, respectively), SHLD2 (yellow), SHLD1 (brown) and SHLD3 (blue) [PDB: 6KTO]. **(B)** Topology diagram of Shieldin complex as in (A). C-REV7 binds SHLD3 in canonical safety-belt conformation. O-REV7* binds SHLD2 and SHLD3 by forming extended β-sheet interaction as shown in dotted box. The safety-belt region is flexible (orange dotted line). The β-sheet interaction is mediated by β6 of O-REV7*. In O-REV7*, C-terminus (β8) interacts with β5 (this is the relative C-terminus position after relocation on conversion of O-REV7 to C-REV7). In classical O-REV7 state, C-terminus (β8) interacts with β6.

4.2 REV7 forms topology independent dimers

Liang et al., 2020 reported REV7 dimer in Shieldin complex to be a closed: open dimer similar to MAD2 conformational dimer (Figure 4). This classification seems to be based on the fact that only one of the REV7 protomer is present in a safety belt conformation. The data presented in this thesis supports the observation that the first protomer of REV7 is closed with the SHLD3-RBM entrapped in the safety belt conformation. The second protomer appears to be unusual in that though it binds SHLD2 at a similar interface as SHLD3 RBM in the adjacent protomer it lacks a safety belt interaction. This would mean only the conversion of the first protomer is necessary for Shieldin assembly. This would have major implications for kinetic study of Shieldin assembly which is an important part of this thesis.

Moreover, whether the second REV7 protomer identified by Liang et al., 2020 is in open REV7 conformation within the Shieldin complex is not tested. Thus, in this thesis, I sought to characterise the topology of REV7 dimer. Prior to this report, a study showed that indeed REV7 can exist as open state and similar to MAD2 these two states can be separated on a Q column (Clairmont et al., 2020). I purified stable open and closed states of REV7 based on MAD2 topology trapping mutants (Mapelli et al., 2006; Mapelli et al., 2007). When tested in isolation REV7 formed dimers form both open and closed states suggesting REV7 dimerization is topology insensitive. An equimolar amount of SHLD2, SHLD3, O-REV7 and C-REV7 when mixed could form stable Shieldin complex. Interestingly, equimolar of SHLD2, SHLD3, C-REV7 and C-REV7 when mixed could also form stable Shieldin complex. This suggests REV7 can form O-C and C-C dimers within Shieldin complex. This is similar to MAD2 were O-C and C-C dimers are possible. The likely explanation for this in Shieldin complex is that the first protomer REV7 binds SHLD3 in the safety belt conformation while the second protomer (open or closed REV7) can interact with SHLD2 as the safety-belt is not involved. This suggests binding of the second protomer is topology independent in line with my hypothesis. Indeed, the crystal structure shows the N-terminal β1-strand of O-REV7* is unstructured suggesting the conformer is most likely is not in its

canonical open state. Additionally, C-terminal region (β8'') interacts with β5 similar to what is observed in the closed state. Despite this it does not use its safety belt interaction. The residues 5-11 of SHLD2 form β strand interaction with β5 of REV7. It is likely that the core of HORMA REV7 mediates SHLD2 binding. This is likely possible as I observe both locked C-REV7 and locked O-REV7 can form homodimers suggesting REV7 lacks a conformational dimer and the dimer formation is mediated by its core alone. Together, these results suggest Shieldin assembly requires conversion of only one protomer of REV7 from open to closed state. Whereas, the second protomer can be incorporated from the pool of free REV7 present in the cells.

The "open" REV7 identified by Liang et al (2020) seems to appear similar to the hypothesised intermediate state of MAD2 (I-MAD2) which shows disordered N and C-terminus yet a stable HORMA core. Moreover, this state is hypothesized to be less stable and thus has short half-life. It's unlikely that "open" REV7 identified in Shieldin complex would be stable in this state in absence of SHLD2. Due to structural ambiguity of this state with either O-REV7 or C-REV7 and the observation that both open and closed REV7 can readily convert to it, I propose that that Shieldin complex contains a novel C-REV7: I-REV7 dimer mediated by SHLD2-SHLD3 interaction wherein stabilization of the intermediate state by interaction with SHLD2 N-terminus is necessary for Shieldin assembly and function.

4.3 REV7 dimer presents scaffolding potential

Pol-ζ and Shieldin complex both contain REV7 dimers. Interestingly, the dimers are associated with binding to additional factors REV1 in case of Pol-ζ and SHLD2 in case of Shieldin. MAD2 does not form a constitutive dimer in MCC. Rather MCC assembly takes place via a transient C-MAD2:O-MAD2 conformational dimer formation. The LL mutant of MAD2 was engineered specifically for stabilizing conformational dimer by locking MAD2 in an open conformer (Mapelli et al., 2007). Moreover, the conformational

dimerization of MAD2 is thought to play an essential role in binding of MAD2 to CDC20 thereby suggesting a functional rather than a structural role. This is unlike in human Shieldin where REV7 dimerization is shown to play both structural as well as a functional role. This is also suggested in yeast Pol-ζ where the presence of two REV7 protomers makes the polymerase more rigid as compared to Pol-δ which contains similar subunits like Pol-ζ both structurally and functionally but lacking REV7 dimer (Malik et al., 2020; Du Truong et al., 2021). Moreover, REV7 is involved in binding and recruiting other inserter polymerases like REV1 in association with Pol η/ι/κ. This is similar to Shieldin complex where dimer formation allows for SHLD2 binding. Whether REV7 is able to form such structural dimers with CHAMP1 and other binding partners is yet to be studied. Together, these studies show a divergent role of REV7 from MAD2. Presence of HORMA dimer is also seen in mammalian as well as fission yeast autophagy where HORMA domain proteins ATG101 and ATG13 form constitutive dimer (Qi et al., 2015; Suzuki et al., 2015). This suggests REV7 mediated assembly of supra molecular complexes seem to rely on binding two protomers of REV7. In human Shieldin, REV7 shows dimer formation using its dimer interface in a head-to-head arrangement whereas in yeast Pol-ζ the arrangement is head to tail (Liang et al., 2020; Malik et al., 2020). These studies show REV7 is able to assemble supra molecular complexes through the structural plasticity of its HORMA domain.

4.4 REV7 dimerization and Shieldin disassembly

For MCC disassembly by TRIP13, CDC20 bound MAD2 undergoes dimerization through the dimer interface with another HORMA domain protein $p31^{comet}$ (Yang et al., 2007). $p31^{comet}$ serves as an adaptor for recruiting TRIP13 to MCC. *In vitro* studies show $p31^{comet}$ is necessary for TRIP13 binding and disassembly of MAD2 (Ye at al., 2017; Alfieri et al., 2018). Moreover, in absence of $p31^{comet}$ TRIP13 shows weak activity towards MAD2:CDC20 complex (Ye et al., 2015). Similar to C-MAD2: $p31^{comet}$ dimer we identify

a constitutive REV7 dimer in Shieldin. We suspect this dimer may play an active role in disassembly of Shieldin complex. As expected, we observe p31^{comet} is not necessary for binding of TRIP13 to Shieldin complex possibly due to absence of free REV7 dimer interface in Shieldin complex. Indeed, Shieldin complex containing REV7 in dimeric but not monomeric state is able to bind TRIP13 (de Krijger et al., 2021). A recent Cryo-EM structure of Shieldin complex bound to TRIP13 confirms this (Xie et al., 2021). The structure captures TRIP13 with its catalytic core engaging with C-REV7 N-terminus similar to how TRIP13 disassembles MAD2. This suggest the mechanism of Shieldin and MCC disassembly is similar with TRIP13 engaging with N-terminus of respective HORMA domains REV7 and MAD2. Additionally, this suggests the second protomer of REV7 takes over the role of p31^{comet}. However, this needs further investigation.

Moreover, the report has solved Shieldin: TRIP13 Cryo-EM structure with a tetramer of Shieldin complex due to use of shorter SHLD2 construct which the authors acknowledge themselves. The authors also acknowledge that the structural artifact of Shieldin allowed for higher resolution map to be obtained due to fortuitous interaction stabilizing Shieldin on TRIP13. In absence of these interactions, the Cyro-EM map obtained was of poor resolution and thus wasn't investigated further. This most likely suggests that the Shieldin complex containing REV7 dimer weakly binds TRIP13 and may not be the final target for disassembly. This explains the inactivity of TRIP13 towards Shieldin disassembly (Krijger et al., 2021; Xie et al., 2021). Indeed, a direct assay for measuring disassembly was not shown. Unsurprisingly, it was found that in cells overexpression of p31^{comet} upregulated HR activity similar to TRIP13 suggesting a role of p31^{comet} as a negative regulator of Shieldin (Sarangi et al., 2020).

The report suggests p31 interacts with C-REV7:SHLD3 using dimer interface in a way analogous to C-MAD2:CDC20. With REV7 forming a constitutive dimer in Shieldin it is hard to imagine how p31^{comet} utilizes this interface to bind Shieldin complex. Another explanation is that p31^{comet} may not be the adaptor but the competitor for free C-REV7 in cells. This way p31^{comet} recruitment would silence NHEJ by siphoning C-REV7 away from Shieldin assembly. This function of p31^{comet} is observed in SAC silencing where p31

blocks O-MAD2 recruitment by binding and poisoning C-MAD2 present at kinetochores (Yang et al., 2007). A biochemical assessment of TRIP13: p31^{comet} mediated disassembly of Shieldin complex is thus warranted.

It is unlikely that post translational modifications induce TRIP13's activity towards Shieldin complex. This is due to the fact both MAD2 and Bacterial HORMAs are disassembled by TRIP13 without any known PTMs. On the other hand, it is possible that TRIP13 utilises a novel adapter for Shieldin disassembly. Bacterial TRIP13 binds *E. coli* MS115-1/ *P. aeruginosa* CD-NTase that adopts a polymerase β-like nucleotidyl-transferase fold, suggesting TRIP13 can interact with diverse adapter proteins (Ye et al., 2020). Therefore, identification of such a factor would be necessary to address disassembly of Shieldin by TRIP13. Affinity purification coupled to mass spectrometry (AP-MS) approach was used to identifying Shieldin complex and TRIP13 as a negative regulator of Shieldin (Gupta et al., 2018; Clairmont et al., 2020; Krijger et al., 2021). A similar approach can be utilized for identifying TRIP13 adaptor for Shieldin complex.

4.5 Kinetics of Shieldin assembly

Seminal studies on MAD2 in assembly of MCC in SAC unveiled unique principles for HORMA domain proteins mediated assembly of macromolecular complexes. These studies showed the binding of MAD2 to CDC20 is a key step in the assembly of MCC which shows co-operative interaction. Shieldin assembly is also seem to be a co-operative binding interaction. In isolation, MAD2 is very slow in binding CDC20. *In vitro*, dimerization defective MAD2 binding to CDC20 This suggests MAD2 dimerization to play an essential role in MCC assembly. I observed a similar behaviour of REV7 in binding SHLD3 suggesting REV7 binds SHLD3 with MAD2-like kinetics. Similar to MAD2, I also observe REV7 dimer mutant is appreciably slower than WT REV7. These results mirror MAD2 in its binding to CDC20. Moreover, we observed a similar effect of REV7

binding to REV3 in Pol-ζ assembly (carried out by Damla Temel). This confirmed a key hypothesis that REV7 mediated assembly of Shieldin and Pol-ζ is slow and depends on conversion of REV7 from open to closed conformation. Whether this is true with other REV7 binding partners needs investigation. I quantified the kinetic rates of REV7 binding to SHLD3 or REV3 using SPR. As expected, the stable dissociation curves show that once bound to SHLD3 or REV3, REV7 fails to dissociate underlying the need for active disassembly. The k_{on} of ~10^{-4} μM^{-1} s^{-1} for REV7-SHLD3/REV7-REV3 is similar to what is reported for MAD2-CDC20 (Simonetta et al., 2007; Piano et al., 2021). This suggest that assembly of both shieldin complex and Pol-ζ in vitro is slow. However, the SPR measured on-rate constants between $REV7^{WT}$ and $REV7^{R124A}$ are near identical. This suggests dimerization plays insignificant role in Shieldin assembly. The likely explanation is that at high concentrations (~8 µM) $REV7^{WT}$ is present as a dimer. This allows for concentration and possibly oligomerization and thus, faster assembly when compared to $REV7^{R124A}$. At physiological concentrations in cells, it's unlikely that $REV7^{WT}$ would be present as a dimer and thus, would behave similar to $REV7^{R124A}$ in binding to SHLD3. Also, the association rates calculated here are most likely for closed conformer of REV7 as seen from the Q-column profile for purified protein. In MAD2, both open and close conformers bind CDC20 peptide with very different on-rate constants with the closed being two orders faster than open (Piano et al., 2021). It is unclear whether open conformer of REV7 can show similar slower on rates for binding.

4.6 Potential catalytic factors for Shieldin assembly

In cells, the NHEJ pathway right from induction of DSBs to re-ligation, takes about 30 minutes for completion (Mao et al., 2008). However, under unphysiological concentrations of REV7 (~ 8 µM), I show Shieldin assembly takes few hours. A similar observation was reported for MAD2 where, *in vivo* assembly of MCC was reported to be much faster than *in vitro*. The catalyst for MCC assembly was later identified to be a phosphorylated form

of MAD1:C-MAD2 complex (Faesen et al., 2017). It is possible a similar physical platform for REV7 conversion at DSB site for Shieldin assembly exists. MAD1:C-MAD2 phosphorylation is carried out by MPS1, it is possible a similar kinase activity to be involved in Shieldin assembly. Unlike MAD2 where dimerization is temporary for MCC assembly, REV7 dimerization is constitutive for Shieldin/Pol-ζ assembly suggesting a possibility where the catalyst could be a member of Shieldin complex itself. Also, it is possible that REV7 would be target for such phosphorylation directly.

A recent study identified a conserved Threonine at position 103 to be target for phosphorylation (Li et al., 2021). Moreover, the phosphorylated form of REV7 was enriched in the chromatin bound fractions as opposed to nonchromatin bound fractions. This phosphorylation of REV7 was found to be ATM kinase dependent. However, it is unclear whether ATM kinase itself phosphorylates REV7 or some other kinase such as DNA-PKcs.

A study identified an additional DNA repair protein that is able to interact with REV7 at DSBs other than SHLD3 and SHLD2. XL-MS data suggests RIF1 interacts with REV7 in the Shieldin complex. It binds the C-terminal region of REV7 in the canonical closed conformation (Setaiputra et al., 2021). It is further proposed that RIF1 functions as an antagonist to TRIP13-p31^{comet}. It may function as a necessary assembly component as it interacts with the closed conformation of REV7 specifically on the C-terminus with SHLD3 bound. Identification of NHEJ catalyst that brings about conversion of REV7 from open to closed conformation would be necessary in understanding the discrepancy observed in *in vitro* assembly of Shieldin complex as opposed to in the cells.

4.7 Molecular basis of Shieldin recruitment at DNA double strand breaks

SHLD2 subunit of Shieldin is known to bind DNA and is thought to block the access of long-range exonucleases (Gupta et al., 2018; Noordermeer et al., 2018). However, studies show SHLD2 is the last SHLD subunit to be recruited at DNA break site. Currently, it is hypothesized that the upstream factor RIF1 recruits the Shieldin complex through direct interaction with SHLD3. This RIF1 interacting surface is thought to be present at the C-terminus of SHLD3 which is predicted to be a folded domain (Dai et al., 2019; Liang et al., 2020). However, a recent study showed mammalian RIF1 N-terminal domain interacts with Shieldin complex but through REV7 subunit and not SHLD3. XL-MS data found extensive crosslinks between RIF1 N-terminus and REV7 C-terminus whereas RIF1 N-terminus crosslinks with SHLD3 were limited to N-terminal region (Setaiputra et al., 2021). This suggest SHLD3 C-terminus does not interact with RIF1 and contains an uncharacterized function.

In this thesis, I have experimentally shown the C-terminal region to be indeed folded in line with the predictions presented earlier. I have identified the functional role of SHLD3 in complex. SHLD3 binds DNA through its C-terminal domain and recruits REV7-SHLD proteins at DNA break site. This SHLD3 mediated recruitment of REV7-SHLD proteins is most likely supported by additional DNA repair factor as seen with the upstream factor RIF1's direct interaction with REV7. Further quantification of binding affinity for various DNA substrates revealed a modest DNA binding strength and strikingly no substrate specificity. SHLD3 with sequence preference to non-telomeric DNA sequences would make Shieldin assembly at telomeres less efficient This is in line with the identification of Shieldin complex at dysfunctional telomeres (Mirman et al., 2018). Moreover, yeast RIF1 is shown to be a strong dsDNA binding protein suggesting mammalian RIF1 could also be a potential dsDNA binding protein (Mattarocci et al., 2017). Alphafold prediction of human RIF1 shows it adopts a similar α-helical fold as yeast RIF1 with potential dsDNA binding electropositive grooves. With SHLD2 having a stronger preference for ssDNA

binding, SHLD3 would serve as a bridging molecule for stretches between dsDNA and ssDNA. With both RIF1 and SHLD2 having strong DNA binding affinities, moderate affinity of SHLD3 would suffice for recruiting REV7 at the DSBs/Telomeres. This overall strong avidity for DNA by multiple DNA binding proteins at DSB site might explain why SHLD3 may not need a strong DNA binding affinity to carry out its function in cells. This would explain the compaction of SHLD3 fold with reduced of loop regions and reduction of surface electropositivity observed between SHLD3 and its structural homolog EIF4-E. Moreover, a small nucleotide binding patch would allow for binding various different DNA substrates as seen from our experiments.

4.8 Model for Shieldin recruitment and assembly at DSBs

Taken together these results show the basis of Shieldin recruitment and assembly at DSBs, by concerted activity of both SHLD3 and REV7. I, hereby, propose a mechanism involving direct sensing of DNA by SHLD3 for Shieldin recruitment at DSBs. Utilising its DNA binding activity, SHLD3 is able to localise at DSBs. This provides a binding region near DSBs for REV7 to interact and assemble Shieldin complex. REV7 undergoes conversion from open to close and captures the N-terminal RBM of SHLD3. This allows for docking of another protomer of REV7 through the dimerization interface and subsequent recruitment of SHLD2-SHLD1. The incorporation of second protomer increases the interaction surface for Shieldin mediated recruitment of downstream components. The assembled Shieldin complex is strongly held at DSBs by multiple protein: protein interaction and strong protein: DNA interactions. For repair to follow completion, Shieldin is removed from DSB site by the activity of TRIP13.

4.9 Outlook

This thesis provides mechanistic insights into Shieldin assembly by HORMA domain REV7 and its recruitment to DNA by Shieldin complex subunit SHLD3.

These observations lead to further questions regarding Shieldin assembly and function.

1) Understanding the kinetic basis of Shieldin/ Pol-ζ assembly.

Our quantitative analysis shows Shieldin assembly *in vitro* mediated by SHLD3-REV7 binding is very slow. Similarly, we show Pol-ζ assembly mediated by REV3-REV7 binding follows slow kinetics. These results suggest a strong possibility that assembly of all REV7 containing complex is slow. Thus, understanding the basis of Shieldin assembly can help extend this knowledge to assembly of other key DNA repair complexes. It is unclear what makes these complexes assemble at faster rate in cells. Future studies on identifying these factors will be of utmost importance in fully understanding HORMA REV7's role in these processes.

2) Determining role of SHLD3 in cells

Our results show SHLD3 contains a conserved C-terminal EIF4-like domain which contains DNA binding activity. The model proposed for SHLD3 mediated recruitment of REV7-SHLD proteins to DSBs needs to be verified in cells. The SHLD3 mutants identified in this thesis would help understanding how much of SHLD3 DNA binding activity is needed for Shieldin recruitment. Recruitment of SHLD3 is dependent on 53BP1-RIF1 (Gupta et al., 2018). This suggest SHLD3 recruitment might be mediated additionally through direct interaction with possible upstream factors. It is possible that additional factors might help in stabilization of SHLD3 on DNA as the reported DNA binding strength of SHLD3 is intermediate.

3) Understanding structural basis of Shieldin function

Reconstitution studies here focused on understanding the assembly and recruitment of Shieldin complex at DSBs. Purification of stable full length SHLD2-SHLD1 or SHLD2 alone will be essential to delineate the conflicting data on SHLD2's DNA binding specificity (Noordermeer et al., 2018; Gao et al., 2018). Moreover, it is unclear whether SHLD2 has additional role outside ssDNA binding in Shieldin complex. A report suggests SHLD1 binds and recruits CST subunit CTC1 (Mirman et al., 2018). Structural studies would be necessary to mechanistically understand how Shieldin bridges DNA end protection with fill-in synthesis

Supplement

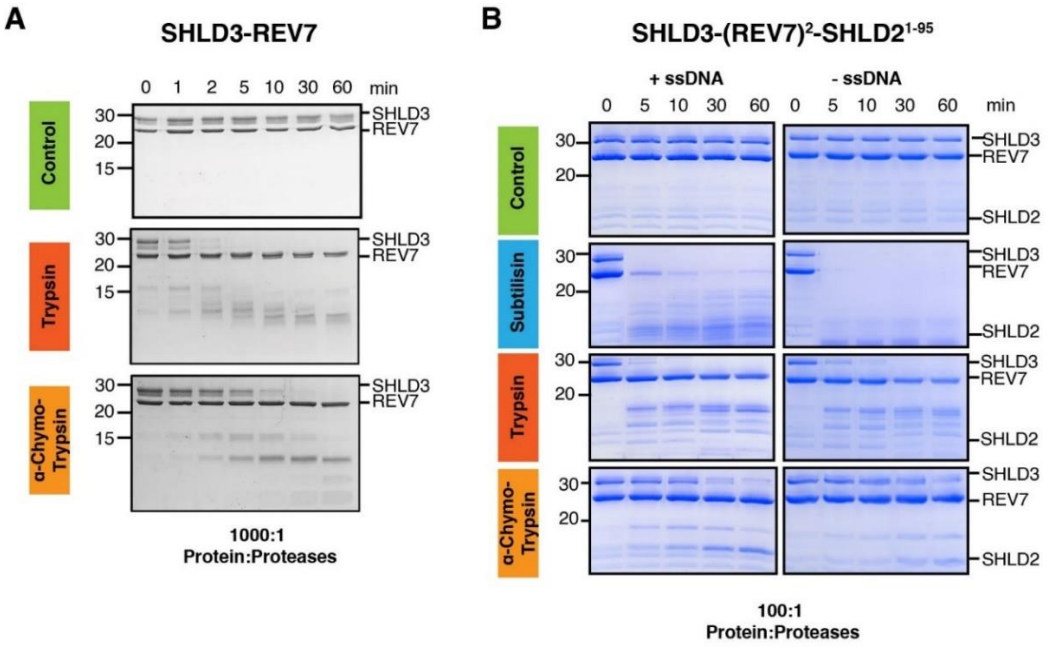

Figure S1: Limited proteolysis of SHLD3-REV7 and SHLD3-SHLD2-REV7 complex. (A) Proteolytic digestion of SHLD3-REV7 complex with trypsin and α-chymotrypsin. SHLD3 gets digested releasing two fragments of ~17 kDa and ~13 kDa. The ~17kDa fragment gets further digested to ~13 KDa. **(B)** Similar experiment performed with addition of protease subtilisin on SHLD3-REV7 bound to SHLD2$^{1-95}$ in presence or absence of ssDNA. The digestion patterns in presence or absence of ssDNA are similar suggesting SHLD3 maintains flexibility when bound or unbound to ssDNA. SHLD3 proteolytic cleavage pattern is similar whether SHLD2 is bound or not (compare A and B)

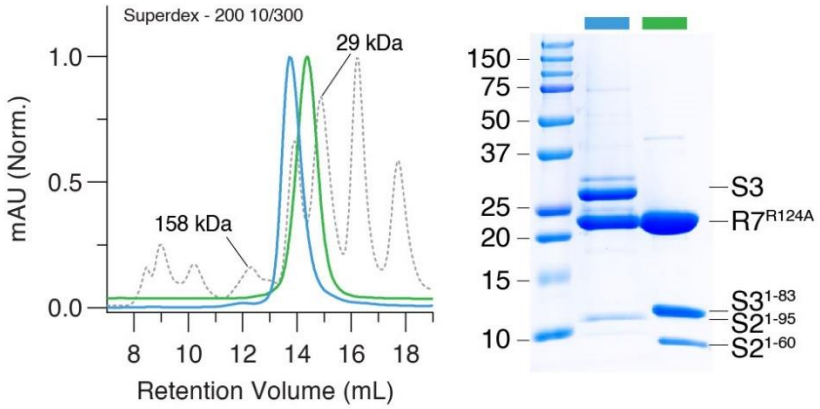

Figure S2: **Purification of Shieldin complex.** SEC profile of Shieldin complex (SHLD3-SHLD2$^{1-95}$-REV7^{R124A}) and Shieldin complex$^{\Delta SHLD3-CTD}$ (SHLD3$^{1-83}$-SHLD2$^{1-60}$-REV7^{R124A}) on Superdex-200 10/300 column. The peak eluted at 13 mL represents Shieldin complex (blue curve) while the peak eluted at 15 mL represents Shieldin complex$^{\Delta SHLD3-CTD}$ (green curve).

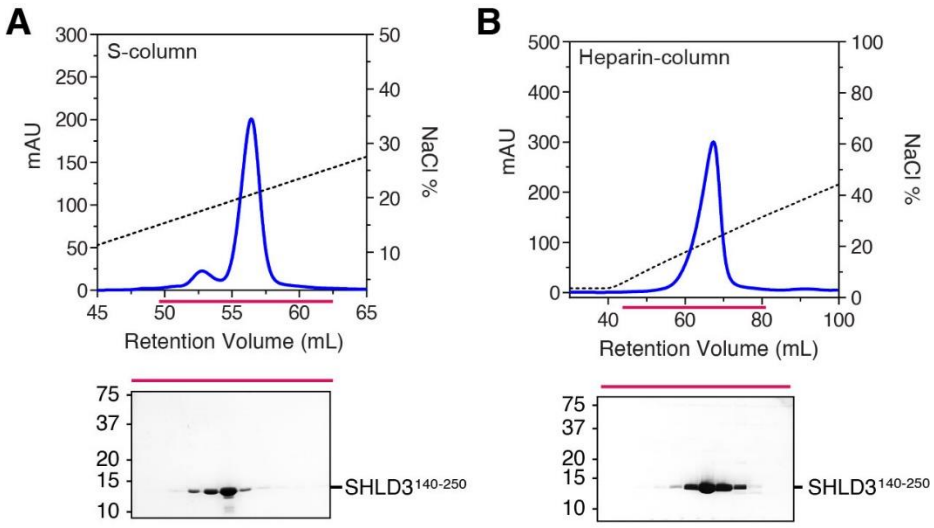

Figure S3: SHLD3-CTD binds positively charged resin. (A) Purified SHLD3 C-terminal domain binds Resource S column. The SHLD3 fragment elutes from S column at ~220 mM NaCl concentration. **(B)** Purified SHLD3 C-terminal domain binds heparin column. Similar to S column, SHLD3 fragment elutes from heparin column at ~220 mM NaCl concentration.

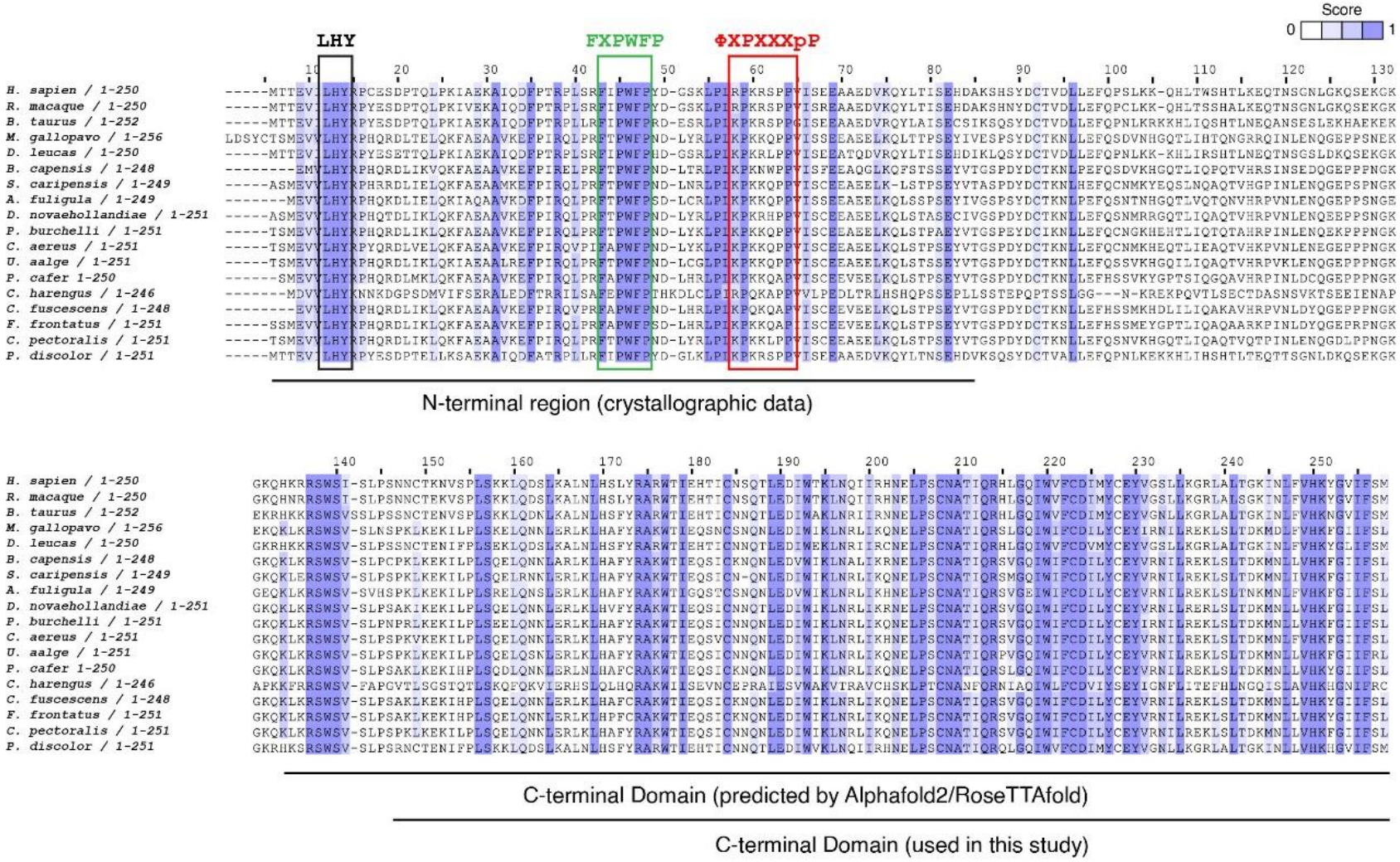

Figure S4. Sequence alignment of full length SHLD3 from multiple eukaryotic species Figure legends on next page.

Figure S4: Sequence alignment of full length SHLD3 from multiple eukaryotic species. Sequence alignment was carried out using Clustal O software. Alignment is coloured by phylogenetic conservation of amino acid physiochemical property similarity. Colouring begins at 30% conservation. Several conserved features in the N-terminal region are marked in boxes. LHY (black box) motif is involved in β strand interaction with SHLD2. FXPWFP (green box) motif interacts with the C-terminus of C-REV7. Closure motif sequence (red box) interacts with REV7 in safety belt conformation. C-terminus of SHLD3 similarly contains largely conserved residues/regions indicating a possible folded domain or containing residues of functional relevance.

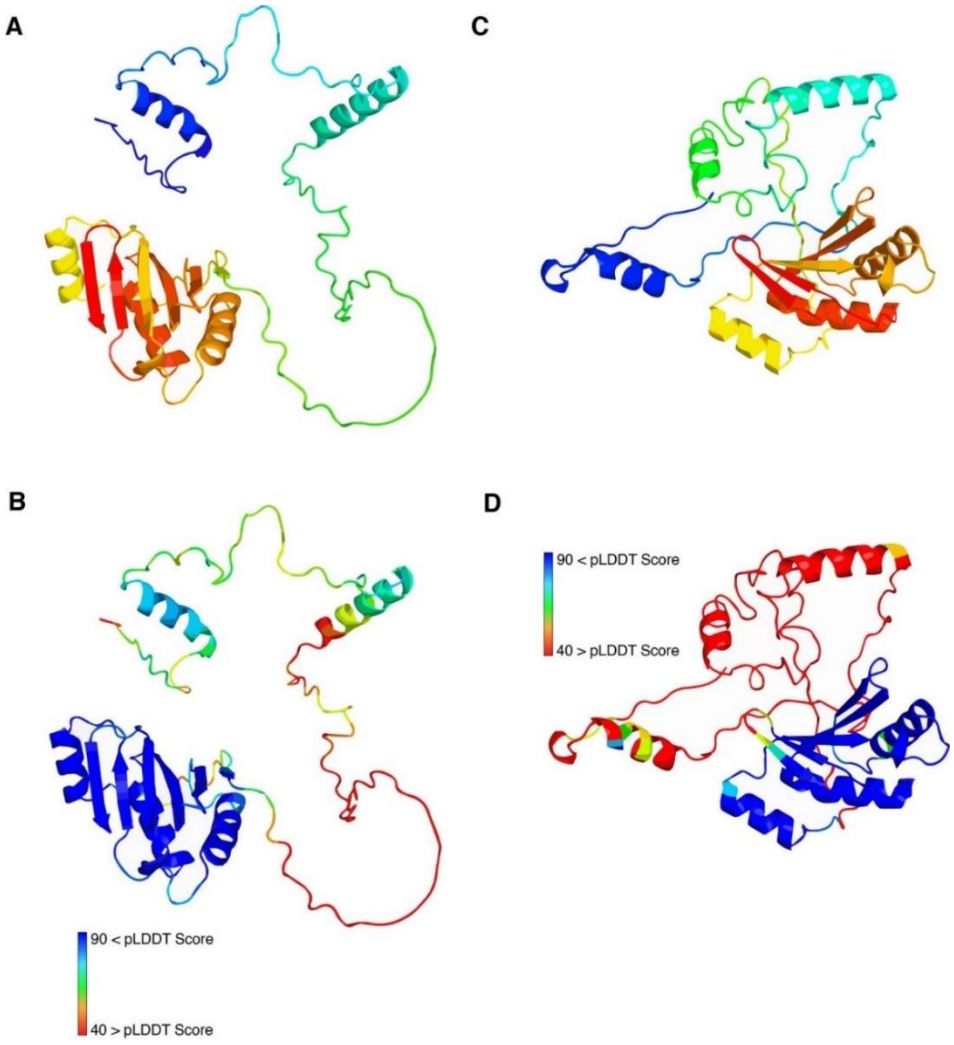

Figure S5: Full-length SHLD3 prediction by Alphfold2 (A and B) and RoseTTA fold (C and D). (A) Cartoon representation of Full-length SHLD3 prediction by Alphafold2 software. SHLD3 is shown in rainbow colour scheme: N → C; blue → red. Alphafold2 predicts SHLD3 contains a completely disordered N-terminal region (1-129) with a well folded C-terminal domain (1-130). The N-terminal shows presence of two alpha helices in line with crystallographic data. The N-terminus and C-terminus are separated by a region of poor conservation (Figure S5) and high flexibility. **(B)** pLDDT score for SHLD3 predicted structure (pLDDT score of > 90 suggest highly accurate model). Alphafold predicts moderate pLDDT score for N-terminus while high pLDDT score for C-terminus. **(C)** RoseTTA fold predictions for full length SHLD3 is similar to Alphafold. **(D)** RoseTTA fold predicts high confidence for C-terminal domain of SHLD3.

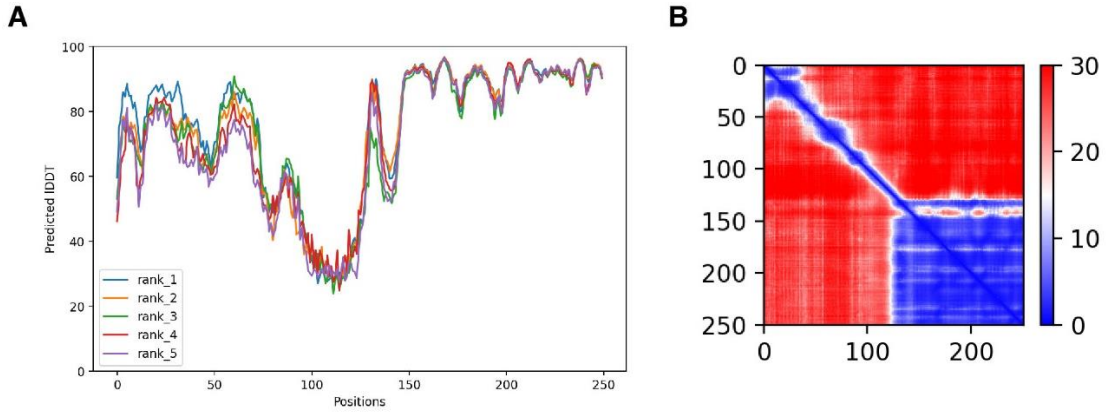

Figure S6: Accuracy of SHLD3 predicted structure. **(A)** Predicted LDDT score for five different models of SHLD3 built using Alphafold (Jumper et al., 2021). Higher score denotes high confidence in predicted positions whereas lower score denotes low confidence in predicted positions. **(B)** Relative domain position within SHLD3 is given by Predicted alignment error (PAE) plot. Blue colour denotes low error, red colour denotes high error. Alphafold predicts SHLD3 contains a domain at its C-terminus.

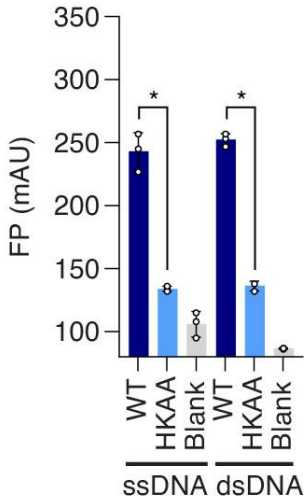

Figure S7: SHLD3^{HKAA} mutant shows reduced binding to telomeric DNA. Mutation of H242 and K243 to alanine reduced binding affinity of SHLD3-CTD to both telomeric ssDNA and dsDNA. Error bar represents s.d. (n = 3 independent experiments). One-tailed Student's test are indicated: *p < 0.001

Table S1: Plasmids used in this thesis.

Plasmid	**Source**
MBP-REV7^{WT} in pColi	this thesis
MBP-REV7^{R124A} in pColi	this thesis
MBP-REV7^{K44A,R124A,A135D} in pColi	this thesis
MBP-REV7$^{WT,\Delta N15}$ in pColi	this thesis
MBP-REV7$^{WT,\Delta C}$ in pColi	this thesis
MBP-REV7^{WT,LL} in pColi	this thesis
MBP-REV7$^{R124A,\Delta N15}$ in pColi	this thesis
MBP-REV7$^{R124A,\Delta C}$ in pColi	this thesis
MBP-REV7^{R124A,LL} in pColi	this thesis
GST-REV7^{WT} in pColi	this thesis
GST-REV7^{R124A} in pColi	this thesis
MBP-REV7$^{R124A,\Delta N15,LL}$ in pColi	this thesis
MBP-SHLD3$^{28-83}$ in pColi	this thesis
MBP-SHLD3$^{1-62}$ in pColi	this thesis
MBP-SHLD3$^{45-60}$ in pColi	this thesis
GST-SHLD3$^{1-62}$ in pColi	this thesis
MBP-SHLD2$^{1-60}$ in pColi	this thesis
GST-SHLD2$^{1-95}$ in pLIB	this thesis
MBP-REV3$^{1887-2014}$ in pColi	this thesis
His-SHLD3$^{140-250}$ in pRSF	this thesis
His-SHLD3$^{140-250,H242A,K243A}$ in pRSF	this thesis
SHLD3 in pLIB	this thesis
MBP-REV7^{WT} in pLIB	this thesis
MBP-REV7^{R124A} in pLIB	this thesis
REV7^{WT} in pLIB	this thesis
REV7^{R124A} in pLIB	this thesis

Table S1: Plasmids used in this thesis. (continued)

Plasmid	**Source**
GST-SHLD2$^{1-95}$ in pLIB	this thesis
MBP-REV7^{WT} in pLIB	this thesis
MBP-REV7^{WT}-SHLD3 in pBIG1a	this thesis
MBP-REV7^{R124A}-SHLD3 in pBIG1a	this thesis
REV7^{WT}-SHLD3-GST-SHLD2$^{1-95}$ in pBIG1a	this thesis
REV7^{R124A}-SHLD3-GST-SHLD2$^{1-95}$ in pBIG1a	this thesis

Table S2: Bacterial strains used in this thesis.

Strain	**Background**	**Reference**
Rosetta-BL21(DE3)	F^- ompT $hsdS_B(r_B^- m_B^-)$ gal dcm (DE3) pRARE (Cam^R)	Tegel H et al., 2009
LOBSTR-BL21(DE3)	F^- ompT $hsdS_B(r_B^- , m_B^-)$ gal dcm (DE3) arnA slyD	Andersen KR et al., 2013
NEB5α	fhuA2 Δ(argF-lacZ)U169 phoA glnV44 Φ80 Δ(lacZ)M15 gyrA96 recA1 relA1 endA1 thi-1 hsdR17	New England Biolabs
DH10EMBacY	F ⁻ mcr A Δ(mrr-hsdRMS- mcr BC) Φ80 lac ZΔM15 Δ lacX74 recA1 endA1 araD139 Δ(ara , leu)7697 galU galK λ⁻rpsL nupG/EMBacY/pMON7124	Geneva Biotech

Table S3: Insect cell lines used in this thesis.

Cell line	Origin	Reference
Sf9 (IPLB-Sf21-AE)	*Spodoptera frugiperda*	Vaughn, JL et al. (1977) Summers and Smith (1987)
High Five (BTI-TN-5B1-4)	*Trichoplusia ni*	Davis, T.R. et al. (1992)

Table S4: Oligonucleotides used for REV7 cloning. Gibson assembly was used for cloning. Mutagenesis was carried out using site-directed mutagenesis (SDM) protocol as discussed in section **2.2**.

PCR product	Forward primer (5'-3')	Reverse primer (5'-3')
REV7	CTGTTCCAGGGGCCCGG ATCCATGACCCACGCT CACACGACAAGACCTCA	TCCTCTAGTACTTCTCG ACAAGCTTTATGAGC GCGCTCTTCCAC
$REV7^{K44A}$	GTGGGCATCTTCCAGGC ACGCAAGAAGTAC	TCCTCTAGTACTTCTCG ACAAGCTTTATGAGC GCGCTCTTCCAC
$REV7^{A135D}$	AGCGTGTGCGATGAC GTCCTGGACCACAAC	TCCTCTAGTACTTCTCG ACAAGCTTTATGAGC GCGCTCTTCCAC
$REV7^{\Delta N}$	CTGTTCCAGGGGCCCGG ATCCGCCGATGTGCTCT GCGAGTTCCTG	TCCTCTAGTACTTCTCG ACAAGCTTTATGAGC GCGCTCTTCCAC

Table S4: Oligonucleotides used for REV7 cloning. (continued)

REV7$^{\Delta C}$	CTGTTCCAGGGGCCCGG ATCCATGACCCACGCT CACACGACAAGACCTCA	ATTTCCTCTAGTACTTCTC GACAAGCTTTTAAAGCTGC ATCTTTAAAATGTCCGACG
REV7^{LL}	GGAGAAATTCGTCTTTGA GATCACCCAGGGCTCTGG TTCGCTGTTGTCTCATGT GGAGC	TCCTCTAGTACTTCTCG ACAAGCTTTATGAGC GCGCTCTTCCAC

Table S5: Oligonucleotides used for SHLD3 cloning. Gibson assembly was used for cloning. Mutagenesis was carried out using site-directed mutagenesis (SDM) protocol as discussed in section **2.2**.

PCR product	**Forward primer (5'-3')**	**Reverse primer (5'-3')**
SHLD3	CTGTTCCAGGGGCCCGG ATCCATGACTACAGAA GTAATATTAC	TCCTCTAGTACTTCTCG ACAAGCTTTTACATACTA AAAATAACACC
SHLD3$^{1-62}$	CTGTTCCAGGGGCCCGG ATCCATGACTACAGAA GTAATATTAC	TCCTCTAGTACTTCTCG ACAAGCTTTTATTATTCAG AAATCACAGGTGGTGATC
SHLD3$^{46-60}$	CCACCATCGGGCGCG GATCCTCCGGGTCCAA GCTTCCACTCAGACCT AAAAGATCACCACCTG TGATTTCTGGGTCTTAA AAGCTTGTCGAGAAGT ACTAGAGGA	TCCTCTAGTACTTCTCGA CAAGCTTTTAAGACCCAGA AATCACAGGTGGTGATCT TTTAGGTCTGAGTGGAA GCTTGGACCCGGAGGA TCCGCGCCCGATGGTGG

Table S5: Oligonucleotides used for SHLD3 cloning. (continued)

SHLD3$^{28-83}$	CTGTTCCAGGGGCCCGG ATCCATGCAAGACTT TCCTACTCGTC	TCCTCTAGTACTTCTCG ACAAGCTTTTACTG TGTGACTTAGCATC
SHLD3$^{1-83}$	CTGTTCCAGGGGCCCGG ATCCATGACTACAGAA GTAATATTAC	TCCTCTAGTACTTCTCG ACAAGCTTTTACTG TGTGACTTAGCATC
SHLD3$^{140-250}$	CTGTTCCAGGGGCCCGG ATCCAGCAATAATTGTA CTAAAAACG	TCCTCTAGTACTTCTCG ACAAGCTTTTACATACTA AAAATAACACC
SHLD3$^{140-250,H242A,K243A}$	CTGTTCCAGGGGCCCGG ATCCAGCAATAATTGTA CTAAAAACG	TTACATACTAAAAATAAC ACCATATGCAGCCACAAA TAAATTAATTTTT

Table S6: Oligonucleotides used for SHLD2 cloning. Gibson assembly was used for cloning. Mutagenesis was carried out using site-directed mutagenesis (SDM) protocol as discussed in section **2.2**.

PCR product	**Forward primer (5'-3')**	**Reverse primer (5'-3')**
SHLD2$^{1-95}$	CTGTTCCAGGGGCCCG GATCCATGAGTGGA GGATCTC	TCCTCTAGTACTTCTCG ACAAGCTTTTAAGAAC GTACAAAGTCATCTTTCAC
SHLD2$^{1-60}$	CTGTTCCAGGGGCCCG GATCCATGAGTGGA GGATCTC	TCCTCTAGTACTTCTCG ACAAGCTTTTATTCA AGATTTTTGTGCTG

Table S7: Oligonucleotides used for REV3 cloning. Gibson assembly was used for cloning. Mutagenesis was carried out using site-directed mutagenesis (SDM) protocol as discussed in section **2.2**.

PCR product	**Forward primer (5'-3')**	**Reverse primer (5'-3')**
$REV3^{1871-2014}$	CTGTTCCAGGGGCCCG GATCCACCCCTCGAACT GCTAACATTCTG	TCCTCTAGTACTTCTCGA CAAGCTTTTATTCTTTGG CTTGAAGCCACACTTGA ACCAGTT

Table S8: Oligonucleotides used for shieldin complex cloning. Gibson assembly was used for cloning. Mutagenesis was carried out using site-directed mutagenesis (SDM) protocol as discussed in section **2.2**

Primers	**Forward primer (5'-3')**	**Reverse primer (5'-3')**
CasI_for (α)	AACGCTCTATGGTCTAAA GATTTAAATCGACCTACTC CGGAATATTAATAGATC	-
CasI_rev	-	AAACGTGCAATAGTATCCAG TTTATTTAAATGGTTATGA TAGTTATTGCTCAGCG
CasII_for	AAACTGGATACTATTGCAC GTTTAAATCGACCTACTCC GGAATATTAATAGATC	-
CasII_rev	-	AAACATCAGGCATCATTA GGTTTATTTAAATGGTTA TGATAGTTATTGCTCAGCG

Table S4: Oligonucleotides used for REV7 cloning. (continued)

CasIII_for	AAACCTAATGATGCCTG ATGTTTAAATCGACCTAC TCCGGAATATTAATAGATC	-
Casω _rev (ω)	-	AACCCCGATTGAGATATA GATTTATTTAAATGGTT ATGATAGTTATTGCTCAGCG

References

Alfieri, C., Chang, L. & Barford, D., 2018. Mechanism for remodelling of the cell cycle checkpoint protein MAD2 by the ATPase TRIP13. *Nature*, July, Volume 559, p. 274–278.

Anand, R., Ranjha, L., Cannavo, E. & Cejka, P., 2016. Phosphorylated CtIP Functions as a Co-factor of the MRE11-RAD50-NBS1 Endonuclease in DNA End Resection. *Molecular Cell,* December, Volume 64, p. 940–950.

Andersen, K. R., Leksa, N. C. & Schwartz, T. U., 2013. Optimized E. coli expression strain LOBSTR eliminates common contaminants from His-tag purification. *Proteins: Structure, Function, and Bioinformatics,* August, Volume 81, p. 1857–1861.

Antoni, A. D. et al., 2005. The Mad1/Mad2 Complex as a Template for Mad2 Activation in the Spindle Assembly Checkpoint. *Current Biology,* February, Volume 15, p. 214–225.

Aravind, L. & Koonin, E. V., 1998. The HORMA domain: a common structural denominator in mitotic checkpoints, chromosome synapsis and DNA repair. *Trends in Biochemical Sciences,* August, Volume 23, p. 284–286.

Arnaoutov, A. & Dasso, M., 2003. The Ran GTPase regulates kinetochore function. *Developmental cell,* Volume 5, p. 99–111.

Ashkenazy, H. et al., 2016. ConSurf 2016: an improved methodology to estimate and visualize evolutionary conservation in macromolecules. *Nucleic Acids Research,* May, Volume 44, p. W344–W350.

Baek, M. et al., 2021. Accurate prediction of protein structures and interactions using a three-track neural network. *Science,* August, Volume 373, p. 871–876.

Barazas, M. et al., 2018. The CST Complex Mediates End Protection at Double-Strand Breaks and Promotes PARP Inhibitor Sensitivity in BRCA1-Deficient Cells. *Cell Reports,* May, Volume 23, p. 2107–2118.

Bateman, A. et al., 2020. UniProt: the universal protein knowledgebase in 2021. *Nucleic Acids Research,* November, Volume 49, p. D480–D489.

Bekker-Jensen, S. & Mailand, N., 2010. Assembly and function of DNA double-strand break repair foci in mammalian cells. *DNA Repair,* December, Volume 9, p. 1219–1228.

Berger, I., Fitzgerald, D. J. & Richmond, T. J., 2004. Baculovirus expression system for heterologous multiprotein complexes. *Nature Biotechnology*, November, Volume 22, p. 1583–1587.

Berger, I. et al., 2013. The MultiBac Protein Complex Production Platform at the EMBL. *Journal of Visualized Experiments*, July.

Bluteau, D. et al., 2016. Biallelic inactivation of REV7 is associated with Fanconi anemia. *Journal of Clinical Investigation,* August, Volume 126, p. 3580–3584.

Boersma, V. et al., 2015. MAD2L2 controls DNA repair at telomeres and DNA breaks by inhibiting 5′ end resection. *Nature,* March, Volume 521, p. 537–540.

Borner, G. V., Barot, A. & Kleckner, N., 2008. Yeast Pch2 promotes domainal axis organization, timely recombination progression, and arrest of defective recombinosomes during meiosis. *Proceedings of the National Academy of Sciences*, February, Volume 105, p. 3327–3332.

Bouwman, P. et al., 2010. 53BP1 loss rescues BRCA1 deficiency and is associated with triple-negative and BRCA-mutated breast cancers. *Nature Structural & Molecular Biology*, May, Volume 17, p. 688–695.

Brandsma, I. & Gent, D. C., 2012. Pathway choice in DNA double strand break repair: observations of a balancing act. *Genome Integrity*, Volume 3, p. 9.

Bryant, H. E. et al., 2005. Specific killing of BRCA2-deficient tumours with inhibitors of poly(ADP-ribose) polymerase. *Nature,* April, Volume 434, p. 913–917.

Bunting, S. F. et al., 2010. 53BP1 Inhibits Homologous Recombination in Brca1-Deficient Cells by Blocking Resection of DNA Breaks. *Cell*, April, Volume 141, p. 243–254.

Buonomo, S. B. C., 2017. Rif1-Dependent Regulation of Genome Replication in Mammals. In: *Advances in Experimental Medicine and Biology.* s.l.:Springer Singapore, p. 259–272.

Burroughs, A. M. et al., 2015. Comparative genomic analyses reveal a vast, novel network of nucleotide-centric systems in biological conflicts, immunity and signaling. *Nucleic Acids Research,* November, Volume 43, p. 10633–10654.

Caldecott, K. W., 2008. Single-strand break repair and genetic disease. *Nature Reviews Genetics,* August, Volume 9, p. 619–631.

Cannavo, E. & Cejka, P., 2014. Sae2 promotes dsDNA endonuclease activity within Mre11–Rad50–Xrs2 to resect DNA breaks. *Nature*, September, Volume 514, p. 122–125.

Celli, G. B. & de Lange, T., 2005. DNA processing is not required for ATM-mediated telomere damage response after TRF2 deletion. *Nature Cell Biology*, June, Volume 7, p. 712–718.

Chapman, J. R., Taylor, M. R. G. & Boulton, S. J., 2012. Playing the End Game: DNA Double-Strand Break Repair Pathway Choice. *Molecular Cell*, August, Volume 47, p. 497–510.

Chatterjee, N. & Walker, G. C., 2017. Mechanisms of DNA damage, repair, and mutagenesis. *Environmental and Molecular Mutagenesis*, May, Volume 58, p. 235–263.

Chen, C., Jomaa, A., Ortega, J. & Alani, E. E., 2013. Pch2 is a hexameric ring ATPase that remodels the chromosome axis protein Hop1. *Proceedings of the National Academy of Sciences*, December, Volume 111, p. E44–E53.

Cheung, K. L. Y. et al., 2010. Alternative Oligomeric States of the Yeast Rvb1/Rvb2 Complex Induced by Histidine Tags. *Journal of Molecular Biology*, December, Volume 404, p. 478–492.

Clairmont, C. S. et al., 2020. TRIP13 regulates DNA repair pathway choice through REV7 conformational change. *Nature Cell Biology*, January, Volume 22, p. 87–96.

Clairmont, C. S. & D'Andrea, A. D., 2021. REV7 directs DNA repair pathway choice. *Trends in Cell Biology*, December, Volume 31, p. 965–978.

Cuevas-Navarro, A. et al., 2021. The RAS GTPase RIT1 compromises mitotic fidelity through spindle assembly checkpoint suppression. *Current Biology*, September, Volume 31, p. 3915–3924.e9.

Dai, Y. et al., 2020. Structural basis for shieldin complex subunit 3–mediated recruitment of the checkpoint protein REV7 during DNA double-strand break repair. *Journal of Biological Chemistry*, January, Volume 295, p. 250–262.

Davis, T. R., Trotter, K. M., Granados, R. R. & Wood, H. A., 1992. Baculovirus Expression of Alkaline Phosphatase as a Reporter Gene for Evaluation of Production, Glycosylation and Secretion. *Nature Biotechnology*, October, Volume 10, p. 1148–1150.

de Krijger, I. et al., 2021. MAD2L2 dimerization and TRIP13 control shieldin activity in DNA repair. *Nature Communications*, September.Volume 12.

de Krijger, I., Boersma, V. & Jacobs, J. J. L., 2021. REV7: Jack of many trades. *Trends in Cell Biology,* August, Volume 31, p. 686–701.

Denchi, E. L. & de Lange, T., 2007. Protection of telomeres through independent control of ATM and ATR by TRF2 and POT1. *Nature,* August, Volume 448, p. 1068–1071.

Dev, H. et al., 2018. Shieldin complex promotes DNA end-joining and counters homologous recombination in BRCA1-null cells. *Nature Cell Biology,* July, Volume 20, p. 954–965.

Erdős, G., Pajkos, M. & Dosztányi, Z., 2021. IUPred3: prediction of protein disorder enhanced with unambiguous experimental annotation and visualization of evolutionary conservation. *Nucleic Acids Research,* May, Volume 49, p. W297–W303.

Escribano-Díaz, C. et al., 2013. A Cell Cycle-Dependent Regulatory Circuit Composed of 53BP1-RIF1 and BRCA1-CtIP Controls DNA Repair Pathway Choice. *Molecular Cell,* March, Volume 49, p. 872–883.

Eytan, E. et al., 2014. Disassembly of mitotic checkpoint complexes by the joint action of the AAA-ATPase TRIP13 and p31comet. *Proceedings of the National Academy of Sciences,* August, Volume 111, p. 12019–12024.

Faesen, A. C. et al., 2017. Basis of catalytic assembly of the mitotic checkpoint complex. *Nature,* January, Volume 542, p. 498–502.

Farmer, H. et al., 2005. Targeting the DNA repair defect in BRCA mutant cells as a therapeutic strategy. *Nature,* April, Volume 434, p. 917–921.

Feng, X. et al., 2017. CTC1-mediated C-strand fill-in is an essential step in telomere length maintenance. *Nucleic Acids Research,* February, Volume 45, p. 4281–4293.

Findlay, S. et al., 2018. SHLD 2/ FAM 35A co-operates with REV 7 to coordinate DNA double-strand break repair pathway choice. *The EMBO Journal,* August.Volume 37.

Fong, P. C. et al., 2009. Inhibition of Poly(ADP-Ribose) Polymerase in Tumors fromBRCAMutation Carriers. *New England Journal of Medicine,* July, Volume 361, p. 123–134.

Gao, S. et al., 2018. An OB-fold complex controls the repair pathways for DNA double-strand breaks. *Nature Communications,* September.Volume 9.

Ghezraoui, H. et al., 2018. 53BP1 cooperation with the REV7–shieldin complex underpins DNA structure-specific NHEJ. *Nature,* July, Volume 560, p. 122–127.

Gibson, B. A. & Kraus, W. L., 2012. New insights into the molecular and cellular functions of poly(ADP-ribose) and PARPs. *Nature Reviews Molecular Cell Biology*, June, Volume 13, p. 411–424.

Goodarzi, A. A. et al., 2006. DNA-PK autophosphorylation facilitates Artemis endonuclease activity. *The EMBO Journal*, July, Volume 25, p. 3880–3889.

Gourley, C. et al., 2019. Moving From Poly (ADP-Ribose) Polymerase Inhibition to Targeting DNA Repair and DNA Damage Response in Cancer Therapy. *Journal of Clinical Oncology*, September, Volume 37, p. 2257–2269.

Gupta, R. et al., 2018. DNA Repair Network Analysis Reveals Shieldin as a Key Regulator of NHEJ and PARP Inhibitor Sensitivity. *Cell*, May, Volume 173, p. 972–988.e23.

Hara, K. et al., 2010. Crystal Structure of Human REV7 in Complex with a Human REV3 Fragment and Structural Implication of the Interaction between DNA Polymerase ζ and REV1. *Journal of Biological Chemistry*, April, Volume 285, p. 12299–12307.

Hara, K. et al., 2009. Purification, crystallization and initial X-ray diffraction study of human REV7 in complex with a REV3 fragment. *Acta Crystallographica Section F Structural Biology and Crystallization Communications*, November, Volume 65, p. 1302–1305.

Hara, K. et al., 2017. Dynamic feature of mitotic arrest deficient 2–like protein 2 (MAD2L2) and structural basis for its interaction with chromosome alignment–maintaining phosphoprotein (CAMP). *Journal of Biological Chemistry*, October, Volume 292, p. 17658–17667.

Iwai, H. et al., 2007. A Bacterial Effector Targets Mad2L2, an APC Inhibitor, to Modulate Host Cell Cycling. *Cell*, August, Volume 130, p. 611–623.

Jumper, J. et al., 2021. Highly accurate protein structure prediction with AlphaFold. *Nature*, July, Volume 596, p. 583–589.

Kikuchi, S. et al., 2012. Structural Basis of Recruitment of {DNA} Polymerase $\upzeta$ by Interaction between REV1 and REV7 Proteins. *Journal of Biological Chemistry*, September, Volume 287, p. 33847–33852.

Kim, H. & D\textquotesingleAndrea, A. D., 2012. Regulation of DNA cross-link repair by the Fanconi anemia/BRCA pathway. *Genes & Development*, July, Volume 26, p. 1393–1408.

Lamarche, B. J., Orazio, N. I. & Weitzman, M. D., 2010. The MRN complex in double-strand break repair and telomere maintenance. *FEBS Letters*, July, Volume 584, p. 3682–3695.

Leach, D. R. F., 1993. *A Short Course in Bacterial Genetics: A Laboratory Manual and Handbook for Escherichia coli and Related Bacteria. By JEFFREY H. MILLER. Cold Spring Harbor Laboratory Press. 1992. 876 pages. Price 95.00. ISBN 0 87969 349 5.*. s.l.:Cambridge University Press.

Liang, L. et al., 2020. Molecular basis for assembly of the shieldin complex and its implications for NHEJ. *Nature Communications*, April.Volume 11.

Li, F. et al., 2021. REV7/FANCV Binds to CHAMP1 and Promotes Homologous Recombination Repair. October.

Listovsky, T. & Sale, J. E., 2013. Sequestration of CDH1 by MAD2L2 prevents premature APC/C activation prior to anaphase onset. *Journal of Cell Biology*, October, Volume 203, p. 87–100.

Liu, H. & Naismith, J. H., 2008. An efficient one-step site-directed deletion, insertion, single and multiple-site plasmid mutagenesis protocol. *BMC Biotechnology*, Volume 8, p. 91.

Liu, T. & Huang, J., 2016. DNA End Resection: Facts and Mechanisms. *Genomics, Proteomics & Bioinformatics*, June, Volume 14, p. 126–130.

Lottersberger, F. et al., 2013. Role of 53BP1 oligomerization in regulating double-strand break repair. *Proceedings of the National Academy of Sciences*, January, Volume 110, p. 2146–2151.

Luo, X., Tang, Z., Rizo, J. & Yu, H., 2002. The Mad2 Spindle Checkpoint Protein Undergoes Similar Major Conformational Changes Upon Binding to Either Mad1 or Cdc20. *Molecular Cell*, January, Volume 9, p. 59–71.

Malik, R. et al., 2020. Structure and mechanism of B-family DNA polymerase $\upzeta$ specialized for translesion DNA synthesis. *Nature Structural & Molecular Biology*, August, Volume 27, p. 913–924.

Manke, I. A., Lowery, D. M., Nguyen, A. & Yaffe, M. B., 2003. BRCT Repeats As Phosphopeptide-Binding Modules Involved in Protein Targeting. *Science*, October, Volume 302, p. 636–639.

Mapelli, M. et al., 2006. Determinants of conformational dimerization of Mad2 and its inhibition by p31comet. *The EMBO Journal*, March, Volume 25, p. 1273–1284.

Mapelli, M., Massimiliano, L., Santaguida, S. & Musacchio, A., 2007. The Mad2 Conformational Dimer: Structure and Implications for the Spindle Assembly Checkpoint. *Cell*, November, Volume 131, p. 730–743.

Mapelli, M. & Musacchio, A., 2007. MAD contortions: conformational dimerization boosts spindle checkpoint signaling. *Current Opinion in Structural Biology*, December, Volume 17, p. 716–725.

Mattarocci, S. et al., 2017. Rif1 maintains telomeres and mediates DNA repair by encasing DNA ends. *Nature Structural & Molecular Biology*, June, Volume 24, p. 588–595.

Medendorp, K. et al., 2009. The Mitotic Arrest Deficient Protein MAD2B Interacts with the Small GTPase RAN throughout the Cell Cycle. *PLoS ONE*, September, Volume 4, p. e7020.

Miniowitz-Shemtov, S. et al., 2012. Role of phosphorylation of Cdc20 in p31comet-stimulated disassembly of the mitotic checkpoint complex. *Proceedings of the National Academy of Sciences*, May, Volume 109, p. 8056–8060.

Miniowitz-Shemtov, S. et al., 2015. Mode of interaction of TRIP13 AAA-ATPase with the Mad2-binding protein p31comet and with mitotic checkpoint complexes. *Proceedings of the National Academy of Sciences*, August, Volume 112, p. 11536–11540.

Mirdita, M. et al., 2021. ColabFold - Making protein folding accessible to all. August.

Mirman, Z. et al., 2018. 53BP1–RIF1–shieldin counteracts DSB resection through CST- and Pol alpha dependent fill-in. *Nature*, July, Volume 560, p. 112–116.

Mirman, Z. et al., 2022. 53BP1–shieldin-dependent DSB processing in BRCA1-deficient cells requires CST–Pol alpha primase fill-in synthesis. *Nature Cell Biology*, January, Volume 24, p. 51–61.

Mirza, M. R., Pignata, S. & Ledermann, J. A., 2018. Latest clinical evidence and further development of PARP inhibitors in ovarian cancer. *Annals of Oncology*, June, Volume 29, p. 1366–1376.

Miyake, Y. et al., 2009. RPA-like Mammalian Ctc1-Stn1-Ten1 Complex Binds to Single-Stranded DNA and Protects Telomeres Independently of the Pot1 Pathway. *Molecular Cell*, October, Volume 36, p. 193–206.

Murai, J. et al., 2012. Trapping of PARP1 and PARP2 by Clinical PARP Inhibitors. *Cancer Research*, October, Volume 72, p. 5588–5599.

Noordermeer, S. M. et al., 2018. The shieldin complex mediates 53BP1-dependent DNA repair. *Nature*, July, Volume 560, p. 117–121.

Noordermeer, S. M. & van Attikum, H., 2019. PARP Inhibitor Resistance: A Tug-of-War in BRCA-Mutated Cells. *Trends in Cell Biology*, October, Volume 29, p. 820–834.

Pernicone, N., Grinshpon, S. & Listovsky, T., 2020. CDH1 binds MAD2L2 in a Rev1-like pattern. *Biochemical and Biophysical Research Communications*, October, Volume 531, p. 566–572.

Pfleger, C. M., Lee, E. & Kirschner, M. W., 2001. Substrate recognition by the Cdc20 and Cdh1 components of the anaphase-promoting complex. *Genes & Development*, September, Volume 15, p. 2396–2407.

Piano, V. et al., 2021. CDC20 assists its catalytic incorporation in the mitotic checkpoint complex. *Science*, January, Volume 371, p. 67–71.

Prakash, S., Johnson, R. E. & Prakash, L., 2005. EUKARYOTIC TRANSLESION SYNTHESIS DNA POLYMERASES: Specificity of Structure and Function. *Annual Review of Biochemistry*, June, Volume 74, p. 317–353.

Qi, S., Kim, D. J., Stjepanovic, G. & Hurley, J. H., 2015. Structure of the Human Atg13-Atg101 HORMA Heterodimer: an Interaction Hub within the ULK1 Complex. *Structure*, October, Volume 23, p. 1848–1857.

Rizzo, A. A. et al., 2018. Rev7 dimerization is important for assembly and function of the Rev1/Polζ translesion synthesis complex. *Proceedings of the National Academy of Sciences*, Volume 115, p. E8191–E8200.

Rosenberg, S. C. & Corbett, K. D., 2015. The multifaceted roles of the HORMA domain in cellular signaling. *Journal of Cell Biology*, November, Volume 211, p. 745–755.

Rottenberg, S. et al., 2008. High sensitivity of BRCA1-deficient mammary tumors to the PARP inhibitor AZD2281 alone and in combination with platinum drugs. *Proceedings of the National Academy of Sciences*, October, Volume 105, p. 17079–17084.

Sarangi, P. et al., 2020. p31comet promotes homologous recombination by inactivating REV7 through the TRIP13 ATPase. *Proceedings of the National Academy of Sciences*, October, Volume 117, p. 26795–26803.

Schrödinger, L. L. C. & DeLano, W., 2020. *PyMOL*. s.l.:s.n.

Scully, R. et al., 1997. Dynamic Changes of BRCA1 Subnuclear Location and Phosphorylation State Are Initiated by DNA Damage. *Cell*, August, Volume 90, p. 425–435.

Setiaputra, D. & Durocher, D., 2019. Shieldin – the protector of DNA ends. *EMBO reports*, April.Volume 20.

Setiaputra, D. et al., 2022. RIF1 acts in DNA repair through phosphopeptide recognition of 53BP1. *Molecular Cell*, February.

Sievers, F. et al., 2011. Fast, scalable generation of high-quality protein multiple sequence alignments using Clustal Omega. *Molecular Systems Biology*, January, Volume 7, p. 539.

Simonetta, M. et al., 2009. The Influence of Catalysis on Mad2 Activation Dynamics. *PLoS Biology*, January, Volume 7, p. e1000010.

Sironi, L., 2002. Crystal structure of the tetrameric Mad1-Mad2 core complex: implications of a 'safety-belt' binding mechanism for the spindle checkpoint. *The EMBO Journal*, May, Volume 21, p. 2496–2506.

Steinegger, M. & Söding, J., 2017. MMseqs2 enables sensitive protein sequence searching for the analysis of massive data sets. *Nature Biotechnology*, October, Volume 35, p. 1026–1028.

Summers, M. D. & Smith, G. E., 1987. A manual of methods for baculovirus vectors and insect cell culture procedures..

Suzuki, H., Kaizuka, T., Mizushima, N. & Noda, N. N., 2015. Structure of the Atg101–Atg13 complex reveals essential roles of Atg101 in autophagy initiation. *Nature Structural & Molecular Biology*, June, Volume 22, p. 572–580.

Takai, H., Smogorzewska, A. & de Lange, T., 2003. DNA Damage Foci at Dysfunctional Telomeres. *Current Biology*, September, Volume 13, p. 1549–1556.

Tegel, H., Tourle, S., Ottosson, J. & Persson, A., 2010. Increased levels of recombinant human proteins with the Escherichia coli strain Rosetta(DE3). *Protein Expression and Purification*, February, Volume 69, p. 159–167.

Teichner, A. et al., 2011. p31comet promotes disassembly of the mitotic checkpoint complex in an ATP-dependent process. *Proceedings of the National Academy of Sciences*, February, Volume 108, p. 3187–3192.

Tomida, J. et al., 2015. REV7 is essential for DNA damage tolerance via two REV3L binding sites in mammalian DNA polymerase $\upzeta$. *Nucleic Acids Research*, January, Volume 43, p. 1000–1011.

Truong, C. D. et al., 2021. Cryo-EM reveals conformational flexibility in apo DNA polymerase ζ. *Journal of Biological Chemistry*, August, Volume 297, p. 100912.

Vaughn, J. L., Goodwin, R. H., Tompkins, G. J. & McCawley, P., 1977. The establishment of two cell lines from the insectspodoptera frugiperda (lepidoptera$\mathsemicolon$ noctuidae). *In Vitro*, April, Volume 13, p. 213–217.

Vermeulen, M. et al., 2010. Quantitative Interaction Proteomics and Genome-wide Profiling of Epigenetic Histone Marks and Their Readers. *Cell*, September, Volume 142, p. 967–980.

Vink, M. et al., 2006. In Vitro FRAP Identifies the Minimal Requirements for Mad2 Kinetochore Dynamics. *Current Biology*, April, Volume 16, p. 755–766.

Wang, F. et al., 2012. Human CST Has Independent Functions during Telomere Duplex Replication and C-Strand Fill-In. *Cell Reports*, November, Volume 2, p. 1096–1103.

Wang, X. et al., 2019. REV7 has a dynamic adaptor region to accommodate small GTPase RAN/Shigella IpaB ligands, and its activity is regulated by the RanGTP/GDP switch. *Journal of Biological Chemistry*, October, Volume 294, p. 15733–15742.

Waterhouse, A. M. et al., 2009. Jalview Version 2–a multiple sequence alignment editor and analysis workbench. *Bioinformatics*, January, Volume 25, p. 1189–1191.

Waters, L. S. et al., 2009. Eukaryotic Translesion Polymerases and Their Roles and Regulation in DNA Damage Tolerance. *Microbiology and Molecular Biology Reviews*, March, Volume 73, p. 134–154.

Weissmann, F. et al., 2016. biGBac enables rapid gene assembly for the expression of large multisubunit protein complexes. *Proceedings of the National Academy of Sciences*, Volume 113, p. E2564–E2569.

Westhorpe, F. G., Tighe, A., Lara-Gonzalez, P. & Taylor, S. S., 2011. p31comet-mediated extraction of Mad2 from the MCC promotes efficient mitotic exit. *Journal of Cell Science*, November, Volume 124, p. 3905–3916.

Wojtaszek, J. et al., 2012. Structural Basis of Rev1-mediated Assembly of a Quaternary Vertebrate Translesion Polymerase Complex Consisting of Rev1, Heterodimeric Polymerase (Pol) ζ, and Pol κ. *Journal of Biological Chemistry,* September, Volume 287, p. 33836–33846.

Wojtasz, L. et al., 2009. Mouse HORMAD1 and HORMAD2, Two Conserved Meiotic Chromosomal Proteins, Are Depleted from Synapsed Chromosome Axes with the Help of TRIP13 AAA-ATPase. *PLoS Genetics,* October, Volume 5, p. e1000702.

Xia, G. et al., 2004. Conformation-specific binding of p31comet antagonizes the function of Mad2 in the spindle checkpoint. *The EMBO Journal,* July, Volume 23, p. 3133–3143.

Xie, W. et al., 2021. Molecular mechanisms of assembly and TRIP13-mediated remodeling of the human Shieldin complex. *Proceedings of the National Academy of Sciences,* February, Volume 118, p. e2024512118.

Xie, W., Yang, X., Xu, M. & Jiang, T., 2012. Structural insights into the assembly of human translesion polymerase complexes. *Protein & Cell,* November, Volume 3, p. 864–874.

Xu, G. et al., 2015. REV7 counteracts DNA double-strand break resection and affects PARP inhibition. *Nature,* March, Volume 521, p. 541–544.

Yamazaki, S., Hayano, M. & Masai, H., 2013. Replication timing regulation of eukaryotic replicons: Rif1 as a global regulator of replication timing. *Trends in Genetics,* August, Volume 29, p. 449–460.

Yang, M. et al., 2007. p31comet Blocks Mad2 Activation through Structural Mimicry. *Cell,* November, Volume 131, p. 744–755.

Ye, Q. et al., 2017. The AAA+ ATPase TRIP13 remodels HORMA domains through N-terminal engagement and unfolding. *The EMBO Journal,* June, Volume 36, p. 2419–2434.

Ye, Q. et al., 2020. HORMA Domain Proteins and a Trip13-like ATPase Regulate Bacterial cGAS-like Enzymes to Mediate Bacteriophage Immunity. *Molecular Cell,* February, Volume 77, p. 709–722.e7.

Ye, Q. et al., 2015. TRIP13 is a protein-remodeling AAA+ ATPase that catalyzes {MAD}2 conformation switching. *eLife,* April.Volume 4.

Yu, X. et al., 2003. The BRCT Domain Is a Phospho-Protein Binding Domain. *Science,* October, Volume 302, p. 639–642.

Zgheib, O., Pataky, K., Brugger, J. & Halazonetis, T. D., 2009. An Oligomerized 53BP1 Tudor Domain Suffices for Recognition of DNA Double-Strand Breaks. *Molecular and Cellular Biology*, February, Volume 29, p. 1050–1058.

Z, Mao, Bozzella, M., Seluanov, A. & Gorbunova, V., 2008. Comparison of nonhomologous end joining and homologous recombination in human cells. *DNA Repair*, October, Volume 7, p. 1765–1771.

Zimmermann, M. & de Lange, T., 2014. 53BP1: pro choice in DNA repair. *Trends in Cell Biology*, February, Volume 24, p. 108–117.

Acknowledgements

First of all, I would like to thank Dr. Alex C. Faesen for giving me the opportunity to work on such a challenging yet interesting project. Thank you for introducing me to the world of DNA repair and for your constant support, patience and guidance throughout these four years, which became a roller-coaster ride for me. I really cherished the scientific enthusiasm he brought along in our group meetings and journal clubs.

I would also like to thank Prof. Dr. Patrick Cramer and Prof. Dr. Peter Rehling for offering invaluable insights and helpful suggestions through-out my PhD years. I am thankful to Dr. Alexander Stein, Dr. Sonja Lorenz and Prof. Dr. Matthias Dobbelstein for being part of my examination board. I would like to thank Dr. Jacqueline Jacobs and Igne de Krijger for their strong efforts for the collaboration and also for their chase for the publication. I would also like to extend my thanks to the GGNB office for organising the doctoral program and the support they provide to students.

I would like to thank all members of biochemistry of signal dynamics, both past and present. I am grateful to all for your friendship and support. Thank you to Francesca for hanging there with me since beginning and for the endless HORMA-related discussions. I would like to thank Stephanie for her support and assistance in lab. Thank you for lifting our moods from time to time with your amazing baking skills. I would like to thank Simran and Damla for all their help in this project. I am grateful to Anh, Anoshi, Bastian and Laura for the joyous atmosphere they brought in the lab and making my stay more so memorable. I am very grateful for the countless discussions we had on scientific as well as non-scientific topics. This thesis wouldn't be the same without all of your participation.

Moreover, I would like to thank all the members of Stein lab, Jahn lab and Lorenz lab for their scientific inputs during lab seminars.

I would also like to thank our secretary, Juliane Moses, for her administrative support. I thank Vinay and Majety for their advice and support on matters of everyday life in Germany, especially during the initial months when I arrived.

I thank Ulrich, Christian, Metin, Majety and Lucas for technical assistance they offered for this project.

I would like to thank all my friends for their support. I am in-debt to Ashutosh for his help, advice, support and confidence in me and my work through my doctorate years. Thanks for cheering me up, whenever I felt low from personal and professional issues. Thank you for your support in all areas of life. I also thank Francesca and Simran for their beloved friendship and support. I thank both Ashutosh and Simran for proof-reading this thesis. I also thank my roommate Wei for being such a supportive friend. I thank Frank, Sofia, Artem, Rebecca and Dev for their friendship and discussions on life in general.

And finally, I would like to thank my family for their constant support and faith in me. Thank you for not worrying too much and always letting me follow my passion.

In the end, I would like to dedicate my doctoral degree to my father. Without his support and encouragement, I wouldn’t have accomplished this achievement.